

EXPERIMENTAL STUDY ON THE PROPERTIES OF SOLAR CELLS
AND SOLAR CELL MODULES IN CONNECTION WITH THE
MISSION OF A SOLAR PROBE

PART I: SOLAR CELLS

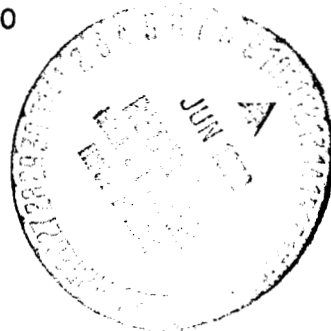
by Siemens Aktiengesellschaft
in collaboration with Messerschmitt-Boelkow GmbH

From: "Experimentalstudie ueber die Eigenschaften von Solarzellen
und Solarzellenmodulen im Hinblick auf die Mission einer Sonnen-
sonde. Teil I: Solarzellen", Siemens AG, Feb.1969 (Contract
RV 4-SS/01/68; period covered: July 15,1968 -- Jan.1,1969).

Translated by
Belov & Associates
for
N.A.S.A. GSFC Library
Contract NAS 5-10888
Item no. 10888-027
February 1970

FACILITY FORM 602

N70-73733	
(ACCESSION NUMBER)	(THRU)
130	None
(PAGES)	(CODE)
SR-110117	
(NASA CR OR TMX OR AD NUMBER)	(CATEGORY)



Federal Ministry for Scientific Research

Contract RV 4-SS/01/68

**Experimental Study on the Properties of Solar Cells and Solar Modules
in connection with the Mission of a Solar Probe.**

Part I

Solar Cells

by

**E. Nitsche
H. Pfeleiderer
G. Rittmayer
K. Wohlleben**

Siemens Aktiengesellschaft (Corporation)

Research Laboratory Erlangen

February 1969

<u>Table of Contents</u>	<u>Page</u>
Summary	1
1. Introduction	2
1.1 Starting Point	2
1.2 Solar Cell Requirements for Missions near the Sun	2
1.3 Scope	2
2. Short Circuit Current Density	6
2.1 Spectral Sensitivity	6
2.2 Two-layer Model	7
2.3 Recombining Effects	8
2.4 External Quanta Yield	8
3. Characteristic	10
3.1 Substitute Circuit Diagram	10
3.2 Effective Internal Resistance	11
3.3 General Graphic Presentation	12
3.4 Grid and Insolation	13
4. Computation of the Grid Optimization	16
4.1 Finger Width	16
4.2 Finger Depth	17
4.3 Layer Resistance of the n-layer	17
4.4 1 Ohmcm - p - Silicon	18
4.5 Spoolshaped Satellite Body	19
4.6 Cylindershaped Satellite Body	22
4.7 Result of Optimization Computation	22
5. Production of Type V Solar Cells for Solar Probes	24
6. Measurement of the Quanta Yield on Type V Solar Cells and Production of a Standard Cell	27
6.1 Measurement of the Quanta Yield and Computation of the Extraterrestrial Short Circuit Current	27

6.2	Measurement of the Quanta Yield on Type V Solar Cells	28
6.3	Production of a Standard Type V Cell	28
6.4	Mathematical Corrections on the Measured Electrical Quantities	29
7.	I/U Graphs of Type V Solar Cells under Temperatures Ranging from -190°C to $+200^{\circ}\text{C}$ for Insolations between 0.5 and 11 suns	32
7.1	Standard Requirements 28°C , 1 AMO	32
7.2	Temperatures below 28°C , Insolation between 0.5 and 1 AMO	34
7.3	Temperatures above 28°C , Insolations to 11 AMO	34
8.	Endurance Tests on Type V Solar Cells under Temperatures to 515°C in a High Vacuum and under an Inert Gas	35
9.	Storage Tests of Type V Solar Cells in an Extremely Humid Atmosphere	37
9.1	Boiling Water Test	37
9.2	Water Vapor Test	37
9.3	Humidity Test	38
9.4	Tape Test	39
10.	Radiation Resistance	40
11.	Results	42
11.1	Comparison of Computation and Test	42
11.2	Families of Characteristics	44
11.3	Temperature Coefficients	44
11.4	Series Resistance	44
11.5	Constancy	45
11.6	Power Output during the Mission	46
	Bibliography	48
12.	Computation of the Radiation Charge and the Equivalent Dose	49
	Summary	49

12.1 Radiation Charge on the Ascent through the Allen Belt	50
12.2 Radiation Charge through the Solar Flares	52
Bibliography	55

Summary

The presented theoretical study shows, that solar cells for missions into the space in the neighbourhood of the sun get enough power to work. The increase of the output by the high insolation is much higher than the decrease of the output by the operation temperature. Therefore the minimum of output during the whole mission is near the earth although there is the lowest operation temperature. Difficult is only the stability of the solar cells at the given high temperature.

As an improved development of the earlier type IV a solar cell type V is developed, satisfying all conditions necessary for the mission into the neighbourhood of the sun. The output near the earth is about 60.5 mW by an operating voltage of nearly 500 mV and a series resistance of about 0.1Ω . During a storage test of 1600 hours the cells were stable at high temperature and at high humidity and in preliminary tests resistant against radiation.

1. Introduction

1.1 Starting Point

The starting point for our study is the type IV Siemens solar cell developed for missions near the earth. This cell is characterized by an n/p arrangement in which a thin n-layer is produced through a diffusion process on p-silicon with a specific resistance of 10 ohmcm. The back of the cell is solid, the front of the cell is comb-like with seven fingers contacted by a silver-titanium alloy. This cell has a series resistance of 0.3 ohm.

This series resistance is composed of the bulk resistance of the p doped silicon layer and of a second item of resistance made up of the resistance of the highly doped n-layer and of that of the metallic contact arrangement on the front of the cell. The total resistance is distributed on these two resistances in the ratio of about 3 to 1.

1.2 Solar Cell Requirements for Missions near the Sun

When using solar cells as the power source for a probe to be sent near the sun new requirements arise which differ basically from those for solar cells used for missions near the earth. Near the sun there is available a sufficiently great amount of radiation intensity. But it must be assumed that the much higher operating temperature of the solar cell in the vicinity of the sun will necessitate a careful estimate of the increased operating efficiency owing to the increased intensity and of the decreased operating efficiency owing to the increased temperature.

Solar cells have up to now been used in temperatures of up to 90°C. This temperature will be greatly exceeded near the sun. The path of the planned solar probe will be near the sun for about 8 weeks. Consequently

solar cells for solar probes must undergo rigid tests of their ability to withstand high operating temperatures over a long period of time. It is known that the solar cell characteristic is changed under extremely high temperatures¹⁾. This fact can only be explained by the formation of leaks. These can occur when the contact material is diffused through the thin n-layer and short circuits the pn-transition. These reasons point to the usefulness of studying the properties of solar cells with a thicker than normal n-layer.

Without knowing the exact trajectory data of a solar probe which will approach the sun as close as 0.3 astronomical units one can roughly estimate that the radiation received in the course of the mission during the passage through the earth's radiation belt and during the flight to and around the sun must be substantially below the equivalent dose for missions near the earth. This assumption, to be proved later on, permits us to consider the use of silicon with a lower ohm rating, for instance down to specific resistances of $0.2 \Omega \text{ cm}$, for the planning of a solar cell for a solar probe.

To increase the electrical output of a solar cell it is necessary to minimize the internal resistance. A series resistance that is smaller than the usual ones increases the performance of solar cells also near the earth. Above all, a smaller series resistance will have many advantages near the sun under intensive insolation.

Aside from the structural arrangement of the contact electrodes on the upper side of the cell (number, width and depth of fingers) the resistance of the thin n-layer and of the basic material contribute to the internal resistance.

1.3 Scope

The solar cells for the solar probe are subjected to minimum temperatures of -64°C near the earth and to maximum temperatures of $+140^{\circ}\text{C}$ near the sun. The maintenance of these temperature limits is assured through proper design. With vertical incidence insolation will increase from 1 AMO to 11 AMO near the sun. The solar cell must produce enough energy for satisfactory operation both under conditions of low temperatures and small insolation near the earth as well as under those of high temperatures and high insolation near the sun.

Starting with the well known type IV solar cell we must examine whether from this type cell we may, with as few manufacturing changes as possible, derive a cell suitable for a solar probe.

In order to arrive experimentally at a meaningful solution in the short time available it seemed advisable to make first of all a theoretical study of the transition from the known type IV to the new type V cell. We started with measurements on type IV cells for insolation of 1 AMO and varied the number, width and depth of fingers, the n-layer resistance, the basic resistance, insolation and temperature in an optimization computation.

The execution of such an optimization computation appeared of particular importance at the start of our research since at that time no decision had as yet been reached as to the form of the satellite and consequently as to the temperature and insolation conditions of the solar cells. A theoretical optimization could thus consider in advance all eventualities which could modify the mission during the course of the experimental research. For this reason we undertook the optimization computation at the beginning of our research. From its results and taking into account the characteristic

data of the solar probe which had in the meantime been laid down and some preliminary experimental work it was then possible, through modification of a few production procedures, to derive a solar cell type suitable for a solar probe, from the type IV cell. It was then the mission of the experimental study to see whether theory and experiment agreed and to determine experimentally the properties of type V solar cells under the extreme operating conditions of the solar probe.

2. Short Circuit Current Density

2.1 Spectral Sensitivity

The optically impressed current density of a solar cell may be broken up according to the wave length spectrum of the solar radiation:

$$I = \int j(\lambda) d\lambda, \text{ where } \lambda \text{ is the length of the light wave.}$$

The spectral density j may be represented as follows:

$$j(\lambda) = e n(\lambda) [1 - r(\lambda)] [1 - \exp(-k(\lambda) d)] \beta(\lambda) \alpha(\lambda)$$

e represents the elementary charge and n the spectral function of the density of the photon stream. The reflection coefficient r is meant to include also the absorption in the protective and tempering layers. k is the absorption coefficient in the solar cell and d the thickness of the solar cell. It is assumed that the so far unabsorbed light on the back of the solar cell has no effect on the impressed current. The internal quanta yield β is the number of electron - aperture-pairs which an absorbed light quantum produces. (β may be assumed to equal 1 up to the absorption edge.) The collective coefficient α represents the probability of an optically produced electron - aperture - pair contributing to the impressed current. The impressed current is to be measured as a short circuit current. Only under very high insolation does the short circuit current lose a part of the impressed current. We shall refer to this again in the next part. According to the above formula one obtains by measurement of j when the remaining quantities are known. Naturally it is helpful when the thickness of the solar cell is large enough so that $kd \gg 1$ is valid for all wave lengths. The tempering layer should be chosen so that

$$\int N(\lambda) d\lambda, N(\lambda) = n(\lambda) r(\lambda) \beta(\lambda) \alpha(\lambda),$$

becomes minimal.

2.2 Two-Layer Model

In order to obtain a simple theoretical expression for α the front and back layers of the solar cells, which are separated by the pn-transition, are regarded as homogeneous. The pn-transition must be abrupt and show a Shockley curve. The essential parameters, on which the resulting formula for α depends²⁾, include, besides the absorption constant k , the front and back layer thicknesses d_1 and d_2 , the diffusion lengths in these layers L_1 and L_2 as well as the surface recombination velocities on the front and back s_1 and s_2 . When the thickness of the solar cell $d = d_1 + d_2$ is sufficiently large s_2 is of no importance. The coefficient naturally approaches its ideal value 1 the large L_1/d_1 and L_2/d_2 and the smaller s_1 and s_2 are.

One can attempt, through adaptation on experimental α -curves to determine the parameters in the formula for α . The diffusion length L_2 in the back layer influences the long wave portion of the α course, that is the red sensitivity of the solar cell. The short wave portion of α , that is the blue sensitivity, is on the other hand mainly dependent on the parameters of the front layer, namely d_1 , L_1 , and s_1 . Function $\alpha(\lambda)$ can also be expressed as $\alpha(1/k)$. This is useful when $\alpha(1/k)$ runs out into a straight line toward the short wave end of the solar spectrum, because the parameters of the front layers can then be obtained in a simple manner^{3),4),5)}. But presumably this only happens when the thickness of the front layer is relatively large, from 5 to 10 μm ⁴⁾. However, based on the solar spectrum and function $k(\lambda)$ for silicon the impressed current increases as the front layer thickness d_1 decreases. This can be shown both theoretically, by inserting plausible values for the α parameters, as well as experimentally. The extension of function $\alpha(1/k)$ for solar cells with $d_1 = 0.5/\mu$ and below is no longer recognizably linear.

This circumstance, for one thing, renders more difficult the comparison of theoretical and experimental α -curves in space. For another, theory and experiment coincide most closely when we assume that s_1 and L_1 are both either ∞ or 0.⁶⁾ Furthermore, the obtainable coincidence is unsatisfactory at best.

2.3 Recombining Defects

From these results it can be concluded that, on the one hand, the blue sensitivity of silicon solar cells is generally poor and, on the other hand, the two-layer solar cell model that was used is unsuited for thin front layers. A realistic theory on the contribution of the front layer to the impressed current would have to try to evaluate the largely disturbed structure of the front layer. It is known that when high phosphorus concentrations are diffused in silicon, phosphorus bearing deposits and alloys are formed⁷⁾. These could have an unfavorable effect on the life of the surplus charge carriers. A comprehensive description of the crystal defects to be expected during diffusion processes and of the experimental possibilities for their detection is given by John⁸⁾. These defects are particularly marked in the case of thin diffused layers as they occur in silicon solar cells. In the case of relay diodes a defective surface layer shows up as an inactive layer⁹⁾. It would make an interesting study to look into the micro-defects of solar cells and the recombination mechanisms connected with them¹⁰⁾.

2.4 External Quanta Yield

Figures 1 and 2 show the existing conditions of our solar cells. The extreme quanta yield is given

$$Q(\lambda) = [1 - r(\lambda)] \beta(\lambda) \alpha(\lambda).$$

The crosses are measuring points of a typical solar cell.

The curves were computed with a formula based on the aforementioned two-layer model. The decrease in the quanta yield in the case of short wave lengths is determined by the very great surface recombination speed $s_1 = 10^7$ cm/s. The change of the diffusion length L_2 in the back layer shifts the red part of the spectrum (Figure 1). The assumption of various front-layer thicknesses d_1 causes a shift in the blue part of the spectrum (Figure 2). The smaller d_1 is, the greater is the blue sensitivity and the impressed current of the solar cell. Furthermore, a decrease in d_1 also causes an increase in the surface resistance of the front layer. In accordance with 1.1 the quanta yield curves shown in Figures 1 and 2 give the short circuit current densities contained in Table 1 below:

TABLE 1

$L_p = 20 \mu\text{m}$	$D_p = 10 \text{ cm}^2/\text{sec}$	$s_1 = 10^7 \text{ cm/sec}$
L_n (μm)	e_1 (μm)	j_k (mA/cm^2)
100	0.1	37.7
150	0.1	39.0
200	0.1	39.8
150	0.1	39.0
150	0.2	37.9
150	0.3	37.0
150	0.5	35.5

For purposes of comparison 299 T 51 $j_k = 36.3$

KZ 2124

A type IV solar cell gives, in comparison, a short circuit current density, computed from the quanta yield and the solar spectrum, of $36.3 \text{ mA}/\text{cm}^2$.

3. Characteristic

3.1 Substitute Circuit Diagram

The solar cell is a source of current. The optically impressed current I_E has the direction of the inverse current during the pn-transition. The resistance in the external circuit causes a loss of power which poles the pn-transition in the forward direction. A part of the impressed current is thus lost as "diode forward current" corresponding to the dark characteristic of the pn-transition. The impressed current is thus distributed over the external working resistance and over the internal pn-transition poled in the forward direction. The first partial current shall be called the working current or current I from the solar cell for short. The second partial current shall be called diode current I_D . The change in the working resistance between 0 and infinity produced the solar cell characteristic. When idling the entire impressed current is used as diode current and thereby builds up the idling tension U_L . In case of short circuit the impressed current flows as short circuit current over the external circuit. The substitute circuit diagram for a solar cell is thus composed of a current source with a parallel switched diode (the pn-transition) as internal current loss branch and of the external resistance R_a . In this description we have not yet taken account of the fact that a part of the tension is already lost inside of the solar cell. We must therefore add to R_a an effective internal resistance R_i . Altogether we thus get

$$I_E + I_D + I = 0$$

where I_E is a negative value. The diode tension becomes

$$U_D = I(R_i + R_a) = U + IR_i$$

U being the external tension. For the diode current we can make the

Shockley statement

$$I_D = I_0 (e^{U/0} - 1)$$

where I_0 represents the saturation current in inverse direction and $\eta = \frac{kT}{Ae}$ the temperature tension (k Boltzmann constant, T absolute temperature, e elemental charge, A Shockley constant). The characteristic parameters

$$I_E, I_0, R_i \text{ and } A$$

can be deduced from measured characteristics. In the previous section we already gave a model theory for I_E . I_E and I_0 can easily be expressed in terms of short circuit current I_K and idling tension U_L . In case of sufficiently high insolation, I_K is smaller than I_E . The remaining parameters R_i and A could then be adjusted to obtain the measured optimum working point. This is the point on the characteristic curve having tension U_m and current I_m , at which the solar cell performs best. Tests have shown that although with the right parameters experimental characteristic curves can be excellently reproduced in their entire course the internal resistance R_i clearly comes out too small. For R_i can also be measured directly, for instance from the dark characteristic (given a sufficiently large current this is solely determined by R_i) or from two characteristics for different illuminations (that is various I_E)¹¹⁾. The substitute circuit diagram represented here cannot be used indiscriminately. This is why we used parameter R_i as experimental value in the characteristic curve adjustment and thereby obtained pretty nearly $A = 1$. The Shockley constant has therefore also been used in the following studies. In the characteristic curve adjustment, account was taken of the fact that the contact grid covers a part of the front of the solar cell, which means that I_E corresponds to a smaller surface than I_0 .

3.2 Effective Internal Resistance

The expected internal resistance can be estimated theoretically. For it is made up of the contact resistances and those of the grid fingers, as

well as the front and back layers of the solar cells. Contact resistances are not taken into account here. The back-layer resistance R_B depends on the specific resistance ρ_B of the basic material. The current distribution in the front layer is inhomogeneous. Because of the constant source current intensity on the surface the current intensity increases toward the grid fingers. Likewise the current in the fingers increases toward the contact collecting bar. The inhomogeneous current distribution results in an inhomogeneous distribution of the electrical field. These current- and field conditions can at best be made up by an effective component R_T to the internal resistance R_i , where $R_T = R_F + R_S$ (R_F finger resistance, R_S front-layer resistance). R_T is so chosen that the energy used up in the front-layer, inclusive of the contact grid, is restored. R_F depends not only on the specific resistance of the finger material but also on their number Z_F , their width F_B and their depth F_T . R_S is essentially determined by the measurable surface resistance ρ_S as well as by Z_F . For R_S we get a formula similar to the one of Wolf¹²⁾. To sum up we have

$$R_i = a \cdot R_T + R_B .$$

The factor "a" is so chosen that the experimental value for R_i is reproduced. In practice we get values for "a" between 1 and 2.

3.3 General Graphic Presentation

The model given for the internal resistance in the preceding section is necessarily very questionable and thus also the appurtenant substitute circuit diagram of section 3.1. The three-dimensional current distribution caused by the grid pattern should really be taken into account, but for practical purposes this would be much too complicated. But one could take into account a two-dimensional potential and current distribution in the front-layer of the solar cell and also the back-layer resistance R_B . The

tension at the pn-transition and with it the diode current density are locally different. Surface resistance ρ_s determines a differential front-layer resistance. A further possible simplification would consist in considering the potential and current distributions in direction of the contact fingers and vertical to them as independent from each other. But even such a simplified solar cell model does not seem to have been studied up to now. The next step consists in taking only into account a one-dimensional potential distribution in the front-layer: the potential will change between the grid fingers but not parallel to them. A loss of potential in the fingers is not taken into account (unless we subsequently add an effective finger resistance). This model was computed for various parameters by Beckmann¹³⁾. In the model in section 3.1 it is assumed that the potential in the front-layer is constant. The internal resistance or the losses of potential, particularly in the front-layer, have an increasingly unfavorable effect on the output of the solar cell at higher rates of insolation. For a theoretical treatment of a possible grid configuration at high insolation the substitute circuit diagram of section 3.1 is hardly satisfactory. In spite of this we shall use it for this very purpose because of its simplicity.

3.4 Grid and Insolation

The output of a solar cell at the optimum working point $N_m = U_m I_m$ should, with due allowance for certain secondary requirements, be as large as possible. In order to obtain this one must try to make the characteristic curve values, namely short circuit current I_K , idling tension U_L and curve factor $f = U_m I_m / U_L I_K$, as large as possible. As regards I_K it is important to keep the reflection and recombination losses small. We mentioned that already in section 1. U_L gains by heavy doping of the front and back layers of the solar cells. f is unfavorably influenced by internal resistance R_i .

The characteristic material and construction parameter of a solar cell, namely front-layer doping, front-layer surface resistance ρ_s , specific back-layer resistance ρ_B and the grid configuration, can have an opposite effect on the curve values. Moreover, secondary requirements impose limits on the material parameters. For example the front-layer doping is made as large as possible for the benefit of U_L . However, when considering the diffusion of the front-layer one should also take into consideration the crystal disturbances it causes which decrease I_K (section 1.3). ρ_s must be as large as possible in favor of I_K (section 1.4) but the operating dependability of the solar cell, particularly under higher temperatures, limits ρ_s . The back-layer doping is expressed by ρ_B . A decrease in ρ_B decreases I_K but increases U_L and reduces R_i . All in all, N_m is favored by a small ρ_B , but for reasons of radiation resistance ρ_B cannot become too small. R_i is in no way determined by ρ_s . That is why R_i does not limit ρ_s . But

ρ_s influences R_i . We shall consider the number of fingers Z_F as variable. The most unfavorable influence of a ρ_s value on R_i can thus be compensated by additional fingers. The surface covered by the contact grid decreases I_K . The true Z_F value therefore represents a compromise between a smaller R_i and a large I_K . We find that the value of ρ_s plays a subordinate role in this connection. The remark made above that ρ_s is not the determining factor for R_i is to be understood in that sense. As concerns the finger width F_B and the finger depth F_T , F_B should be as small as possible and F_T as large as possible. Smaller F_B would of course mean larger Z_F if the total finger conductivity and the loss surface are to be maintained. But in doing so R_i will be decreased. The smallness of F_B and with it the largeness of Z_F are limited on technological grounds. Larger F_T would improve the finger conductivity, at least for as long as the finger resistance still influences R_i . But F_T cannot exceed an acceptable measure in favor of

mechanically stable contacts with any given F_B . To be sure, the proper arrangement of a solar cell is a complex problem. However, if one establishes ϕ_S , ϕ_B , F_B and F_T on the basis of more or less arbitrary secondary conditions, there remains as an open parameter only Z_F . Since under conditions of higher insolation R_i reacts unfavorably on the working point the optimum Z_F will also increase with the insolation. On the basis of the model described in 3.1 and 3.2 N_m is computed as a function of Z_F for various temperatures. We get a more or less well defined maximum which always corresponds to the optimum Z_F . Starting point of the computation are cells with $Z_F=7$, $Z_T=2.2 \cdot 10^{-4} \text{ cm}$, $F_B = 1.35 \cdot 10^2 \text{ cm}$ as well as certain ϕ_S and ϕ_B values. I_K , U_L , and R_i are measured on normal cells given $\text{Ins} = 1 \text{ AMO}$ and a certain temperature. I_E , I_0 and the factor "a" in the expression for R_i are known, namely as a function of ϕ_S , ϕ_B and T depending on the normal cell type and the measurement temperature. Now we can calculate P_m under variation of Z_F , F_T and F_B . Higher insulations are introduced by means of $I_E \sim \text{Ins}$. The freezing of "a" limits the usefulness of the computation particularly, of course, in the case of high temperatures. See section 3.3. From this it will be noted that the results of the computations should only be looked upon as qualitative extrapolations.

4. Computation of the Grid Optimization

The grid form and the electrical characteristic values of type IV solar cells were made the basis of the optimization computation of the grid structure. These have the specific resistance $\rho_B = 10 \Omega \text{cm}$ and the layer resistance $\rho_S = 60 \Omega/\square$.

4.1 Finger Width

As the value to be optimized the maximum power output was chosen. The optimization was carried out in several steps. For a type IV cell with a finger depth $F_T = 2.2 \mu\text{m}$ we then took, at the standard measurement temperature of $+28^\circ\text{C}$, the maximum power computed as a function of the number of fingers, whereby the finger width varies as parameter. In addition to the standard finger width of $135 \mu\text{m}$ the computation was also carried out for half and double the standard finger width, namely for $67.5 \mu\text{m}$ and $270 \mu\text{m}$. As a further parameter the insolation was changed in five steps from 0.25 AMO to 15 AMO. With the smallest insolation of 0.25 AMO (Figure 4) the largest active surface brings the highest maximum power. The optimum number of fingers lies between 6 and 10. Figure 5 shows the conditions with an insolation of 1 AMO. The optimum of the maximum output shifts toward a higher number of fingers and becomes less well defined. It lays, for the standard finger width, between 6 and 12 fingers. With increasing insolation the maximum power increases about proportionally with the intensity. With 5 AMO (Figure 6) and with a number of fingers up to 12, the finger width has no influence on the power generated. With increasing insolation (Figures 7 and 8) the optimum shifts toward a greater number of fingers, that is to say, the series resistance decreases in the measure in which the contact surface increases and the active surface decreases. The optimum of the maximum output then moves to a finger number far removed from the most favorable number necessary for operation of solar cells near the earth.

Since, however, in the case of a solar probe, one and the same solar cell must operate with maximum efficiency both near the earth and near the sun and since, furthermore, the contact pattern must be technically feasible, the number of grid fingers that come into question, after this preliminary examination, must be on the order of a one digit number.

4.3 Finger Depth

A second step of the optimization computation keeps constant the finger width of $135\mu\text{m}$ and studies the maximum output as function of the finger number with the finger depth as parameter. As the contact pattern is produced by a vaporization process we have examined only finger depths of 1.1 to $4.4\mu\text{m}$ because greater finger depths appeared unrealistic. In case of small insulations the influence of the thickness of the contact fingers is small although it can clearly be recognized that even with an insulation of 1 AMO (Figure 9) the greater finger depth produces noticeably greater maximum outputs. The larger the striking solar intensity (Figures 10-12) the more noticeable becomes the possible power increase through greater finger depth. To sum up, we can say about the finger depth that it should be as great as the vaporization technique and the adhesive strength on the silicon surface permit.

4.3 Layer Resistance of the n-Layer

From the two optimization steps we find that a finger width of $135\mu\text{m}$ and a finger depth of $2.2\mu\text{m}$ represent favorable values for the design of a contact pattern. These two numerical values will be kept constant during the third optimization step. In this third optimization step we have again studied the maximum output as a function of the finger number varying the layer resistance of the thin, highly doped n-layer on the silicon surface. For type IV cells the layer resistance amounts to $60\ \Omega/\square$. We have

contemplated a reduction of the layer resistance for two reasons. The rough calculations described in section 2.4 concerning the influence of the thickness of the n-layer on the quanta yield of the solar cell and on the extra-terrestrial short circuit current density have shown that with decreased layer resistance accompanied by a greater n-layer thickness the diminution of the blue sensitivity and with it the decrease of the short circuit current density remain limited. A decrease in the blue sensitivity is of no particular concern for the simple reason that the glass covers and adhesives which are normally used have little transparency in space. It also appeared advantageous to increase the thickness of the n-layer as compared to type IV in order to delay, under high temperatures, the diffusion of the contact metals through the n-layer until it reached the pn-transition.

We have therefore constructed from various base materials of $10 \Omega \text{cm}$ and $1 \Omega \text{cm}$ silicon solar cells having a layer resistance of 60, 30, 15 and $6 \Omega/\square$. The measurement values obtained from these cells for short circuit current, idling tension and maximum output (Figures 13 - 15) formed the starting point for the further optimization computation. The maximum power yield as a function of the finger number was, in turn, studied for these 4 layer resistances as parameter for 3 different insulations between 1 AMO and 10 AMO. The result shows almost no difference when using layer resistances from 60 - $30 \Omega/\square$. A definite power decrease of over 10% can be noticed only when the layer resistance drops to $15 \Omega/\square$. Figures 16 - 18 would suggest the development of a solar cell, unaffected by changes of temperature, having a thicker n-layer.

4.4 p-Silicon with a Basic Resistance of $1 \Omega \text{cm}$

The fourth optimization step extends the analysis to p-silicon with a basic resistance of $1 \Omega/\text{cm}$. This low ohm basic material was chosen for

two reasons. A rough estimate of the annual equivalent dose of 1 MeV-electrons for the solar probe gives a low value of $10^{13} - 10^{14}$ 1 MeV-electrons/cm². From the standpoint of radiation resistance of the solar cells the use of low ohm silicon appears entirely reasonable.

The second reason concerns the production of a solar cell from low ohm silicon having a substantially greater idling tension and greater maximum output than conventional solar cells, considering the limited possibilities afforded by the small radiation. In the next numerical optimization step we have therefore examined the maximum output in relation to the finger number for 1 Ω . cm silicon as basic material with 4 different thicknesses of the n-layer as parameter. The results set down in Figures 19 - 21 for insulations of 1 AMO, 5 AMO and 10 AMO show qualitatively the same behavior as with higher-ohm basic material, except that the absolute amounts of the maximum output are considerably higher for low-ohm material than for high-ohm silicon.

From these 4 optimization steps it appears that a solar cell for a mission beginning near the earth and leading to the vicinity of the sun should be made from basic materials having a specific resistance of 1 Ω . cm. We should also increase the thickness of the n-layer until a layer resistance of 30 Ω/\square is reached. From the rough computations it appears advisable to maintain the same number of fingers which have already been successfully used on type IV, namely 7.

4.5 Spoolshaped Satellite Body

In a subsequent optimization step we have examined the behavior of solar cells, described in the preceding section, which have been placed on the two conical parts of a spoolshaped structure at an angle of 35°. This

geometrical arrangement had been planned for the solar probe project at the time we had reached this point in our optimization analysis.

At that time the satellite to be used in the project was to be in the form of a spool. The sunlight was to strike the spool perpendicularly to its axis. Because of the slant at which the light would strike the solar cells (planned maximum angle of incidence 35°) their warming up would be limited (planned maximum cell temperature 140°C) on the one hand and, on the other, the effective insolation would be decreased. The latter condition could be balanced by the stronger solar radiation nearer the sun.

Because of the slightness of the expected radiation damage of the solar cells we based our computation on back-layer material having a specific resistance of $1\ \Omega/\text{cm}$ which, compared to $10\ \Omega/\text{cm}$ material (as in type IV solar cells), promises greater efficiency. At the same time we reduced the front-layer resistance to $30\ \Omega/\square$ (compared to $60\ \Omega/\square$ in type IV solar cells). This hardly causes a loss of power but should result in greater dependability under high operating temperatures because of decreased layer resistance and greater thickness of the n-layer.

The question still remains regarding the proper design of the grid structure, more especially the number of fingers Z_F to be chosen. Since the spool rotates on its axis the angle of incidence at which the sunlight strikes a solar cell fluctuates between 0 and 35° of the supplement to $\pi/2$ of the vertex angle. One could now use a reduced insolation averaged over the spool rotation, corresponding to the existing distance of the helios-sun, in order to compute the corresponding average solar cell power as a function of Z_F . This was done for a few selected distances from the sun with a few finger depths as parameter (standard finger depth $2.2/u$) and is reproduced in Figures 22 to 24. Since, however, the increase in the

power output is less than proportional to an increase in insolation, particularly in the case of higher insolutions, one must really average the output over the rotation of the spool and, in doing so, one must always take into account the most favorable working point for every angle of incidence. Figures 25 to 27 illustrate the results so obtained. The power outputs so obtained are but slightly less than those obtained for the corresponding average reduced insolation value. This is understandable in view of the mentioned underproportionality. Averaging the outputs also results in somewhat larger optimum values for Z_F because it is obviously advantageous to take particular account of the angles of incidence corresponding to greater effective insolutions. Besides results for space temperature Figures 22 to 27 also show values for $+140^{\circ}\text{C}$. These are based on an assumed temperature behavior of the solar cells which was obtained through extrapolation by our own measurements of the temperature dependence up to $+80^{\circ}\text{C}$. Published figures of the characteristic data of solar cells approximately agree with the extrapolated data. On the one hand, the output of the solar cells increases as it approaches the sun because of the stronger solar radiation and, on the other hand, it decreases because of the resultant heating. One should really deal simultaneously with the heat balance and with the related energy output of the solar cells.

From Figure 27 it will be seen that despite the high solar cell temperature of $+140^{\circ}\text{C}$ in the vicinity of the sun, owing to the high insolation, a mean power output can be made available which is far above the one obtainable near the earth. Consequently it appears useful to choose the still open finger number in such a way that an optimum output is reached near the earth. Figure 25 shows that for a temperature of $+28^{\circ}\text{C}$ the optimum number of fingers is from 6 to 7.

4.6 Cylinder-shaped Satellite Body

In the meantime, the concept of the solar probe has changed to the extent that instead of a spool-shaped, a cylindrical shape is being considered. That is why we have repeated the optimization computations for the new concept. In addition, the requirement was set that the mean temperature of the solar cells should be -64°C near the earth and $+140^{\circ}\text{C}$ at a distance of 0.3 astronomical units from the sun. We have therefore computed the mean output at the optimum working point as a function of the finger number using selected working temperatures and 2 finger depths as parameter. The averaging of the output extends over the lighted half-revolution (Figures 28 - 31). Figure 28 shows that near the earth, during the lighted half-revolution and with a temperature of -64°C , there is available a mean output at the optimum working point of about 55 mW per cell. The optimum of the output curve runs flat between 4 and 9 fingers. There are no noticeable differences in the case of finger depths between 2 - 9 μm . Near the sun (Figure 31) the increase in the radiation intensity of the light far surpasses the decrease in output caused by the high operating temperature. Therefore it seems advisable to design the solar cell in such a way that it will give as large an output as possible near the earth and at the same time be able to withstand the high operating temperature near the sun. The study of solar cells under high temperatures will then be an object of the experimental program.

4.7 Result of the Optimization Computation

The optimization computation for type V solar cells resulted in the following characteristics: specific resistance of the basic material $1 \Omega\text{cm}$. Layer resistance of the n-layer $30 \Omega/\square$. Titanium-silver contacts. Finger depth about 4 μm . The finger arrangement, in width and number, corresponds

to type IV with 7 contact fingers. This contact arrangement was chosen because the optimization computation had shown that it produced a maximum output near the earth.

5. Production of Type V Solar Cells for Solar Probes

The construction of type V solar cells is primarily based on the guidelines furnished in research report BMwF-FB RFT 3013¹⁴⁾ dated 23 December 1967. (Title of the report: Further Development of n/p-Silicon Solar Cells with particular regard to the use of silicon tissue.) The method of construction outlined in that report should be amended as follows:

2.1.1 Basic Material

Wacker-Chemie GmbH, Munich furnished square lamella lapped on both sides. Length of edges 20.8 ± 0.05 mm. thickness 0.365 ± 0.015 mm. Material: high purity silicon, monocrystalline, crucible pulled, p-conductive, (B-doped), orientation 111, maximum deviation 1° , specific resistance $1 \Omega \text{cm} \pm 30\%$ EPD max. $10,000/\text{cm}^2$.

2.1.2 not applicable

2.1.3 Cleaning and Treating

The lamella are treated under room temperature with ultrasonics for 3 x 5 min in carbon tetrachloride and for 2 x 5 min in acetone. This is followed by a two hour bath in a 50% KOH* solution at 70°C .

2.1.4 Diffusion

Immediately prior to diffusion the lamella are immersed for 3 min in a 38% solution of hydro-fluoric acid, then rinsed in distilled water, methanol and a saturated solution of iodine in methanol.

$(\text{NH}_4)_2\text{HPO}_4$ p.A. that has been disintegrated in advance in a separate oven at a temperature of 500°C for a period of 10 min is used as source; the weight of the sample is 2 g.

* KOH - probably carbon hydroxyl (translator's note)

The diffusion requirements are:

10 min at 900°C, rapid cooling (4°/min) to 750°C, getter 1 hour, rapid cooling to room temperature. Carrier gas is N₂/O₂ in a ratio of 3/1 with a velocity of about 120 l/hour. The source temperature is about 760°C.

The basis for the choice of the diffusion time and temperature is the layer resistance which is measured on the cells after removal of the glass layer which is formed during the oxydating diffusion. It should be on the order of $30 \pm 3 \Omega$.

2.1.5 Removal of the Glass Layer

Not applicable at this point. See under 2.1.7.

2.1.6 Lapping of the backside

For the removal of the backside the diffused Si-lamella are cemented on glass with Zeiss wax under high temperature. Then follows grinding with PWS 12. The last 20 μ m lapping at the final measurement are removed with BG 8. Then the lamella are polished with Aerosil and 2 n - NaOH. The caustic soda is removed with a brush under running water.

2.1.7 Vaporization of the Contacts

In place of cleaning in RBS a cleaning in a 20% detex 11 solution at 40°C takes place.

Shortly before placing the lamella in the vaporization apparatus the glass layer is removed on the n-side by treating in a 38% solution of HF.

The (Ag) weight of the sample at the time of vaporization of the contact fingers is 2 g.

2.1.8 Annealing of Contacts

The annealing temperature was reduced to 500°C.

During the period covered by this report 500 type V solar cells were produced by this process. These were used by the firm Mtt.-Boelkow in the measurements to be described later on and for the module construction tests.

6. Measurement of the Quanta Yield on Type V Solar Cells and Production of a Standard Cell

6.1 Measurement of the Quanta Yield and Computation of the Extraterrestrial Short Circuit Current

The quanta yield is a function of the wave length of the incident light. It is defined for a given wave length as the quotient of the number of the electron-hole pairs separated during the pn-transition and the number of light quanta striking the solar cell.

With a monochromator the quanta yield is determined in any selected units. A vacuum-thermo element, whose relative spectral sensitivity was determined by the PTB*, serves for measuring the intensity. The absolute measurement of the quanta yield is done under high intensity with 5 interference filters of various transmission wave lengths. Here, intensity is measured by means of a solar cell that had previously been carefully calibrated with a thermopile.

An EDV 2002, which also analyzes the individual measurements, equates the relative measurement with the absolute measurement using the method of the least squares. At the same time a tape perforator is used to give the necessary instructions to the drawing board which graphically records the course of the quanta yield.

During the same process of calculation the quanta yield and the extraterrestrial solar spectrum are made to yield the extraterrestrial short circuit current for the corresponding solar cell.

Systematic errors may occur during the absolute measurement of the intensity and the extraterrestrial solar spectrum on which it is based¹⁵⁾. But a check for such errors seemed to be unnecessary at this time since in 1967 control measurements were carried out by NASA which duplicated our results.

* could be Physical-Technical Federal Office (translator's note).

In addition, we were able to make measurements on a Heliotek-Standard Cell No. 1082 placed at our disposal by Mtt.-Boelkow. Heliotek gives for this cell two extraterrestrial short circuit currents, obtained through various extrapolations, which vary by 1.5%. Our measurement fell between the short circuit currents given by Heliotek.

In connection with the work done here, comparative measurements to be carried out by JPL on balloon borne type IV cells will show to what extent the calculated extraterrestrial short circuit current still agrees with experimental values.

6.2 Measurement of the Quanta Yield on Type V Solar Cells

Test measurements of the quanta yield on type V solar cells resulted in a course which is pictured in Figure 32, together with the quanta yield curve of the standard type IV cell. The graph shows that it is specifically in the red part of the spectrum that the deviations are the greatest. However, since this part of the spectrum is not approximated very well by the simulator this deviation makes it necessary that we have a special standard type V cell.

6.3 Production of a Standard Type V Cell

From a standard cell it is required that it show about the same course of the quanta yield as the solar cells to be measured, taken as a whole. Only then do the deviations of the simulator spectrum from the extraterrestrial solar spectrum have no effect on the result of the measurement.

For this reason, the solar cells to be used as possible standard cells should be so selected from the total type V cell production that their electrical characteristics closely match the mean values of the total body of cells. On each of the selected solar cells there will then be made at least three measurements of the quanta yield and of the extraterrestrial

short circuit current. That cell, whose individual measurements most nearly approach the average, will then be chosen as standard cell.

6.4 Mathematical Corrections on the Measured Electrical Quantities

If further research should show that a basic standard measure should be changed the values measured up to that time could then be mathematically corrected.

The dependence of the idling potential and maximum output on the short circuit current was derived from two type V solar cells which, in their characteristics, corresponded to the mean value of the cells as a whole. Within the examined limits between 130 and 142 mA the relation is linear. For the coefficients we get the following:

$$\frac{\Delta U_L}{\Delta I_K} = 0.2 \left[\frac{\text{m V}}{\text{m A}} \right]$$

$$\frac{\Delta N_{\max}}{\Delta I_K} = 0.50 \left[\frac{\text{m W}}{\text{m A}} \right]$$

To set the desired intensity a standard cell was used which, because of the energy input to be expected under high insolation, had been soldered to a block through which flowed water at 28°C. This standard cell was mounted, together with the high temperature measurement mounting, on an alternating sliding carriage and could thus be brought to the measurement site in a reproducible condition.

Insolations as high as 11 AMO could be achieved through changes in construction. This was done by moving the measuring system closer to the xenon lamp housing whose mirror adjustment was varied accordingly. The filter for the xenon spectrum adjustment was not used during the measurements with high insolation.

The homogeneity of the illumination was checked with a photo element BPY 11 (measuring 2 mm x 3.5 mm). With a lamp current of 40 A the maximum deviation was 10%; with a lamp current of 60 A a maximum of 3% from the mean value.

Figures 41 to 49 give the family of characteristics in the range of temperatures from +28°C to +215°C for 9 different insolations up to 11 AMO. The temperature curves of short circuit current, idling potential and maximum output are shown in Figures 50 to 52 for 1 AMO and in Figures 53 to 55 for insolations up to 11 AMO.

From Figures 50 to 52 we get, for an insolation of 1 AMO and temperatures above 28°C, the following temperature coefficients:

$$\frac{\Delta I_K}{\Delta T} = + 0.046 \left[\frac{\text{mA}}{^\circ\text{C}} \right]$$

$$\frac{\Delta U_L}{\Delta T} = - 2.15 \left[\frac{\text{mV}}{^\circ\text{C}} \right]$$

$$\frac{\Delta N_{\max}}{\Delta T} = -0.27 \left[\frac{\text{mW}}{^{\circ}\text{C}} \right]$$

The connection between temperature and idling potential or maximum output is linear. In the case of the short circuit current (Figure 50) this linear relationship exists only up to about +170°C. Above this temperature the short circuit current increases more slowly. The temperature dependence of the short circuit current is so small that the observed deviation from linearity almost falls within the test limits for precision. The cause of the deviation from the straight line is not entirely explained. Presumably the simulator spectrum may account for it. Earlier measurements of the quanta yield up to about +80°C showed that in case of higher temperature the long-wave decrease in the quanta yield curve is shifted toward greater wave lengths. But since it is precisely for greater wave lengths that the simulator spectrum deviates substantially from the solar spectrum (xenon lines and filter for the suppression of xenon lines), the intensity set with a standard cell of +28°C did not necessarily correspond to the true value.

7. I/U Characteristics of Type V Solar Cells under Temperatures Ranging from -190°C to $+200^{\circ}\text{C}$ for Insolations between 0.5 - 11 suns.

7.1 Standard Requirements 28°C , 1 AMO

The solar cell is illuminated with the light of a xenon high pressure lamp XBO 1600. The lamp is housed in a commercially obtainable lamp housing (Bauer BL 11 X 2/1). The current supply was provided by a thyristor controlled power pack which keeps constant optionally either the lamp current or the light intensity at the place of measurement. The xenon spectrum is fitted with a T 6 filter made from polished tempax (produced by Jenaer Glaswerke Schott u. Gen., Mainz). The spectral course of the filter's transparency remained unchanged within the ¹⁰⁰precision limits of the test during the entire measurement operation.

The light intensity was set with the standard cell for type IV solar cells. Since the spectral course of the quanta yield from type IV and type V solar cells differs only negligibly (see Figure 32) this procedure appears justified. Furthermore, standard cells for type V became available only toward the end of our research and it did not appear advisable to change standards during the measurements.

For electrical measurements we used a measurement hookup with auxiliary current source which permitted the exact determination of the short circuit current during vanishing cell potential. For the current and potential ¹⁰⁰measurement separate lines were always used. Through changes in the cell potential from 0 up to the idling potential or in the cell current from the short circuit current to 0 the entire I/U characteristics can be traced. Measurements were made with a digital voltmeter and an X-Y recording apparatus. For simplified evaluation graph paper was used which, besides the I/U net, bore a family of hyperbola with curves of constant output.

I/U characteristics were recorded for all type V solar cells. The statistical evaluation by means of frequency distribution gave the median values for I_K , U_L and N_{max} . The cells on which the special measurements were made were so chosen that their electrical data approached as closely as possible the median values of all cells.

7.2 Temperatures under 28°C, Insolation 0.5 to 1 AMO

Because of the expected condensation of water vapor the measurements were carried out under low temperatures in a vacuum apparatus. The cell to be measured is pressed, in the apparatus, on a metal block of great heat capacity which provides good electrical and heat contact. This block can be cooled with cold gaseous or liquid nitrogen and warmed with hot compressed air. The great heat capacity of the set-up guarantees the necessary constant temperature during measurements. The temperature was constantly controlled by means of an iron-constantan - thermoelement with reference junction in melting ice.

With the measuring arrangement that was used it was not possible to bring optionally to the place of measurement either a standard cell or the cell to be measured. The proper intensity was therefore set by means of an auxiliary standard cell. For this purpose, the previously routinely determined short circuit current was set on the cell to be measured prior to cooling. Then the auxiliary standard cell was affixed in the path of the rays in front of the low temperature measuring apparatus for the purpose of determining the short circuit current. This short circuit current served to control the insulations to be used during the measurements.

In the course of the measurements it became obvious that the initial value of the idling potential was somewhat higher than the value shown in the I/U curves. The cause for this is to be found in a warming up of the solar

cells. In order to eliminate this error at the time of temperature determination the initial idling potential was plotted against the temperature. From this graphic presentation it was then possible to coordinate the proper temperatures with the stationary idling potentials and their resulting I/U characteristics.

The irregular course of characteristics that occurs with low temperatures in the vicinity of the idling potential is apparently connected with the current and charge carrier distribution inside of the solar cell, more especially in the front layer. During idling, when the contact grid draws no current, a certain recombination mechanism is weakened. This is why the idling potential appears magnified.

Figures 33 to 35 show current potential characteristics for insolarations of 0.5; 0.75 and 1 AMO for various temperatures down to -196°C . Figures 36 to 38 show the evaluation of the family of characteristics in terms of temperature dependence on short circuit current, the initial value of the idling potential and the maximum output.

7.3 Temperatures above 28°C , Insolarations up to 11 AMO

The measuring hookup for high temperatures also contained a metal block with a high heat capacity which could be heated electrically by means of soldering iron cartridges. The metal block was shielded by a double-walled metal pipe against contact and heat loss through convection. A small metal solar cell carrier could be clamped on the large metal block. The solar cell was fastened onto the carrier with a silver bearing solder (melting point 225°C), so that good heat contact was always assured. The temperature of the solar cell carrier was constantly controlled by means of an iron-constantan thermoelement (see Figures 39 and 40).

8. Endurance Tests on Type V Solar Cells under Temperatures to 515°C in a High Vacuum and under an Inert Gas.

The success of a mission near the sun makes it imperative that the solar cells used can be stored successfully over a longer period of time under high temperatures. In order on the one hand to reduce the storage times that cause a certain damage and, on the other, to gain information on the behavior under high temperatures the tests were conducted under various temperatures. The latest known version of the satellite anticipates stationary temperatures of +140°C, so that even the lowest tested storage temperature of +200°C still affords a sufficient security margin. Since 200°C is also the temperature which most nearly approaches reality, this test was conducted in the only available high vacuum apparatus. Other storage tests were conducted under temperatures of 300°C, 400°C and 515°C in a flowing argon-hydrogen mixture (90 : 10).

In all storage tests the solar cells were placed in space saving quartz brackets in a quartz tube which during the high vacuum test had been reduced to a pressure below $5 \cdot 10^{-6}$ Torr. During the protective gas tests the gas was cleaned in a molecular sieve before being led through the quartz tube. The quartz tube was sealed off from the room atmosphere by a wash bottle.

In all ovens used the constant temperature zone was measured. The temperature fluctuations caused by the adjustments were less than 5°C for high temperatures and less than 2°C for lower temperatures.

For the 4 storage tests the solar cells were chosen from 4 different batches. Six solar cells from each batch were allocated to each test, with the solar cells of each batch being distributed alternately over the 4 storage tests so that all storage tests had comparable collective values. A total of 96 type V solar cells were subjected to these storage tests.

As the solar cells that were used were subject, in their electrical properties, to statistical fluctuations, the electrical characteristic quantities relative to their initial values were determined after every measurement. These values, expressed in percentages, were determined for each batch and were graphically represented.

At 200°C (Figure 56) the solar cells from all batches behave similarly. After a storage time of 1743 hours the decrease in output at the optimum working point is about 3.4%.

At 300°C (Figure 57) the various batches show marked differences. After 1600 hours the maximum output has decreased, according to the batch, from 8 to 16%. The fact that the idling potential is also reduced suggests that the cause of the decrease may lie in the formation of leaks. Experiment shows that this damage ceased after 800 hours and that thereafter the solar cells again produced a constant output.

The tests at 400°C (Figure 58) and 515°C (Figure 59) show the same tendency, except that the time intervals for a still acceptable rate of damage are considerably shorter. Here also the short circuit current remains virtually constant, while the idling potential is decreased and with it also the output, presumably because of leaks. The important thing, however, that these experiments have shown is that in the event of solar eruptions the solar cells are capable of taking substantially higher temperatures, over short periods of time, without losing their ability to function.

9. Storage Tests of Type V Solar Cells in an Extremely Humid Atmosphere.

During assembly, during transport and at the start of a satellite the solar cells may be exposed to a humid atmosphere which may possibly cause corrosion of the contacts. The following tests are designed to show that this type of damage does not occur in type V solar cells. The assumption, that the cells are insensitive to humidity seems to be borne out by the fact that during one of their construction phases they were placed in boiling water for 15 minutes for cleaning after contact vaporization. (See construction regulation BMwF-FB RFT 3013, Section 2.1.9).¹⁰⁰ To be sure, however, three different humidity tests were carried out. The type V solar cells were taken from 3 batches, from each batch 3 cells were picked for each test in alternating sequence, so that we again had at our disposal 3 comparable collectives with a total of 27 type V cells. The evaluation and graphic representation of the results is similar to the description in section 8.

9.1 Boiling Water Test

During the boiling water test the solar cells were boiled in water for 8 hours, with hourly interruptions for a control measurement. After about 4 hours some damage appears. The similarity in the decline of the short circuit current and of the maximum output (Figure 60) is evidence that this is due to damage to the tempering layer. The control of the series resistance, which remained unchanged even after being boiled for 8 hours, confirms this assumption.

After concluding the test, one cell from each batch was subjected to rupture tests with soldered wires. The front and back contacts behaved like those of new cells. The rupture point of a wire, which had been soldered flush with a speck of solder of 1 mm diameter, was in all but one case greater than 2000 p. In the exceptional case the silicon tore loose at 1600 p.

9.2 Water Vapor Test

A water vapor test was conducted during 112 hours. The solar cells were set upright in small baskets suspended in a beaker over boiling water. Here too the damage affects the tempering layer. Short circuit current, maximum output and, in case of heavy damage, the idling potential as well (Figure 61) act as if the cells were exposed to a reduced illumination. The damage between 75 and 112 hours drops out of the expected curve. The cause has not yet been fully explained. But it is assumed that during this period of time the temper of the cells suffered particular damage through dripping condensed water. This suspicion is reinforced by the fact that the cells that suffered the greatest damage to their electrical values also showed the greatest change in the tempering surface (Figure 62).

9.3 Humidity Test

In a humidity test, solar cells were stored for a total of 1475 hours at 80°C and 80% relative humidity. During this test the solar cells were placed in a closed glass container in a drying closet at 90°C. The container held a saturated KCL solution. With this arrangement we find a relative humidity of about 80% (W. Lueck, Humidity, R. Oldenburg, Munich, Vienna 1964; D'Ans-Lax, Notebook for Chemists and Physicists, Springer Verlag, Berlin, Heidelberg, New York 1967).

The electrical characteristics remained unchanged during the period of the tests (see Figure 63).

9.4 Tape Test

A tape test that was made on cells from the humidity test, after 1550 hours had gone by, showed good results for cells from 2 batches. Contact fingers and tempering layer remained undamaged. In the case of cells from the third batch the beam suffered damage where, during control measurements, the contacts touch down; in addition, one finger came loose.

10. Radiation Resistance

As an orientation test a one-time radiation of 8 type V solar cells from two different silicon sticks was carried out with 10^{15} 1 MeV-electrons/cm² 16). Immediately after radiation the degradation of the short circuit current, idling potential, maximum output, curve factor and internal resistance were determined. The results are given in Table 2. The degradation of the short circuit current amounts to 19% (17%), of the idling potential 9% (10%), of the output under optimum adaptation 27% (25%). The values given in parentheses are our measurements of the degradation of type IV solar cells. From the orientation tests made so far the degradation values for short circuit current and output are only slightly larger for type V than for type IV. The idling potential is less radiation sensitive. The slight change in the curve factor can be explained by its intensity dependence. The series resistance of the solar cells has not changed within the limits of measurement accuracy.

Generally valid statements concerning the radiation resistance of type V can only be made after the completion of a step by step radiation. These experiments could not, however, be conducted because of lack of time. Considering the increased temperature during a mission near the sun the repair of the radiation damage should also be studied.

Table 2. Electrical Characteristic Values of Type V Solar Cells before and after Radiation with 10^{15} .

Cell	I_K [mA]		U_L [mV]		N_{max} [mW]		K [%]		R_i [m Ω]	
	Before	After	Before	After	Before	After	Before	After	Before	After
301 T 72	136,0	109,7	598	545	64,0	46,1	78,7	77,2	140	150
73	134,0	107,4	595	543	62,5	45,2	78,4	77,4	130	140
74	133,9	107,3	594	542	58,5	42,2	74,0	72,5	150	180
75	133,4	107,2	595	543	60,4	43,9	75,9	75,3	120	150
302 T 44	134,9	109,3	597	542	59,0	43,0	73,2	72,6	150	140
45	135,3	109,7	597	543	60,9	44,3	75,3	74,4	110	120
46	135,4	108,9	598	543	61,8	44,9	76,1	76,0	140	140
47	135,6	109,8	596	542	60,1	44,8	74,4	75,5	140	140

11. Results

11.1 Comparison of Computation and Test

After obtaining the measurement values of type V solar cells for a wide range of temperature and insolation we shall now compare the theoretical optimization analysis with the experimental findings. The result of the optimization computations was recorded in Figures 29 - 32. Near the earth the computation of the mean output was based on a reduced insolation for the lighted half-rotation of a cylinder of 0.64 AMO (Figure 28); on the way to the sun at a distance of 0.5 AE one of 2.55 AMO and, near the sun, at a distance of 0.3 AE one of 7.07 AMO. The values obtained experimentally for the maximum output are shown, dependent on temperature and insolation, in Figures 38 to 55. The results of experiment and computation are compared in Table 3.

The consistency of the computed and measured values is surprisingly good. It is only for the first value in Table 3, which is of no practical importance as far as the solar probe is concerned, that experiment and computation differ. In this case, during the integration of the available output, the loss connected with the higher output weighs more heavily in the calculation than it would have if the computation had been done for a median insolation constant in time. The conformity of the 5 remaining pairs of values is more than satisfying. The experiments thus confirm that the theoretical optimization not only describes qualitatively the properties of type V solar cells but also gives usable quantitative results.

Table 3. Comparison of the outputs computed and measured for various insulations and temperatures.

r (AE)	Ins (AMO)	T (°C)	N _{max} (mW)	
			Computation	Experiment
0.3	7.07	28	380	480
0.3	7.07	140	190	210
0.5	2.5	28	165	150
0.5	2.5	140	90	88
1.0	0.64	28	40	37
1.0	0.64	-64	55	48

11.2 Families of Characteristics

The properties of type V solar cells are shown in the family of curves in Figures 33 - 55 for a range of temperatures and insolutions that either graphically represents all possible pairs of values of temperature and insolation for the mission of a solar probe or makes it possible to arrive at them quite easily through interpolation.

11.3 Temperature Coefficients

In the temperature range of -64°C to $+140^{\circ}\text{C}$ which comes into consideration for the solar probe the temperature coefficient of the idling potential is constant at $-2.1 \text{ mV}/^{\circ}\text{C}$ for all insolutions between 0.5 - 11 AMO. The temperature coefficient of the short circuit current depends on the insolation. It is very small for small insolutions and amounts to about $0.05 \text{ mA}/^{\circ}\text{C}$ for insolutions up to 1 AMO; it shows a linear increase from $0.3 \text{ mA}/^{\circ}\text{C}$ for 4 AMO to $1.1 \text{ mA}/^{\circ}\text{C}$ for 11 AMO. The temperature coefficient of the maximum available output also depends on the insolation. At 1 AMO it amounts to $0.23 \text{ mW}/^{\circ}\text{C}$ as for type IV and then climbs somewhat faster than proportional to the intensity to values of about $3 \text{ mW}/^{\circ}\text{C}$ for 11 AMO. For insolutions over 6 AMO a slight dependence of the temperature coefficient on the temperature becomes apparent. Aside from the aforementioned deviations in the zone of high insolutions, the type V solar cell under the normal intensity of 1 AMO has a linear temperature coefficient in the entire range of temperatures with which we shall have to deal.

11.4 Series Resistance

The measurement of the series resistance of type V solar cells confirms the correctness of the theoretical considerations. The smaller specific resistance of the initial silicon and the smaller resistance of the n-doped layer taken in conjunction with the most favorable geometric form of the

contact grid produce a series resistance in the range of 100 m Ω .

Figure 64 reproduces a portion of the I/U characteristic curve used for the determination of the series resistance. For the sake of clarity the potential scale was considerably extended on the abscissa axis while the ordinate scale remained unchanged. For the determination of the series resistance, with varying intensity of the incident light, two curves are drawn whose short circuit currents differ by ΔI . The series resistance, under the higher intensity, causes a shift in the I/U curve of ΔU at a distance ΔI from the abscissa axis. The quotient $\Delta U / \Delta I$ gives directly the internal resistance. In routinely drawn curves the difference in potential of 5 mV shown in Figure 64 corresponds to a length of 2 mm.

With solar cells having such small series resistance as in type V routine measurements of the internal resistance cannot be made with an accuracy greater than 10%. But it can be determined with certainty that the series resistance in the case of type V is smaller than in the case of type IV by a 3 factor.

11.5 Constancy

The soft-solder-free contacts required for solar cells with high operating temperatures demand stable solar cell properties under humid storage conditions. These difficult requirements do not appear during the course of the mission but during the construction phase of the satellite. We have therefore conducted three different types of humidity tests with type V cells and have extended these tests far beyond the normal time limits. As a result it can be stated that the titanium-silver contacts produced by us have proven themselves to be humidity-proof. The storage tests at +200°C show that the formation of leaks at the p/n transition can be avoided by

choosing a smaller layer-resistance and thus a greater n-layer thickness.

Our original intention, through storage tests at various high temperatures and measurement of the time necessary for the formation of similar leaks under different temperatures, to compute a diffusion constant that might underlie this process, could not be realized. Storage tests at temperatures of $+300^{\circ}\text{C}$ show clearly that the formation of leaks stops after a certain time. From measurements, made up to now, of the decrease in maximum output that we have for periods up to 1600 hours it may easily be extrapolated that under operating temperatures of $+140^{\circ}\text{C}$ maximum output will in no way be influenced by the formation of leaks.

To sum up it can be stated that type V cell, because of its small series resistance, its optimized grid shape and because of its low-ohm basic material, its 10% higher idling potential as compared to normal cells, can produce about 6% greater output than normal cells. The degradation measurements at hand clearly show that up to equivalent doses of 10^{15} 1-MeV-electrons type V cells are equal to normal cells. Under extreme conditions of use, operating temperatures as high as 140°C are feasible.

11.6 Power Output during the Mission

For rational planning and for the successful accomplishment of a mission it is of considerable importance to know what output is available at any particular time. Since the available output depends on the solar cell temperature and insolation the prerequisite for such estimates is the knowledge of the solar cell temperature.

Figure 65 shows the functional relation of solar cell temperature and the distance between the sun and the probe. The Figure was taken from a Dornier study, based on the assumption of a double cylinder shape with a

40% degree of coverage. For the sake of simplicity the insolation chosen was always the average insolation during a half-rotation at a given distance.

From the I/U curves for various insolations and temperatures (Figures 33 - 35, 41 - 49) the pertinent output values could now be taken for various distances between the sun and the probe. Figure 66 shows, for various given cell potentials, the available outputs in relation to the distance sun - probe. Figure 67 is the corresponding representation for the output at the optimum working point. This shows that the bottleneck of the energy supply is near the earth and that the energy need and the energy supply must be planned accordingly.

Bibliography

- 1) E. Muller, E. Klippel, K. Einfeld, RF 93-0 DGLR-Nr.68-003
DGLR-Symposium 1968 Munchen
- 2) Bir und Pikus, J. techn. Phys. 27 (1957) 467
Wolf, Proc. IRE 48 (1960) 1246;
Loferski u. Wysocki, RCA Review (1961) 38
- 3) Subashiev, Fiz. Tv. T. 2 (1960) 205
- 4) Dubrovskii und Subashiev, Fiz. Tv. T. 2 (1960) 1562
- 5) Subashiev, Dubrovskii u. Petrusevich, Fiz. Tv. T. 2 (1960) 1978
- 6) Pfleiderer, Siemens Report (1967)
- 7) Altshuller, Fiz. Tv. T. 10 (1968) 1136
- 8) John, Proc. IEEE 55 (1967) 1249
- 9) Wolfgang, Abraham und Inskeep, IEEE Transactions Nuclear Science (1966) 30
- 10) Queisser and Guettler, Conference Report (1969)
- 11) Wolf, Rauschenbach, Adv. Energy Conv. 3 (1963) 455
- 12) Wolf. Proc. IEEE 48 (1960) 1246
- 13) Beckmann, J. Engineering for Power (1969) 415
- 14) T. Renner, A. Mueller, Further Development of n/p-silicon solar cells,
particularly in regard to the use of silicon webs, BMwF-FB RFT 3013 (1967)
- 15) F. S. Johnson, J. Meteorology 11 (1954) 431
- 16) K. Wohlleben, R. Bauerlein BMwF-FB-RV 1-624/19/66 (1967)

12. Computation of the Radiation Charge and the Equivalent Dose

Summary

The expected radiation charge of the solar probe planned for the year 1972 will be relatively small. For example, the yearly equivalent dose of a 1-MeV-electron test radiation, to simulate the damage to 10- Ω cm-Si-n/p solar cells behind a 50 μ m thick covering glass layer, amounts to about $5 \cdot 10^{13}$ e/cm², which - without taking into account a possible healing - occasions a degradation of the maximum power output of the solar cell of about 7 to 8%. Of this equivalent dose 77% are due to the charge along the heliocentric course from the solar cosmic protons emitted during solar eruptions. The rest is due to the protons of the Van Allen belt during the ascent. The charge caused by the electrons of the Van Allen belt is negligible. In the case of covering glass layers of more than 100 μ m thickness the portion due to the Van Allen protons is less than 10%.

The radiation charge of the solar probe is made up of the charge of the protons and electrons of the Van Allen belt during the ascent phase and the charge of the solar cosmic protons (solar flares) along the heliocentric course.

12.1 Radiation Charge on the Ascent through the Van Allen Belt

The firm of Boelkow furnished us with a table showing, for distinct times t_i during the ascent phase, the attained height H_i of the satellite as well as the geographic coordinates (geographic longitude φ_i and geographic latitude ψ_i) of the subsatellite point ¹⁾. At the same time we obtained maps with the geomagnetic coordinates for a pure dipole field, that is one showing the real magnetic inclination at the earth's surface in relation to the geographic coordinates.

With the aid of these maps we determined first of all the geomagnetic latitude λ_i corresponding to the geographic coordinates $(\varphi, \psi)_i$ of the sub-satellite point. This was based on the tables of NASA (see below) and, after consultation with the firm of Boelkow, the map for a pure dipole field of the earth (valid from about 1000 km). With a newly plotted computer program SATBN3 (written in FORTRAN IV) we then calculated for the coordinates $(H, \lambda)_i$ the McIlwain ²⁾ trajectory parameter L_i and the force B_i of the geomagnetic field for the relevant point in space according to

$$L_i = \frac{R_e + H_i}{R_e \cos^2 \lambda_i} \quad \text{with } R_e = 6371.2 \text{ km (earth radius)}$$

$$B_i \text{ (Gaub)} = \frac{8.06 \cdot 10^{10} \sqrt{1 + 3 \sin^2 \lambda_i}}{(R_e + H_i)^3}, \quad R_e, H_i \text{ in km.}$$

After this we determined, through a 4 point interpolation ³⁾ of the NASA data, recorded on magnetic tape, for the spatial and energy distribution of the protons and electrons in the radiation belt (up to a maximum height of 36,000 km), the spectra of both particles at each of the i points in the

L,B space and namely for 21 proton energies between 0.4 and 500 MeV and 29 electron energies between 0 and 7 MeV. Then the individual spectra from all the points of the trajectory were added up, using as weight factor of the i-th spectrum the time factor $\Delta t_i = \frac{1}{2}(t_{i+1} - t_{i-1})$.

The firm of Boelkow furnished the coordinates $(t, \varphi, \psi, H)_i$ for 4 different ascent trajectories¹⁾:

Trajectory A	Starting time	5.86 W.Z.*	Parking height	200 km
" B	" "	16.75 "	" "	200 km
" C	" "	5.81 "	" "	185 km
" D	" "	16.74 "	" "	185 km

(most recent situation)

Since the ascent trajectory has apparently not yet been definitely fixed, the integrated particle spectra were calculated for all 4 trajectories. Chart 1 shows the result. From this it will be seen that trajectory B furnishes the highest fluence both for protons and electrons since this trajectory runs generally speaking in lower geomagnetic latitudes and therefore closer to the center of the Van Allen belt. For electrons there is, however, only a slight difference between the various trajectories. The main contribution to proton radiation takes place at heights between about 4000 and 7000 km (corresponds to a flight time of about 5.3 min). In the case of electrons the major portion is integrated between 10,000 and 20,000 km (flight time about 16.6 min).

In order to be on the safe side when making estimates of the expected radiation charge subsequent calculations were based on the spectra along trajectory¹⁰⁶ B. With the aid of the already described computer program⁵⁾ the spectra for protons and electrons were computed, after shielding, for 10 shielding thicknesses between 0.01 and 10 g/cm² and then the absolute damage

* W.Z. - probably Washington time (translator's note).

K (cm^{-2}) caused by these moderated spectra in 10- Ω cm-Si-n/p solar cells was determined. As a base we used the known energy dependence of the damage constant k for this type of cell. (Damage constant k of Si-solar cells; see bibliography⁶). Finally, the total damage $K(=K_p+K_e)$ was related to the damage constant k of the 1-MeV-electrons generally used for test purposes and we obtained the so-called equivalent fluence of the test radiation. Table and chart 2 show the result. From this it appears that the damage due to protons of the Van Allen belt is from 1 to 2 times as large as the damage done by electrons. For the nuclear charge number of the shielding material $Z = 13(\text{Al})$ was taken, which approximates quite closely a material like SiO_2 ⁵). The larger shielding thicknesses are, of course, unreal for solar cells. However, since the program also serves to calculate the ionization and volume damage, it is preferable to include these thicknesses rather than change the program.

12.2 Radiation Charge through the Solar Flares

During the gas eruptions of the sun which occur several times a year mostly protons are emitted. The computation of the charge caused by the solar cosmic protons is based on the estimates of the annual stream density of solar protons near the earth's orbit (in 1 AE) obtained from empirical connections with the number of sun spots during the 20th sun spot cycle (1965-1975). If one takes as basis for the propagation of solar cosmic protons in interplanetary space a quadratic distance law (e.g. stream density $\sim r^{-2}$), then one computes with an already described computer program⁷) for the solar probe (perihelion 0.3 AE, aphelion 1.0167 AE, period 195.19 d) a radiation charge 2.74 times higher than in 1 AE. In the case of a distance law with stream density $\sim r^{-1.5}$ this factor equals 2.00; with a stream density of $\sim r^{-2.5}$ this factor equals 3.95. The calculation is based on the assumption

that the solar cosmic protons are emitted by the sun at a constant average stream density over the entire year and not - as is actually the case - only during statistically occurring brief gas eruptions. The calculation, therefore, furnishes a better estimate the longer the heliocentric mission lasts. A period of a year, corresponding to about two times around the sun, naturally does not fulfill this requirement satisfactorily. However, as long as there are no more reliable forecasts for the appearance of solar eruptions a more exact estimate of the probable radiation charge is not possible.

The calculations were based on the stream density of solar cosmic protons for the year 1972, the last year for which we have a forecast. According to Webber⁸⁾ we may expect in 1972: average number of sun spots 38, number of solar eruptions 6 per year, integrated stream density ϕ_0 of solar cosmic protons in 1 AE:

$$\begin{array}{lll} \phi_0 (>1 \text{ MeV}) \approx 6 \cdot 10^9 & \frac{p}{\text{cm}^2 \text{ a}} \\ \phi_0 (>10 \text{ MeV}) \approx 1.5 \cdot 10^8 & " \\ \phi_0 (>40 \text{ MeV}) \approx 1.5 \cdot 10^7 & " \end{array}$$

The proton spectrum striking the solar probe during a year may be obtained - in accordance with the above assumption - by multiplying by factor 2.74. This spectrum was also entered on chart 1 (I). The solar cell damage caused by spectrum ϕ_0 and the yearly equivalent particle streams of a 1-MeV-electron test radiation required for simulation were already computed in relation to the thickness of the shielding⁷⁾. Through multiplication of these values by factor 2.74 one obtains the values given in table and chart 2.

As chart 2 shows, the radiation charge in the Van Allen belt makes, during the ascent phase, a worthwhile contribution only when thin covering glass layers are used in front of the solar cell. The absolute values of the total radiation charge of the solar probe after a year are relatively small. For

instance, the yearly equivalent 1-MeV-electron fluence for simulation of the total radiation charge of the solar cell behind a 50 μm thick covering glass layer amounts to about $5 \cdot 10^{13} \text{ e/cm}^2$.) This radiation dose corresponds to a degradation of the maximum output of the solar cell of 7 to 8% (without taking into account a possible healing). Of this equivalent dose 77% are due to the heliocentric trajectory, the remaining 23% are caused by the protons of the Van Allen belt. The charge due to electrons from the Van Allen belt is negligible. With covering glass layers above 100 μm in thickness the contribution made by the Van Allen belt radiation is less than 10%, since the spectrum of the Van Allen protons is considerably "softer" than that of the solar cosmic protons (chart 1).

Bibliography

- 1) Letter from the firm Boelkow P 42 - 1828/68 Kt/pe of Sept. 30, 68
and P 42 - 1864/68 Mu/Si of Oct. 3, 68
- 2) C. E. McIlwain, Coordinates for Mapping the Distribution of
Magnetically Trapped Particles, J. Geophys. Res. 66, 3681 (1961).
- 3) K. Wohlleben, Computation of the Radiation Charge of Satellites,
Chapter II, Integration of the Particle Stream Densities on a
Satellite Trajectory in the Van Allen Radiation Belt. GfW - Report
RV 1-624/36 (19)/67.*
- 4) J. I. Vette, Models of the Trapped Radiation Environment,
A. B. Lucero, NASA SP-3024 Vol I to IV.
J. A. Wright,
J. H. King
- 5) K. Wohlleben, Computation of the Radiation Charge in the Van Allen
Belt, discussed on the Basis of the Example of the Research Satellite
AZUR. BMwF-FB W 68-18 (1968). **
- 6) R. Baeuerlein, Radiation Damage in Semi-Conductors and Semi-Conductor
Construction Elements. Solid Bodies VIII.
- 7) K. Wohlleben, Computation of the Radiation Charge of Satellite,
Chapter I, Radiation Charge of Earth Satellites and Solar Probes
through solar cosmic radiation (solar flares). GfW - Report RV
1-624/36(19)/67.*
- 8) W. R. Webber, Sunspot Number and Solar Cosmic Ray Predictions for
Cycle 20 (1965-1975) with Preliminary Estimates for Cycle 21.
Boeing Comp. D2-113522-1 (1967).

Translator's notes:

* GfW probably stands for Gesellschaft fuer Wissenschaft (Scientific Society)

** BMwF - Bundesministerium fuer wissenschaftliche Forschung (Federal
Ministry for Scientific Research)

Equivalent stream of a 1-MeV-electron test radiation for the simulation of the damage produced in 10- Ω cm-Si-n/p solar cells during one year (1972) in the trajectory of the solar probe (perihelion 0.3 AE, aphelion 1.0167 AE) in relation to the thickness of the shielding (nuclear charge = 13)

Thickness of the shielding (Z = 13)

1-MeV-electron equivalent for simulation of the charge through	0,01	0,02	0,05	0,1	0,2	0,5	1,0	2,0	5,0	10	$\frac{g}{cm^2}$
solar flares during the year 1972*)	4,2'13	2,2'13	8,6'12	4,0'12	1,9'12	6,6'11	3,0'11	1,3'11	4,5'10	1,9'10	$\frac{1-MeV-e}{cm^2}$
protons in the Van Allen belt during ascent trajectory B	1,2'13	2,2'12	5,4'11	2,5'11	7,2'10	1,1'10	6,7'9	1,1'9	5,7'7	6,5'6	$\frac{1-MeV-e}{cm^2}$
electrons in the Van Allen belt during ascent trajectory B	3,3'10	3,1'10	2,7'10	1,9'10	1,2'10	3,3'9	6,3'8	1,9'7	2,2'4	1,7'1	$\frac{1-MeV-e}{cm^2}$
total charge during the year 1972	5,4'13	2,4'13	9,7'12	4,3'12	1,9'12	6,7'11	3,1'11	1,3'11	4,5'10	1,9'10	$\frac{1-MeV-e}{cm^2}$

- *) under assumption
1. of a quadratic distance law for the propagation of solar cosmic protons in interplanetary space (fluence $\sim r^{-2}$);
 2. that the solar cosmic protons are emitted by the sun in a timely constant stream density.

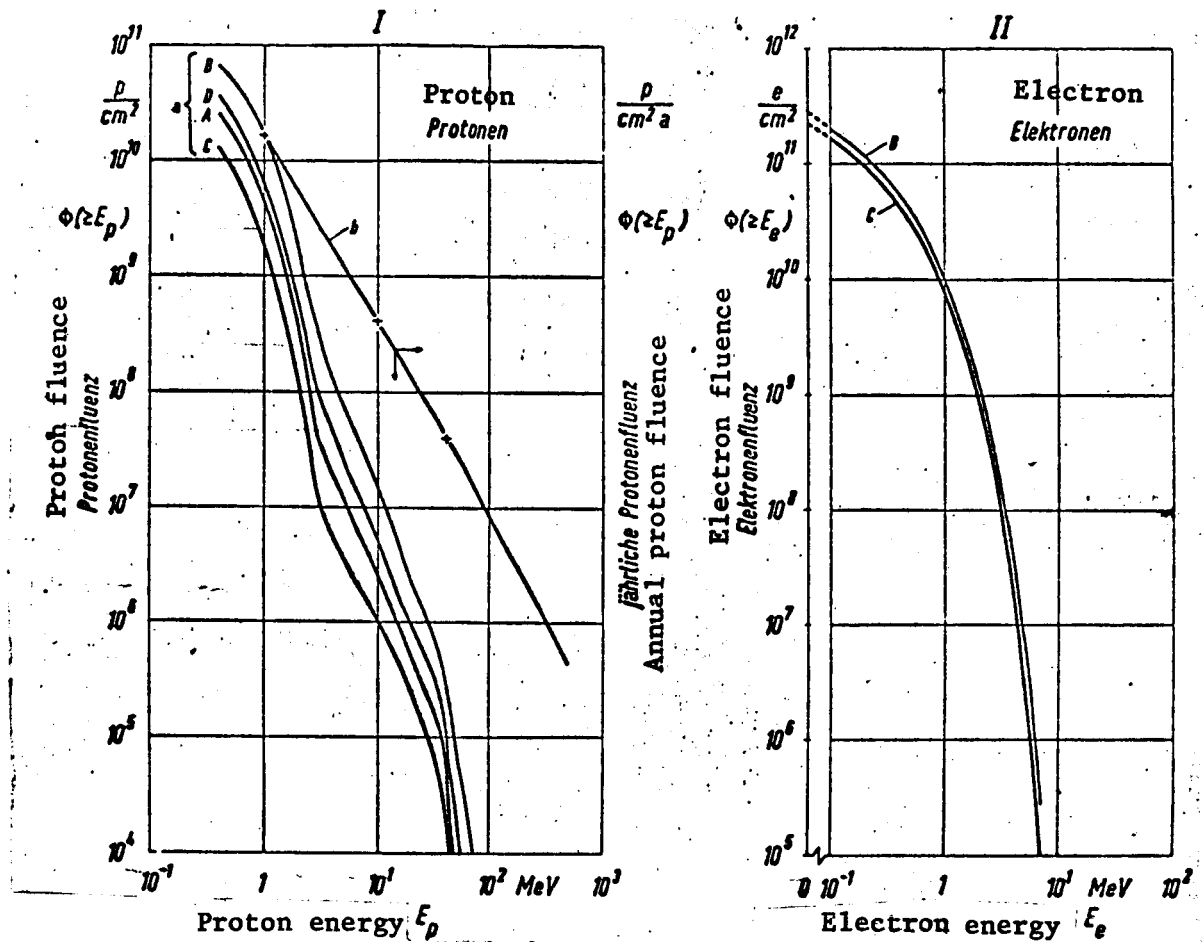


Chart 1 Radiation charge of the solar probe (helios)

- Ia integrated proton spectra for 4 different ascent trajectories (A,B,C,D) through the Van Allen belt;
- Ib integrated spectrum of the solar cosmic protons (solar flares) along the heliocentric trajectory (perihelion 0.3 AE, aphelion 1.0167 AE);
- II integrated electron spectra for ascent trajectory B (maximum fluence) and C (minimum fluence) through the Van Allen belt.

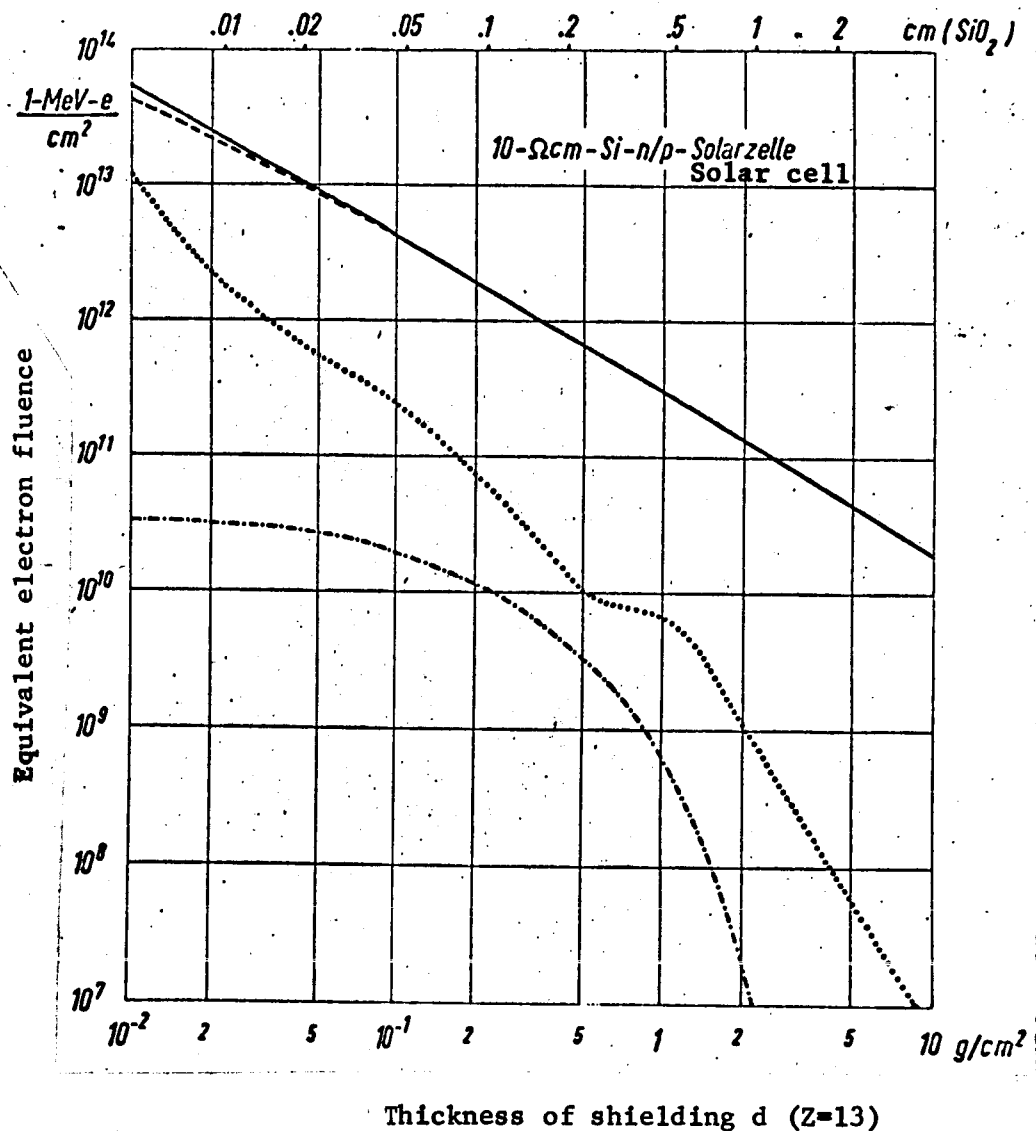


Chart 2 Equivalent stream of a 1-MeV-electron test radiation for the simulation of the damage produced in 10-Ωcm-Si-n/p solar cells during one year in the trajectory of the solar probe (perihelion 0.3 AE, aphelion 1.0167 AE) in relation to the thickness of the shielding (nuclear charge = 13).

- total charge;
- - - - - charge through solar flares during the year 1972;
- charge through protons in the Van Allen belt in ascent trajectory B;
- . - . - charge through electrons in the Van Allen belt in ascent trajectory B.

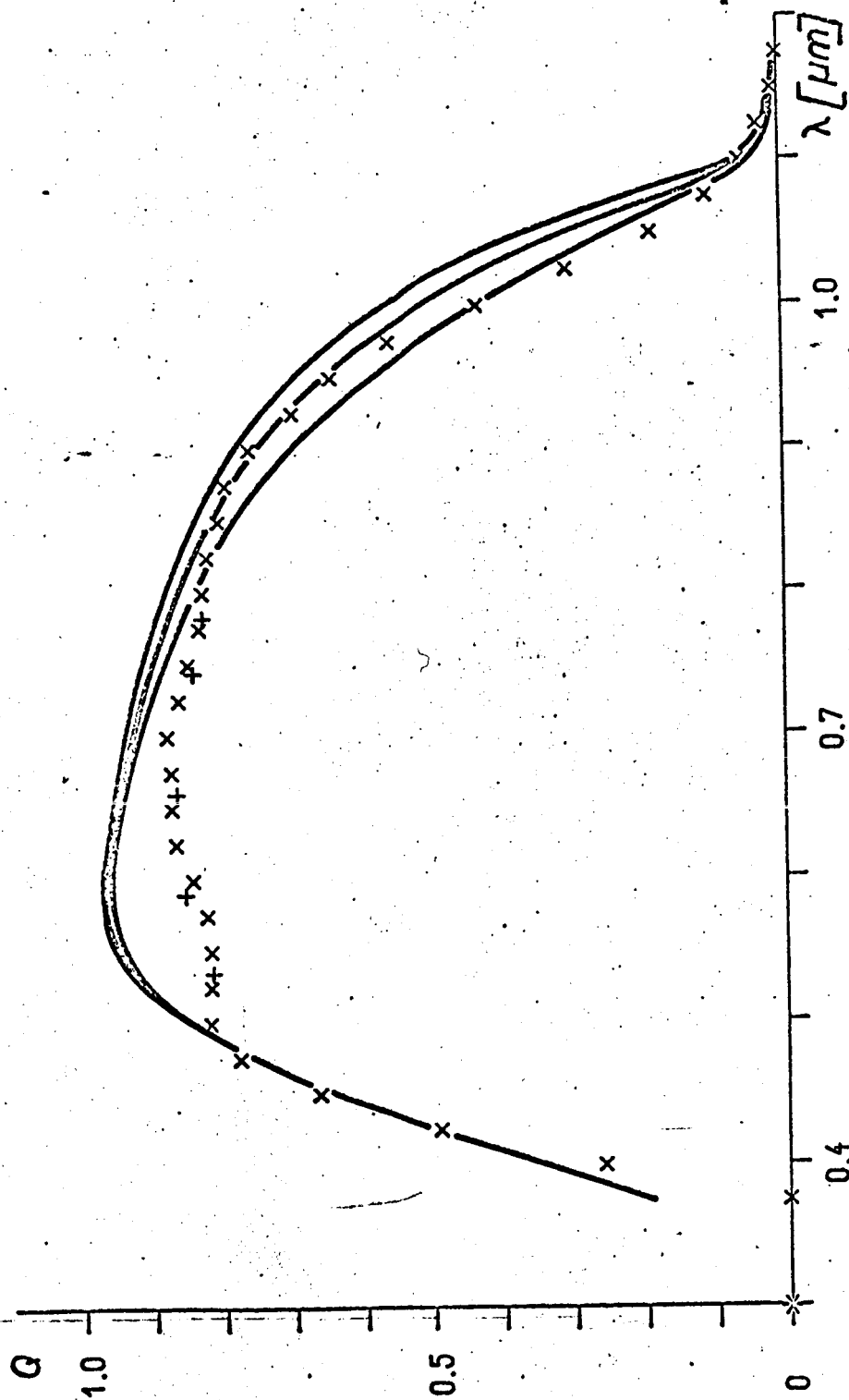


Figure 1 Theoretical quanta yield of a silicon n/p solar cell in relation to the wave length of the incident light. Parameters: diffusion length of the minority charge carriers of the basic material. From top to bottom $L_n = 200, 150$ and $100 \mu\text{m}$. For comparison the measured quanta yield of a type V solar cell.

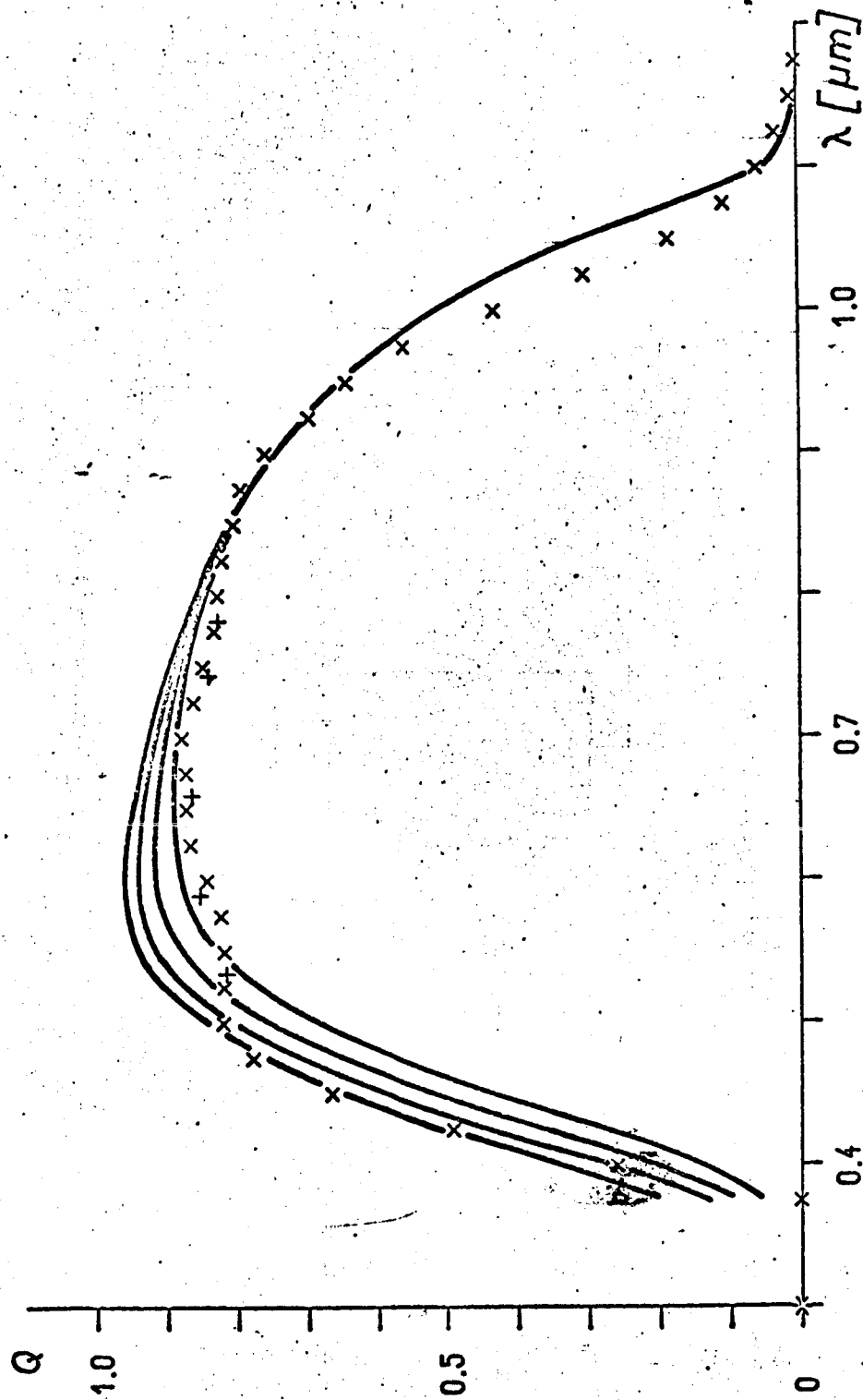


Figure 2 Theoretical quanta yield of a silicon n/p solar cell in relation to the wave length of the incident light. Parameters: thickness of the n-layer, from top to bottom 0.1; 0.2; 0.3 and 0.5 μm . For comparison the measured quanta yield of a type V solar cell.

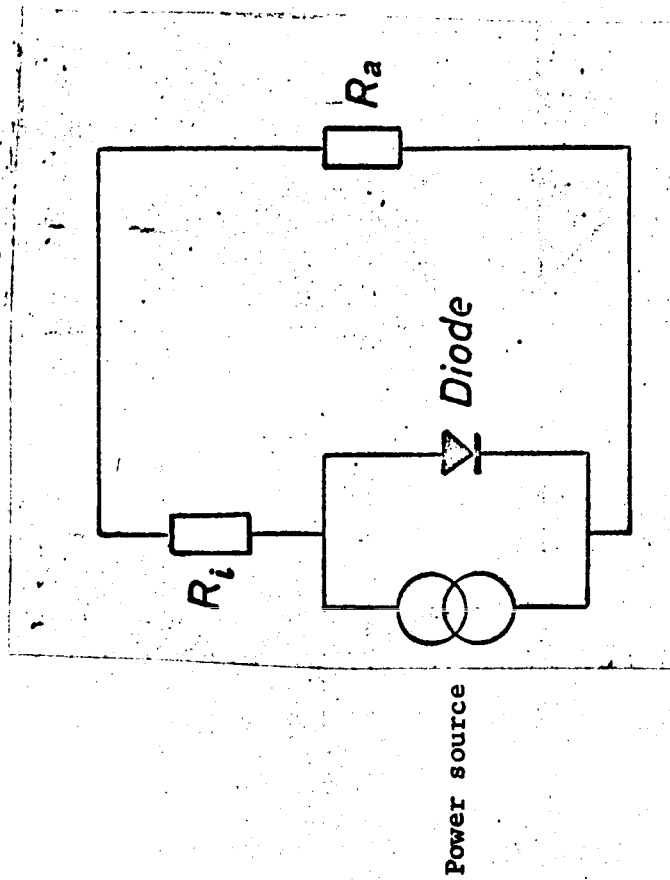


Figure 3 Substitute circuit diagram of a solar cell.
 R_i internal resistance
 R_a work resistance

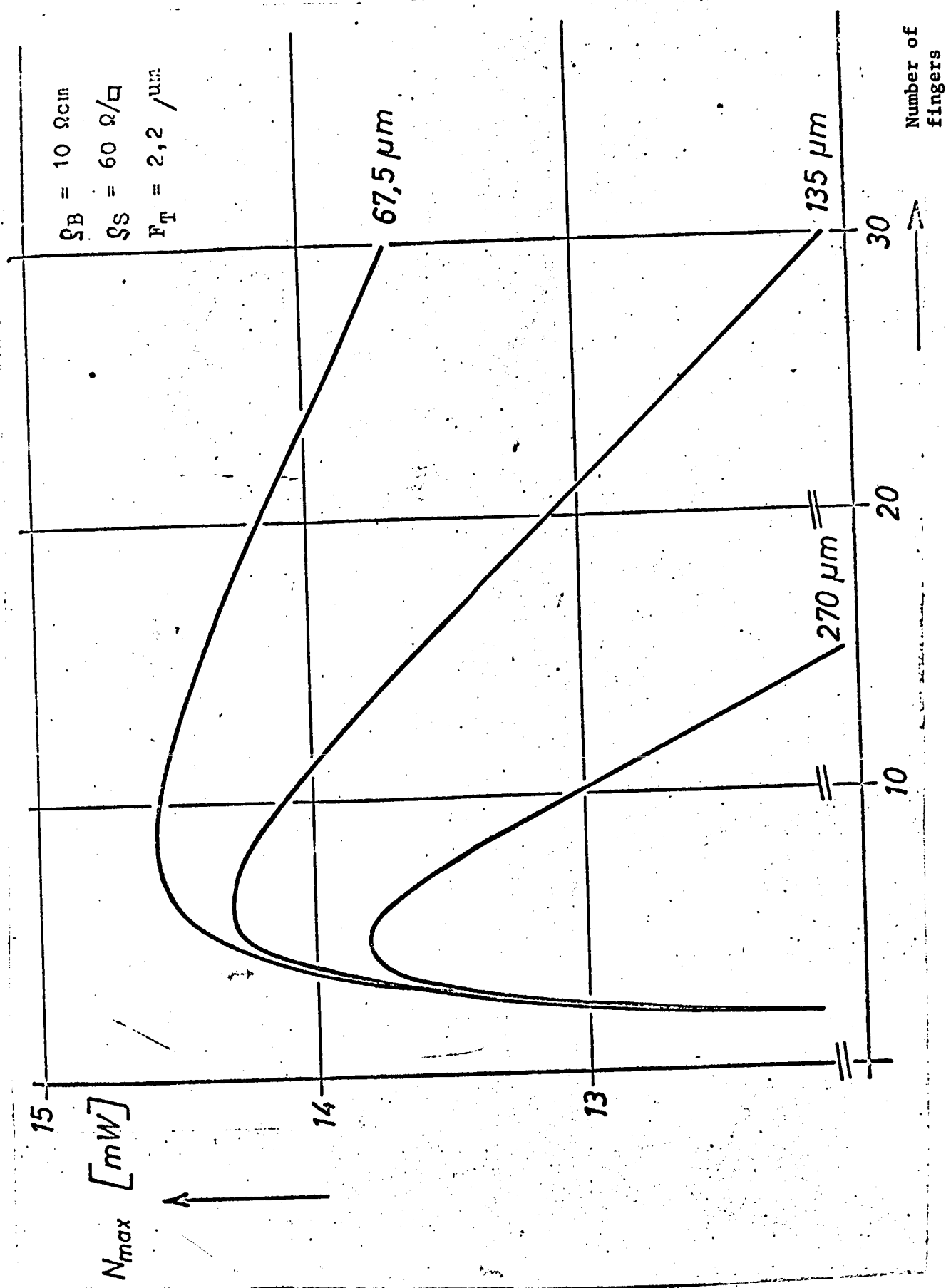


Figure 4 Relation of the output at the optimum working point to the number of grid fingers under an insolation of 0.25 AMO. Parameter: finger width.

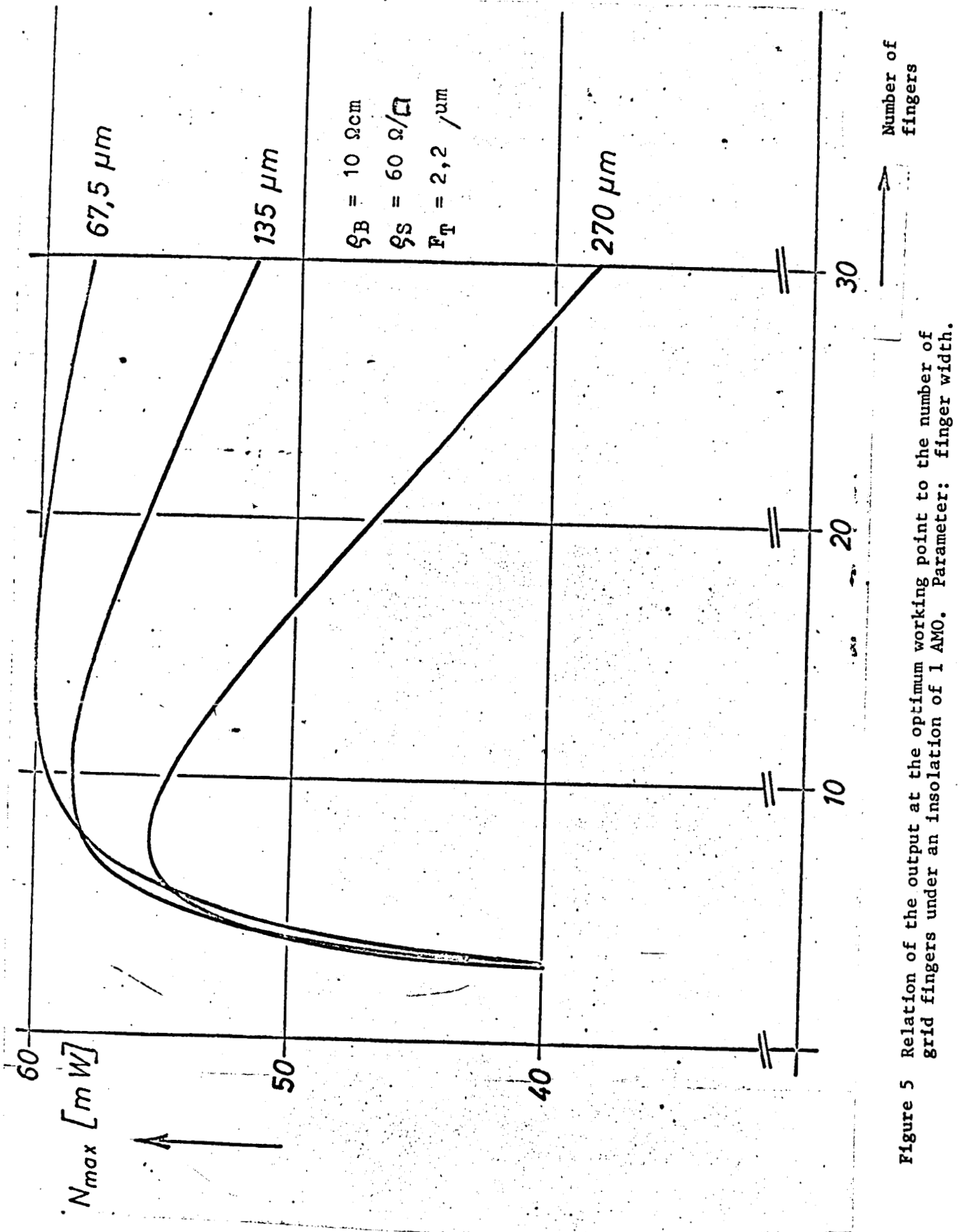


Figure 5 Relation of the output at the optimum working point to the number of grid fingers under an insolation of 1 AMO. Parameter: finger width.

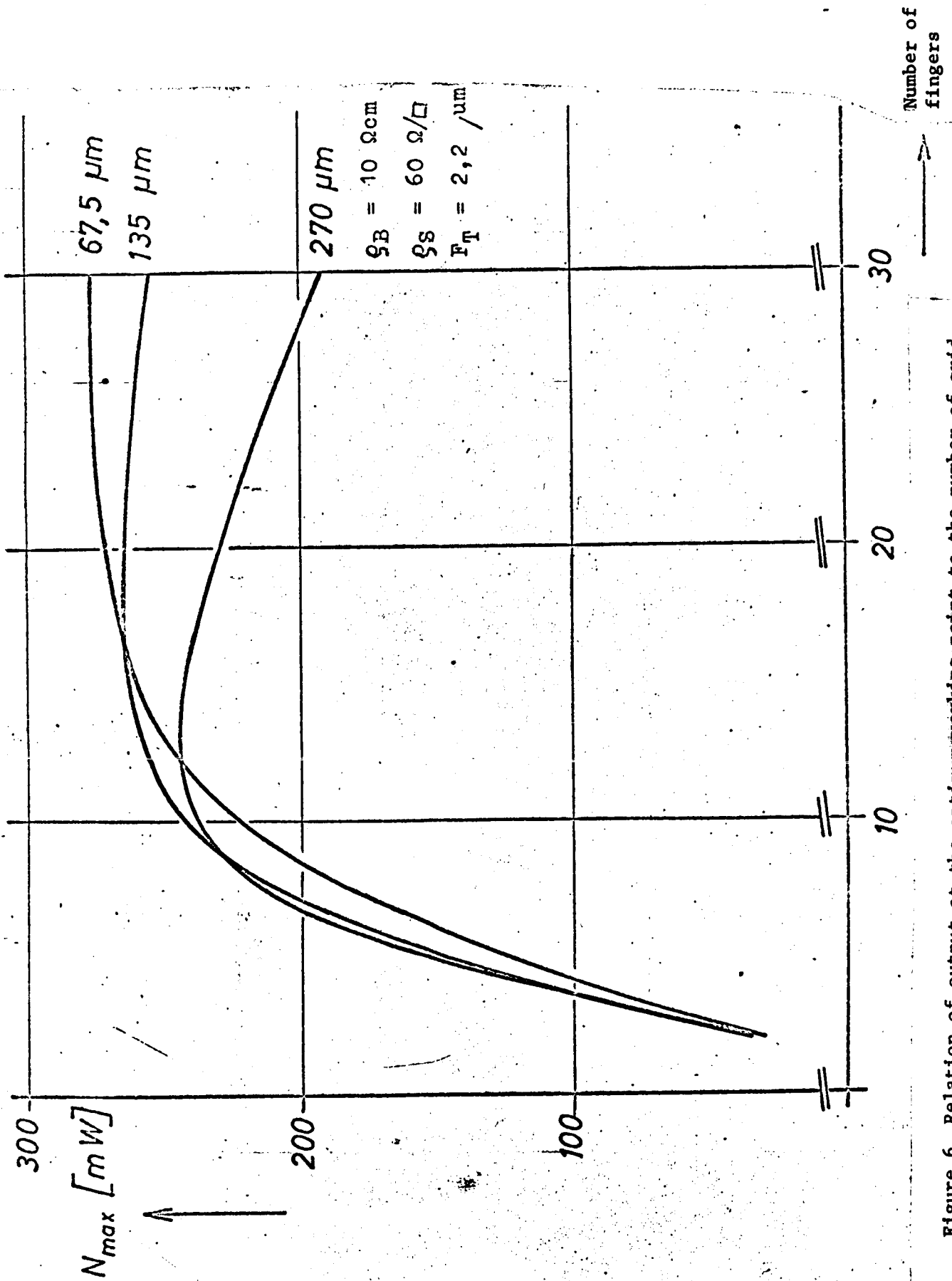


Figure 6 Relation of output at the optimum working point to the number of grid fingers under an insolation of 5 AMO. Parameter: finger width.

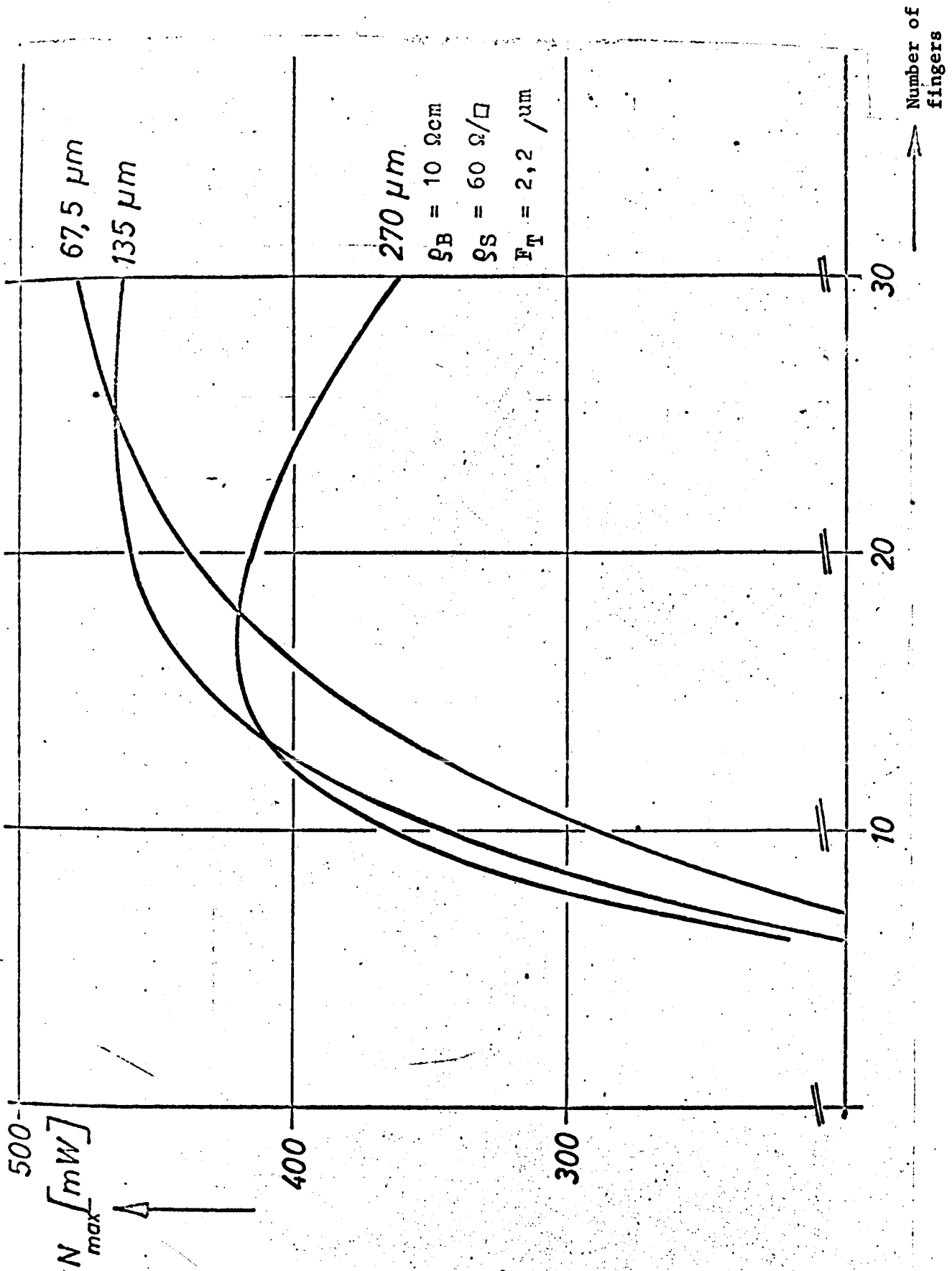


Figure 7 Relation of output at the optimum working point to the number of grid fingers under an insolation of 10 AMO. Parameter: finger width.

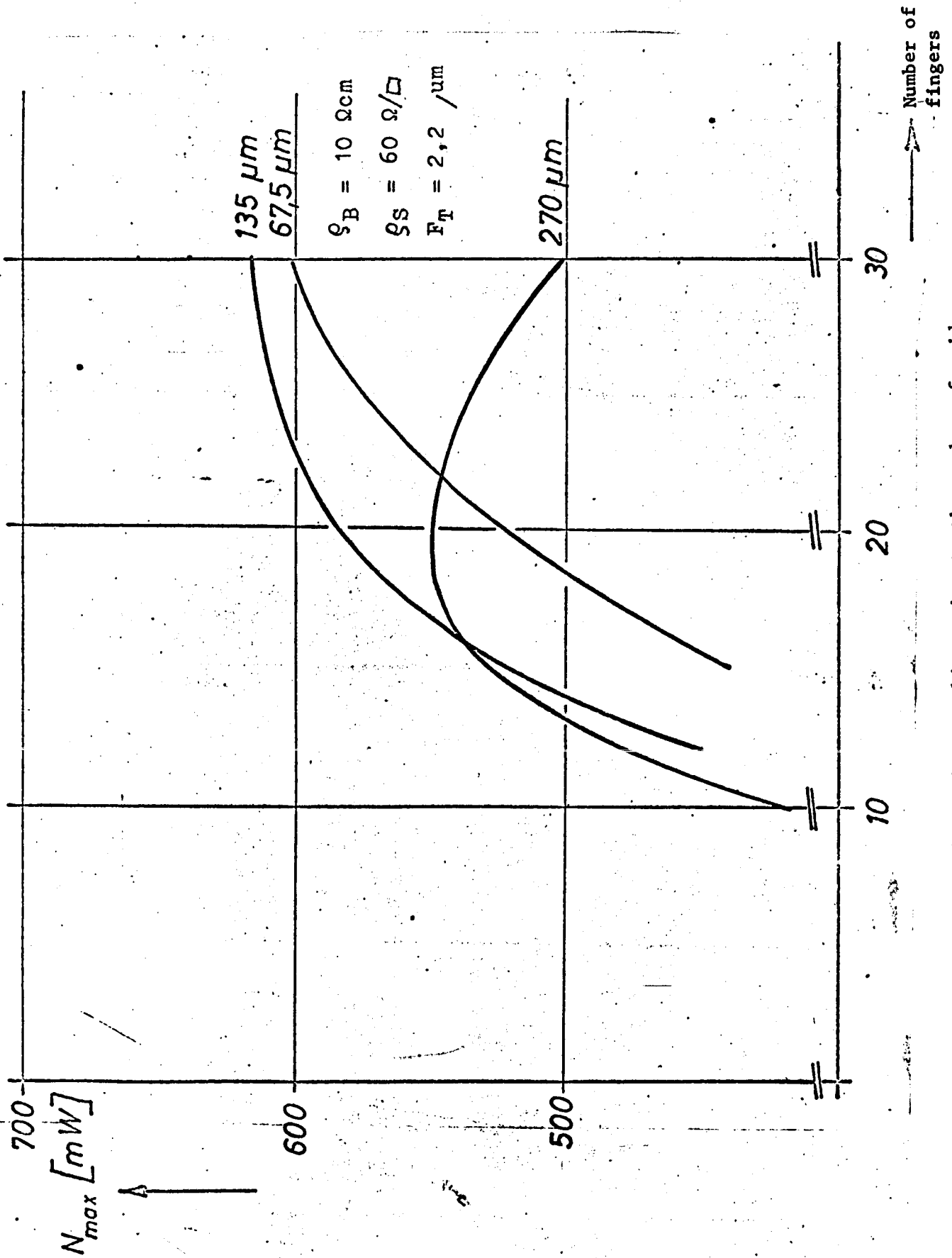


Figure 8 Relation of output at the optimum working point to the number of grid fingers under an insolation of 15 AMO. Parameter: finger width.

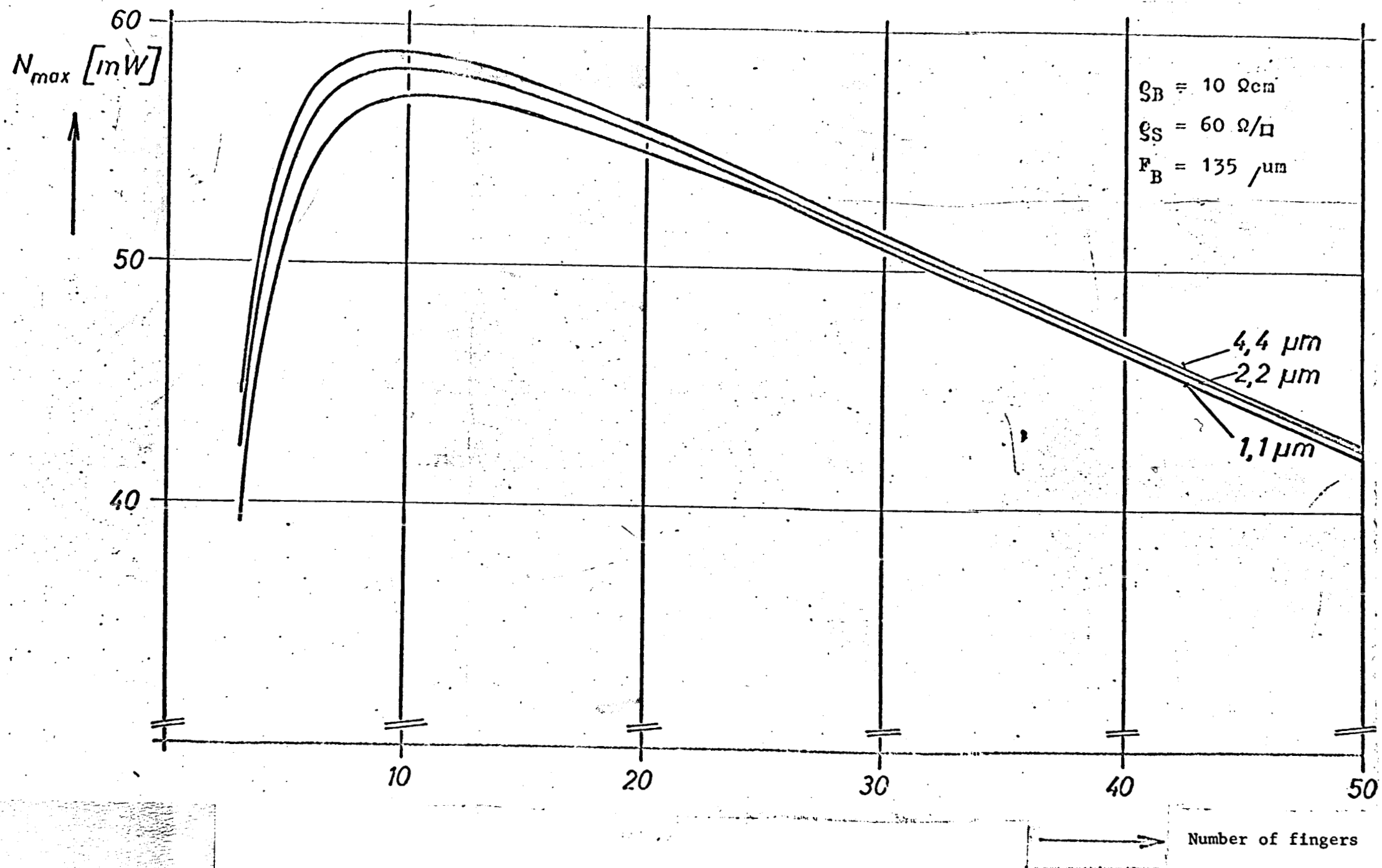


Figure 9 Relation of output at the optimum working point to the number of grid fingers under an insolation of 1 AMO. Parameter: finger depth.

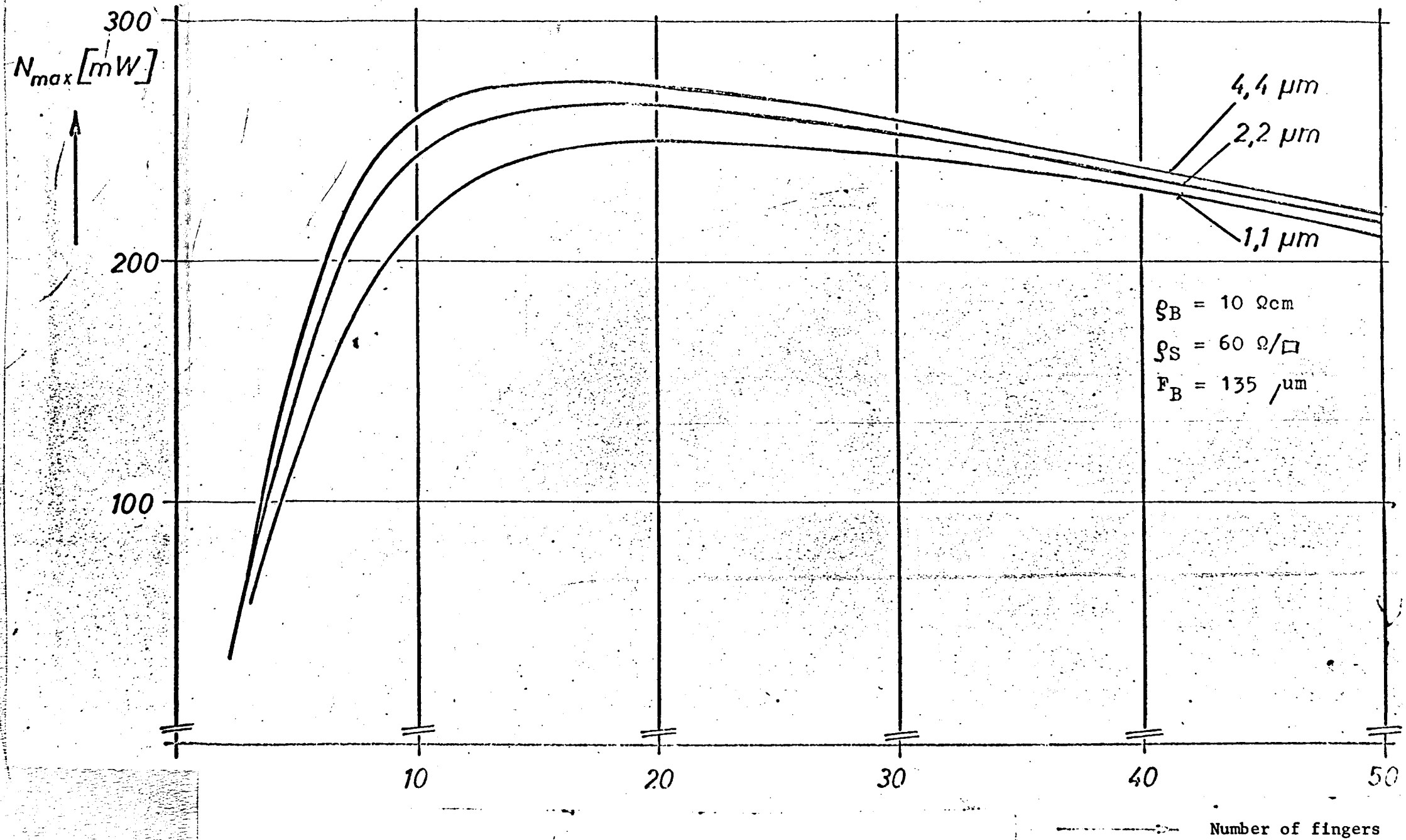


Figure 10 Relation of output at the optimum working point to the number of grid fingers under an insolation of 5 AMO. Parameter: finger depth.

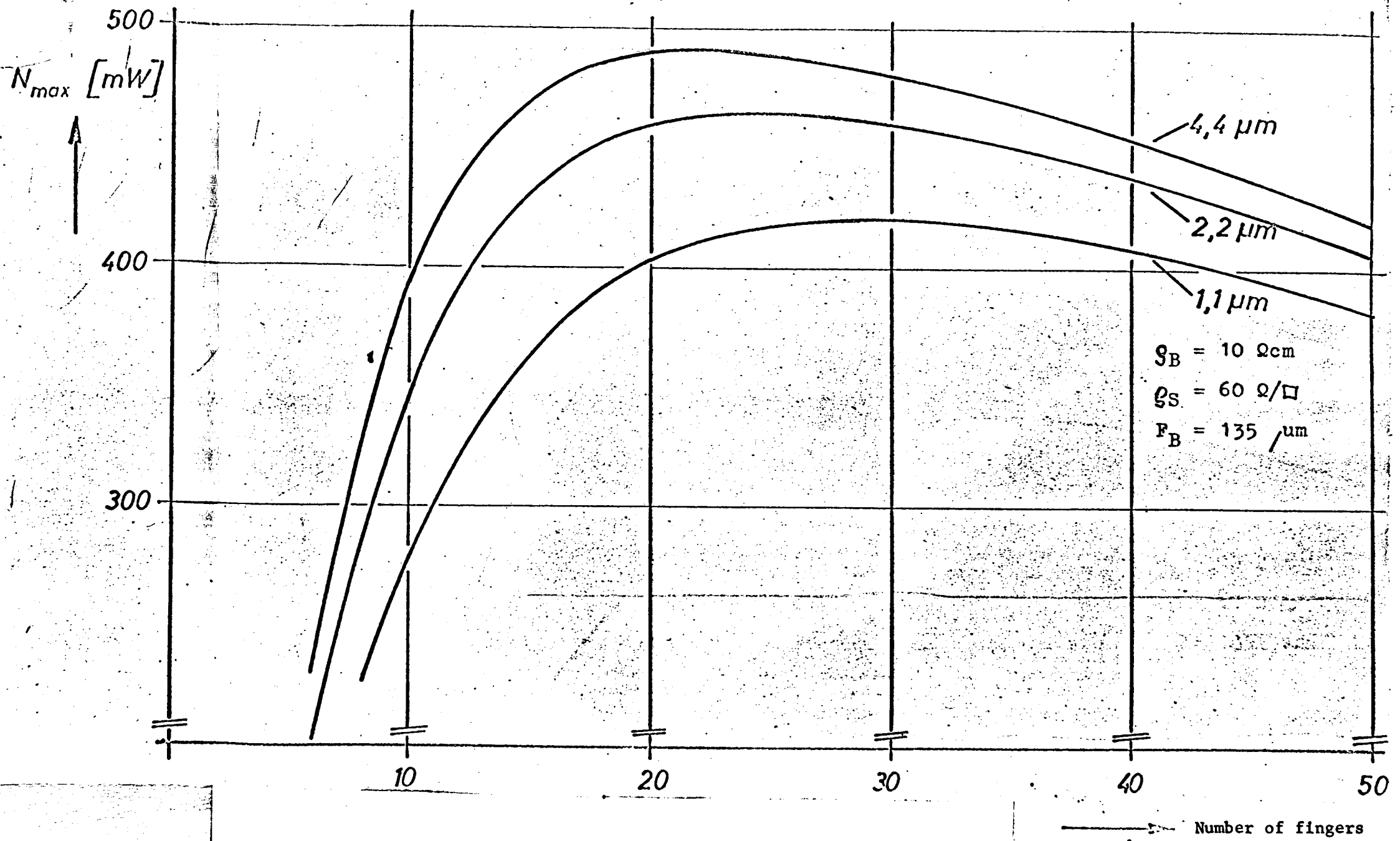


Figure 11. Relation of output at the optimum working point to the number of grid fingers under an insolation of 10 AMO. Parameter: finger depth.

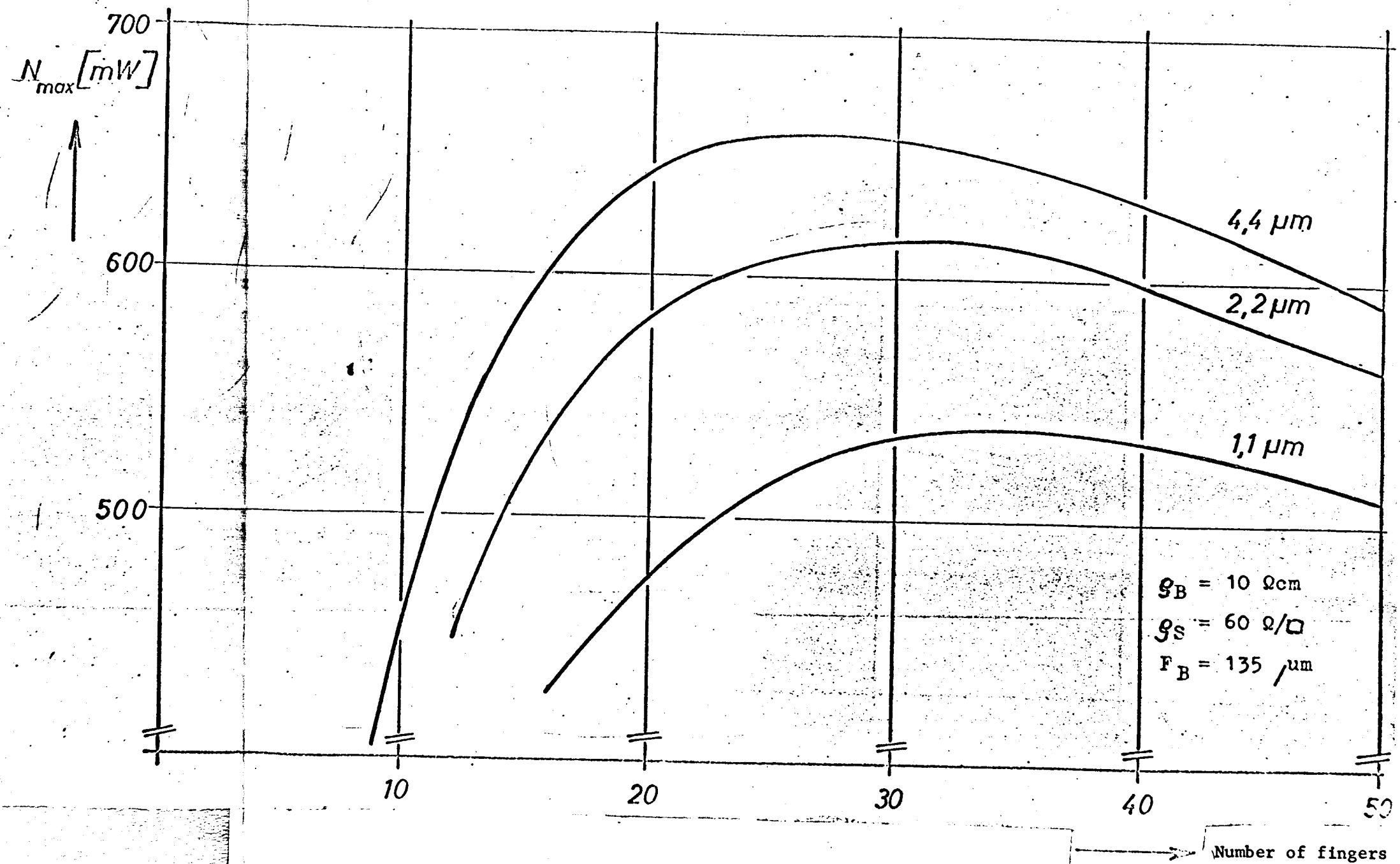
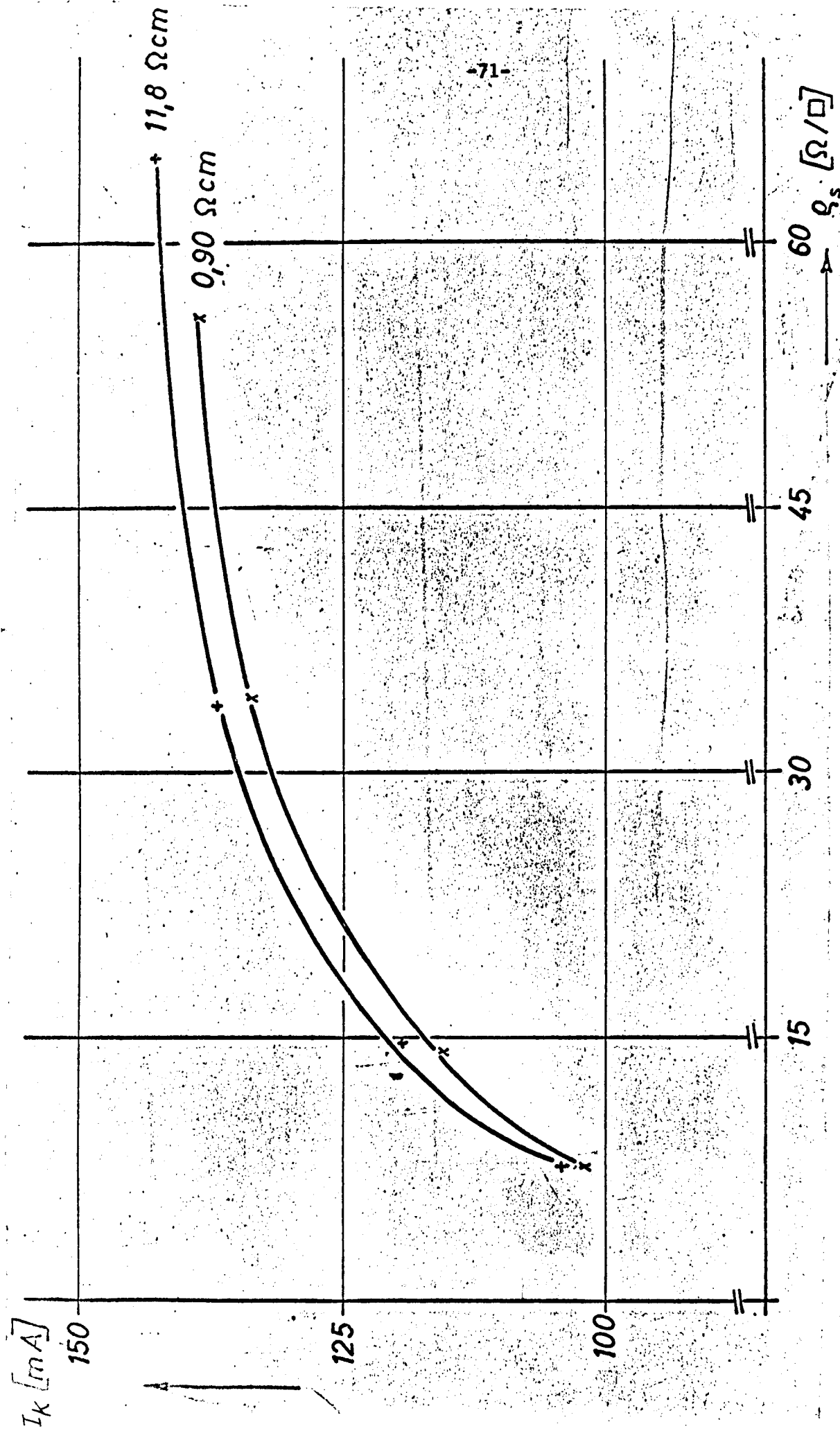


Figure 12 Relation of output at the optimum working point to the number of grid fingers under an insolation of 15 AMO. Parameter: finger depth.



-71-

Figure 13 Experimentally obtained relation of the short circuit current I_K to the layer resistance ρ_B of the n-layer, under AMO. Parameter: specific resistance ρ_B of the p-doped basic material.

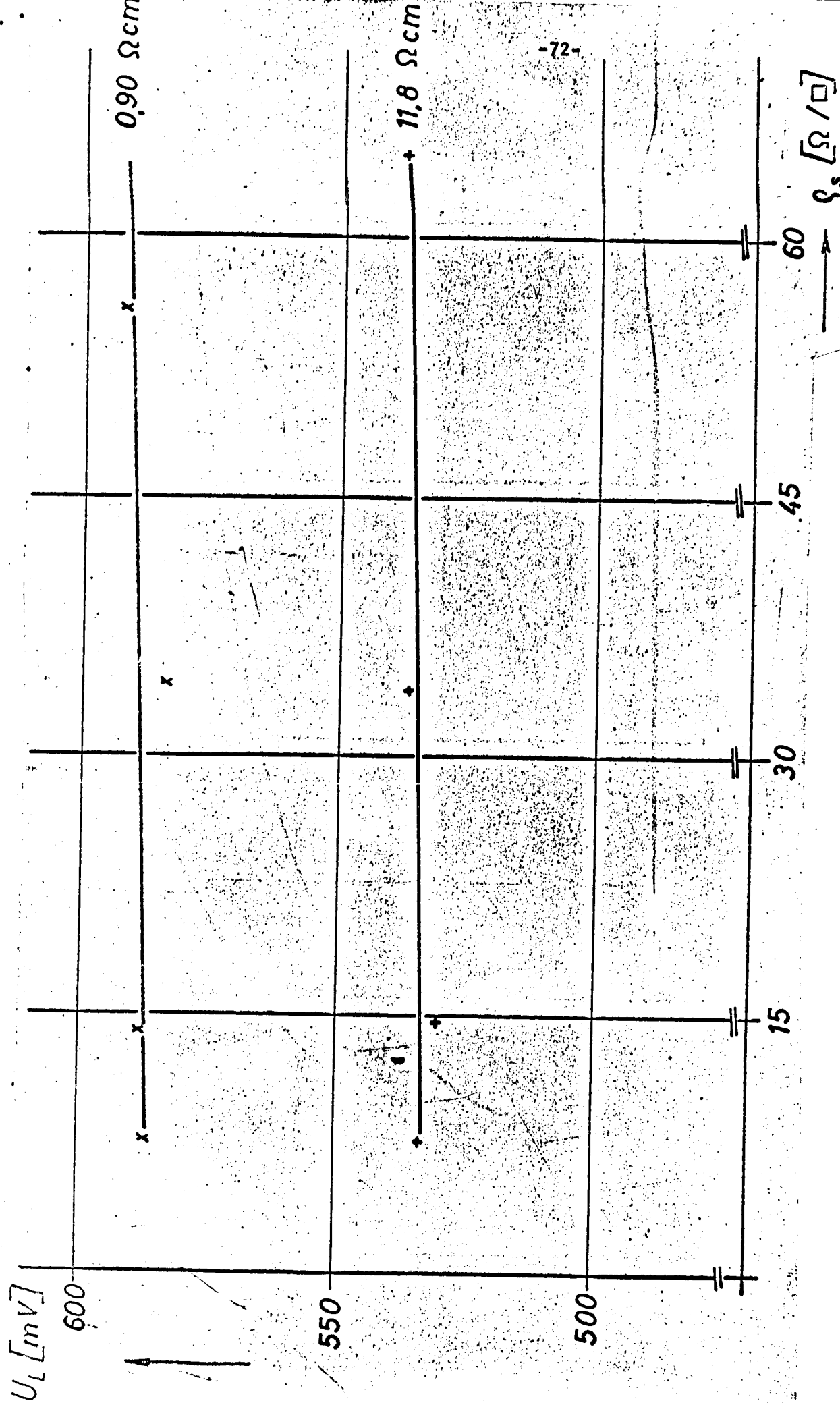


Figure 14 Experimentally obtained relation of the idling potential U to the layer resistance ρ_s of the n-layer, under AMO. Parameter: specific resistance ρ_B of the p-doped basic material.

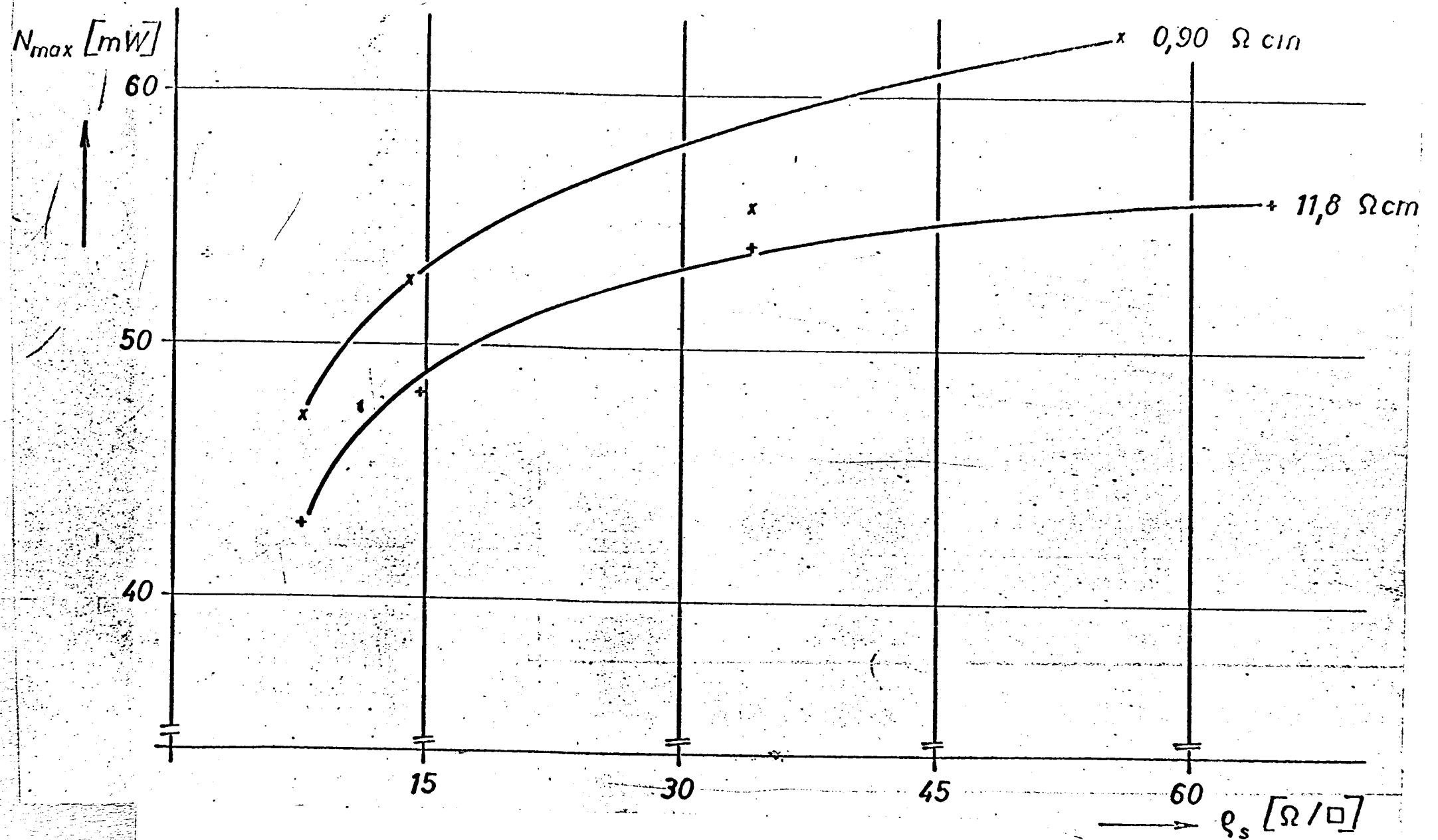


Figure 15 Experimentally obtained relation of the output at the optimum working point N_{max} to the layer resistance ρ_s of the n-layer, under AMO. Parameter: specific resistance ρ_B of the p-doped basic material.

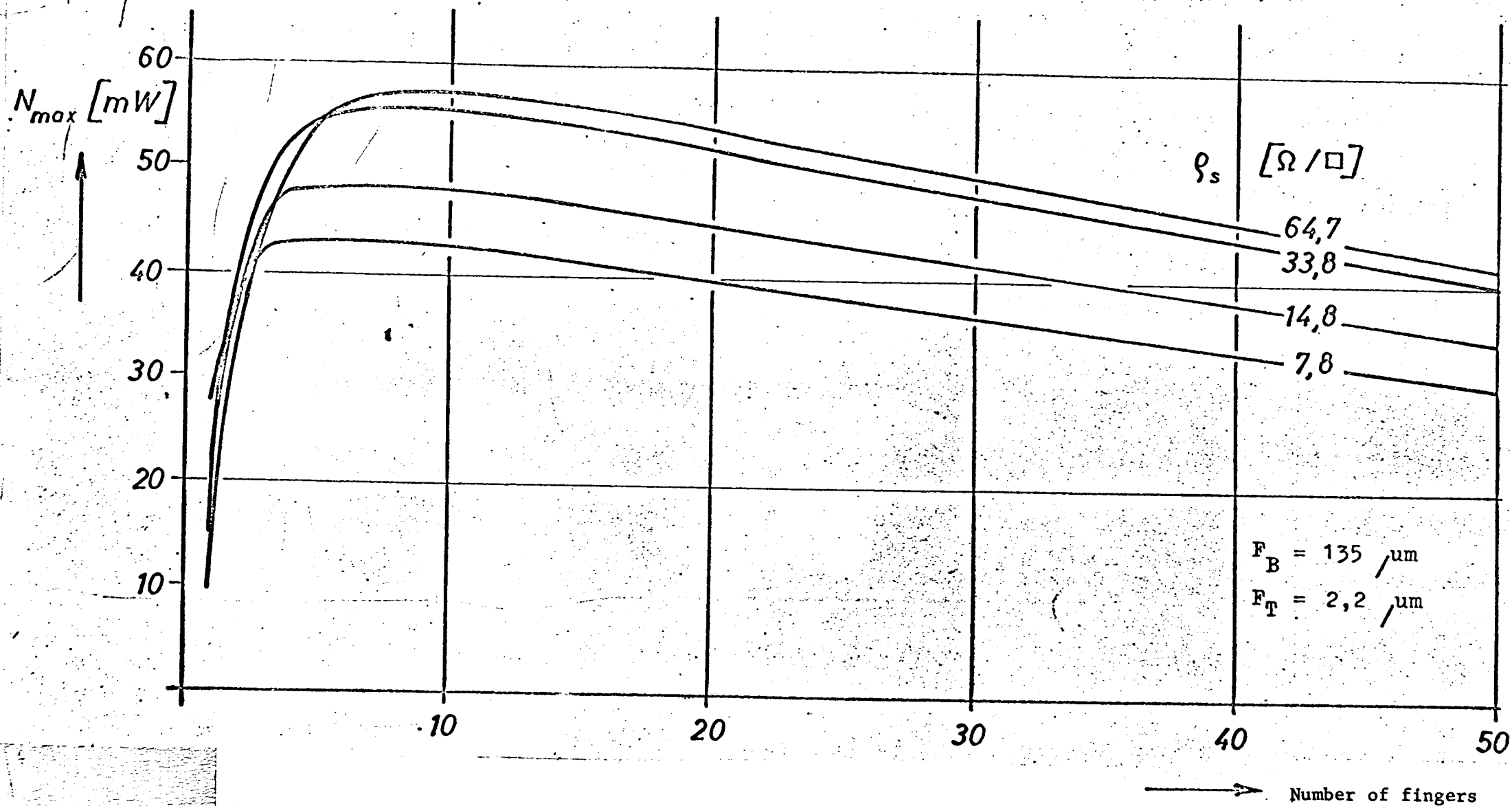


Figure 16 Relation of output at the optimum working point to the number of grid fingers under an insolation of 1 AMO for solar cells made from 10 Ω cm silicon. Parameter: layer resistance ρ_s of the n-layer.

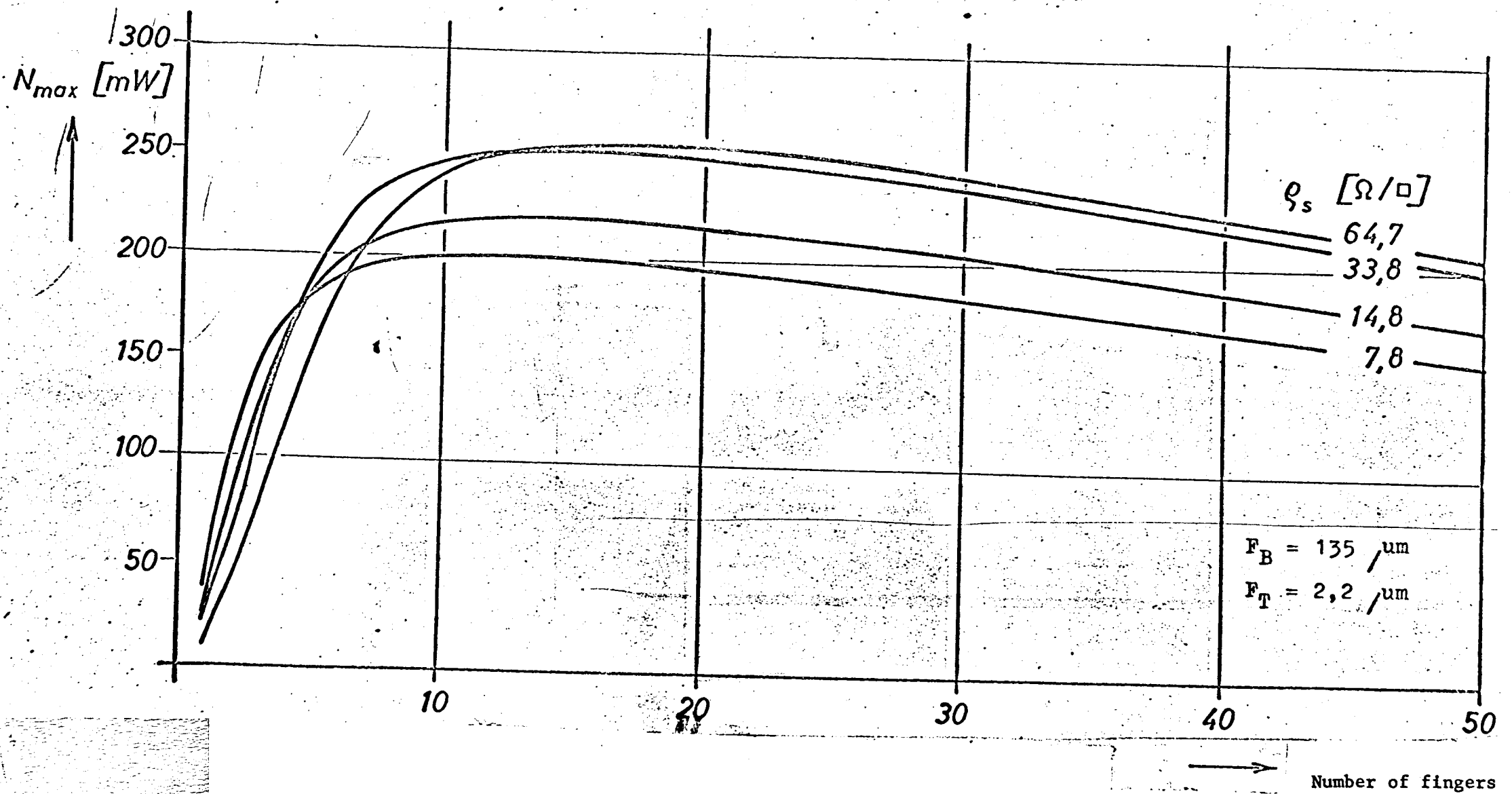


Figure 17 Relation of output at the optimum working point to the number of grid fingers under an insolation of 5 AMO for solar cells made from 10 Ω cm silicon. Parameter: layer resistance ρ_s of the n-layer.

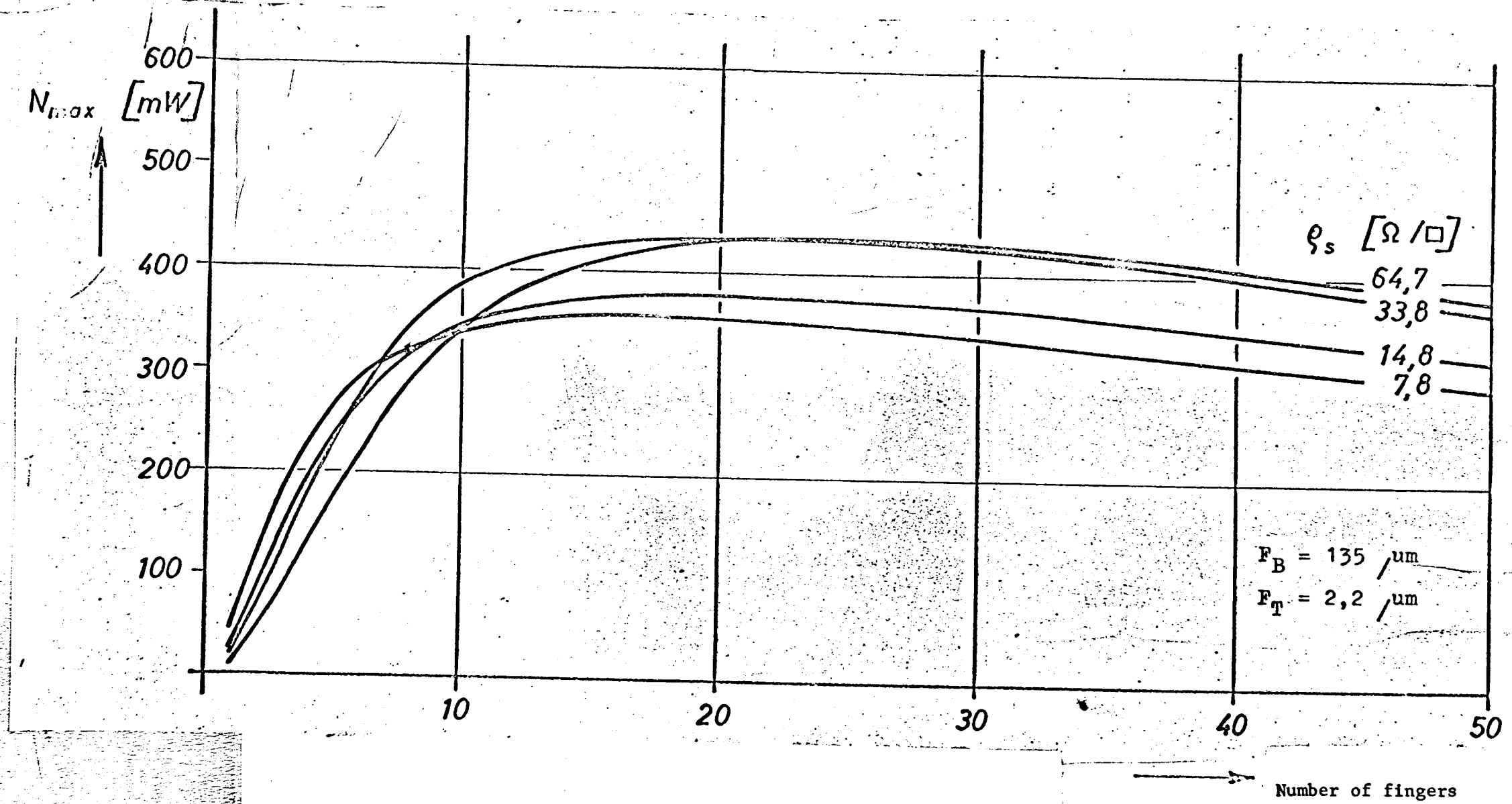


Figure 18 Relation of output at the optimum working point to the number of grid fingers under an insolation of 10 AMO for solar cells made from 10 Ω cm silicon. Parameter: layer resistance ρ_s of the n-layer.

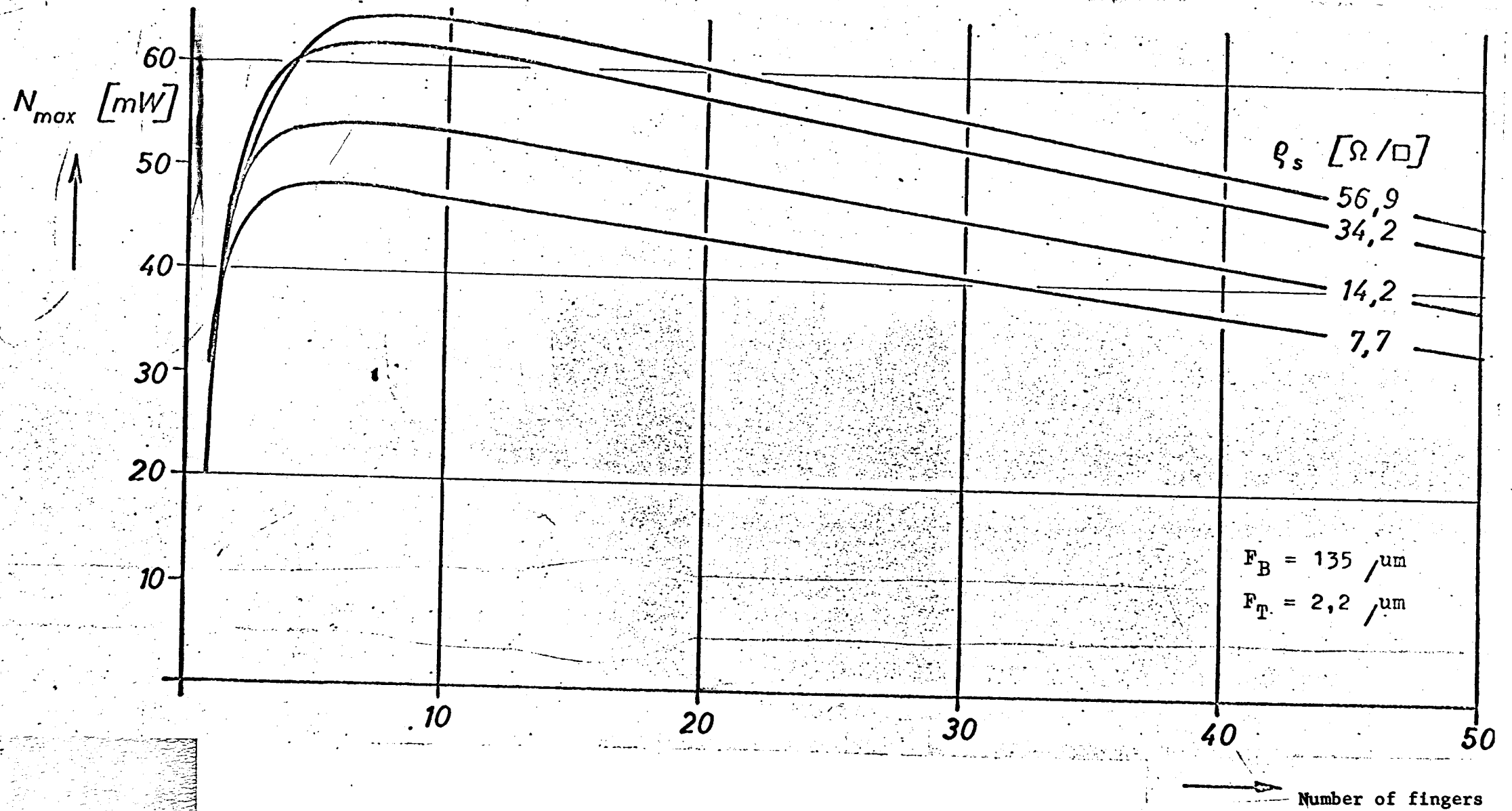


Figure 19 Relation of output at the optimum working point to the number of grid fingers under an insolation of 1 AMO for solar cells made from 1 cm silicon. Parameter: layer resistance ρ_s of the n-layer.

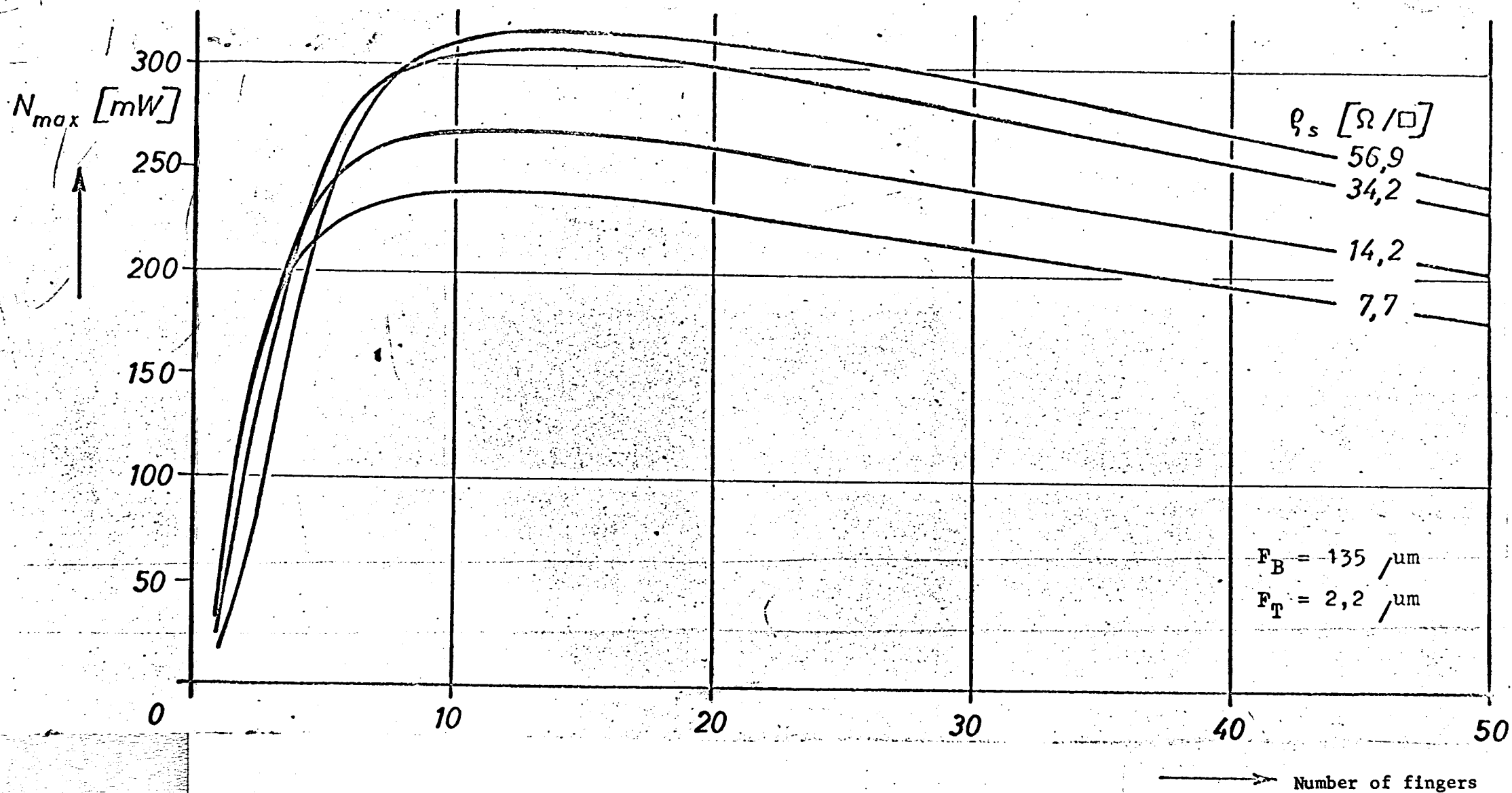


Figure 20 Relation of output at the optimum working point to the number of grid fingers under an insolation of 5 AMO for solar cells made from 1.2 cm silicon. Parameter: layer resistance ρ_s of the n-layer.

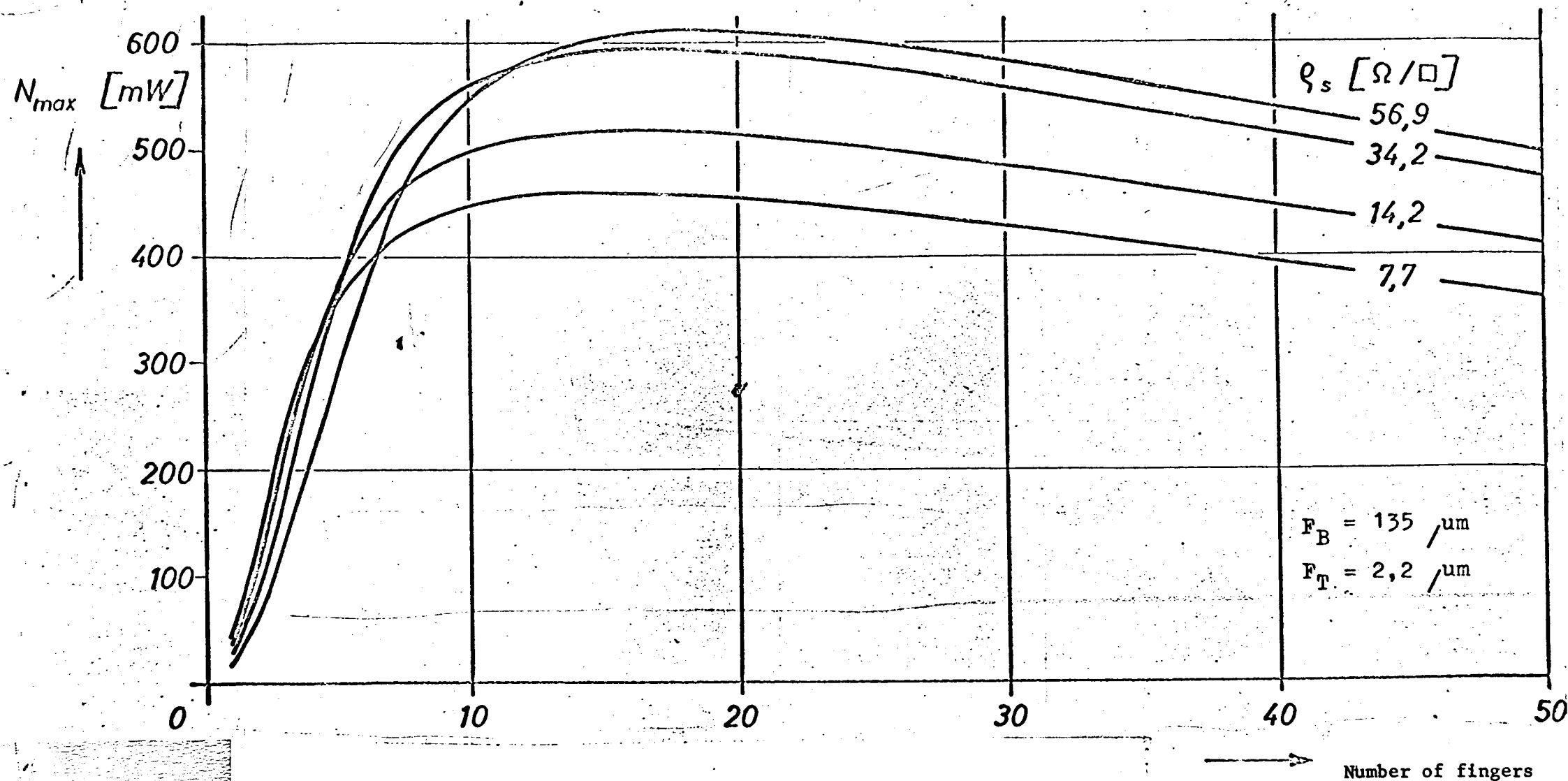


Figure 21 Relation of output at the optimum working point to the number of grid fingers under an insolation of 10 AMO for solar cells made from 1 Ω cm silicon. Parameter: layer resistance ρ_s of the n-layer.

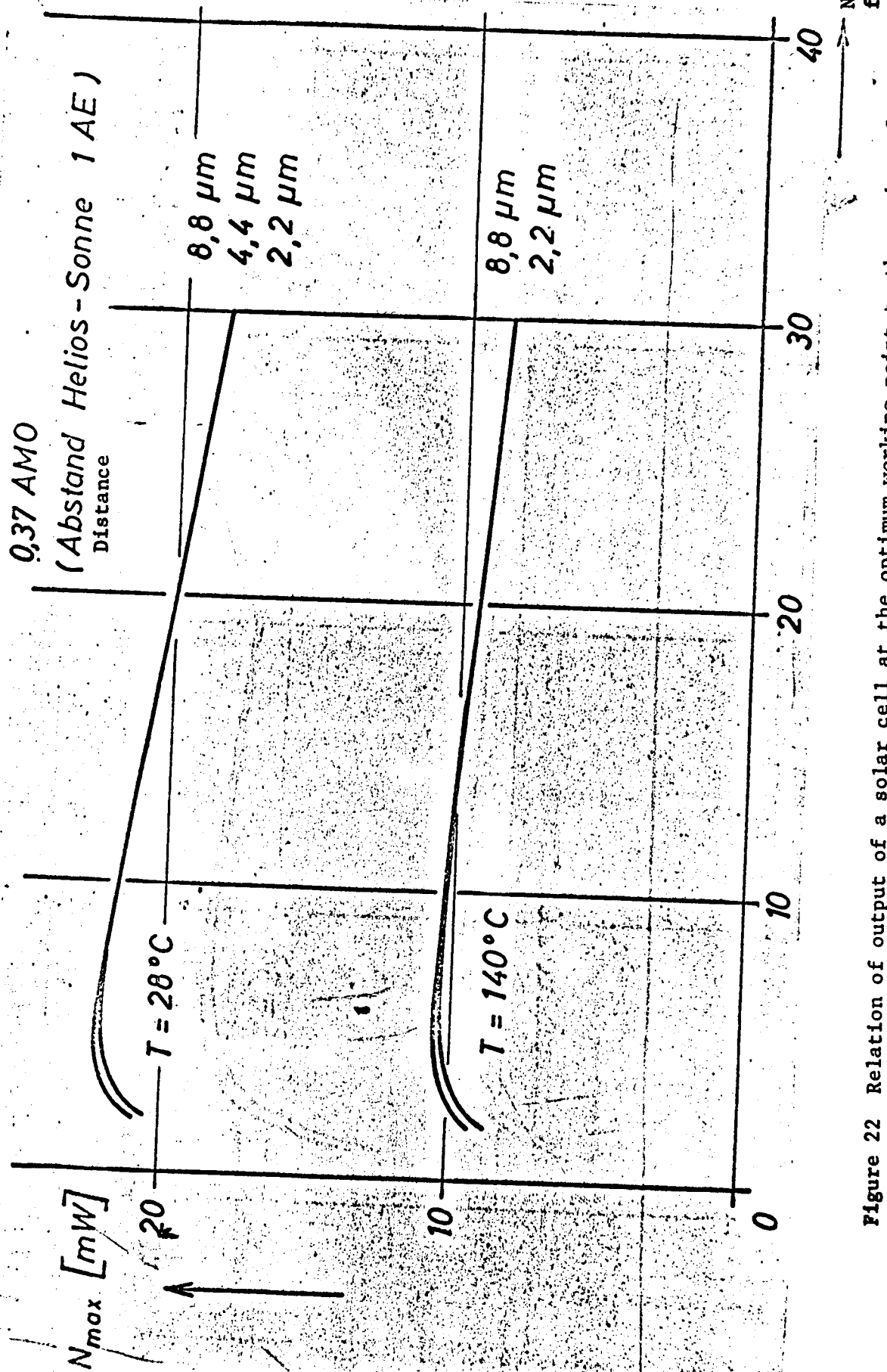


Figure 22 Relation of output of a solar cell at the optimum working point to the number of grid fingers under an insolation averaged for the lighted semi-rotation of a spool. Parameter: temperature and finger depth.

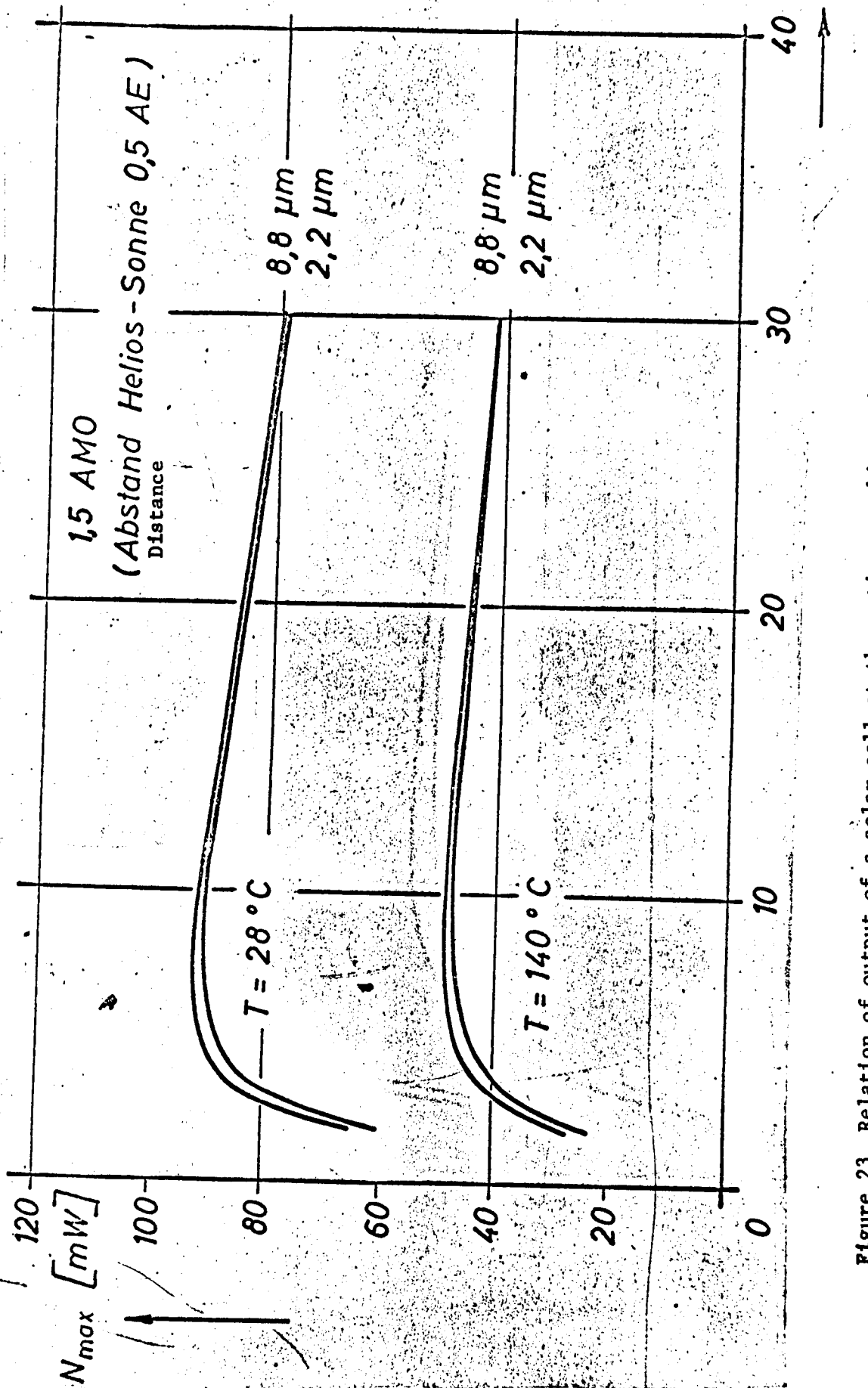


Figure 23 Relation of output of a solar cell at the optimum working point to the number of grid fingers under an insolation averaged for the lighted semi-rotation of a spool. Parameter: temperature and finger depth.

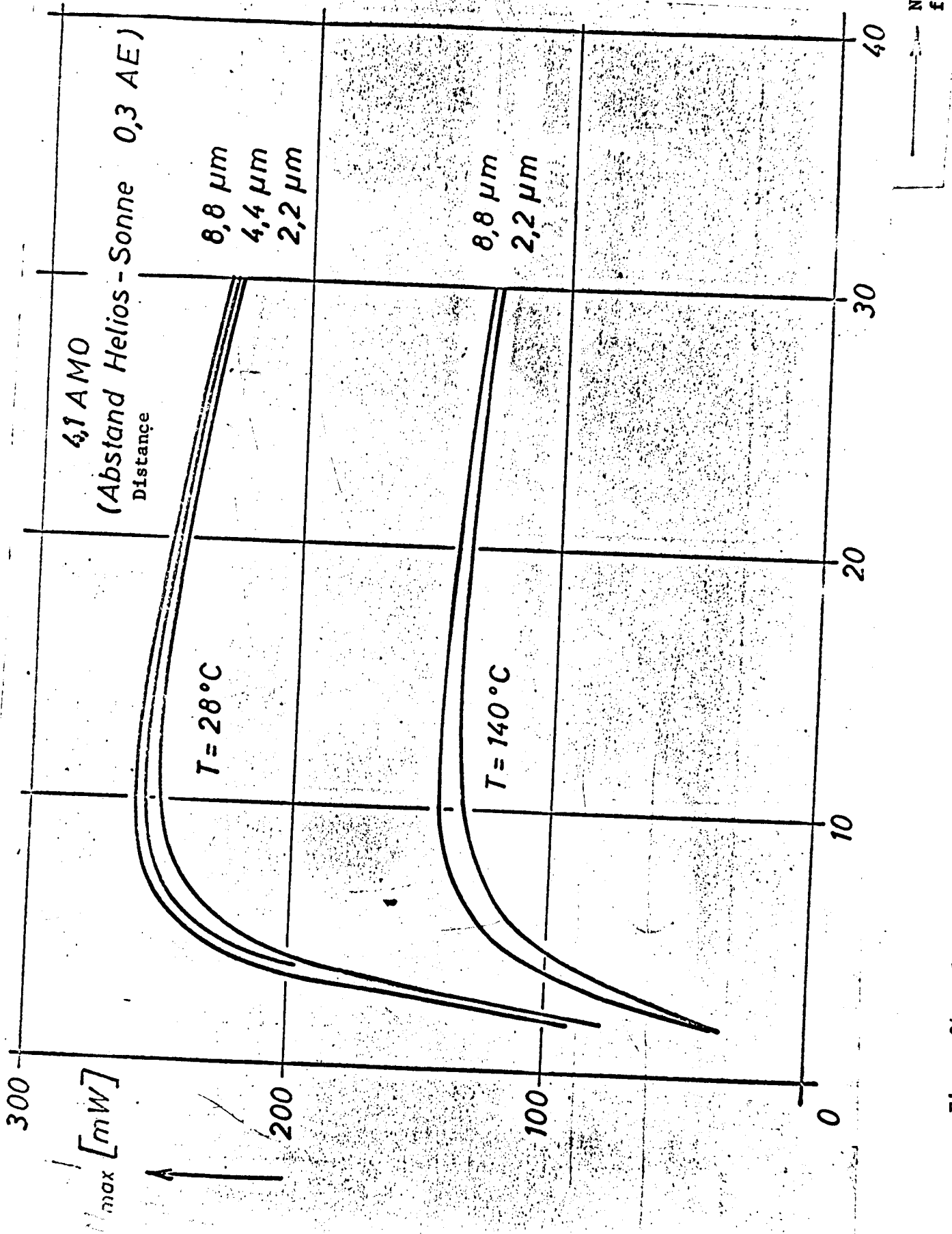


Figure 24 Relation of output of a solar cell at the optimum working point to the number of grid fingers under an insolation averaged for the lighted semi-rotation of a spool.
Parameter: temperature and finger depth.

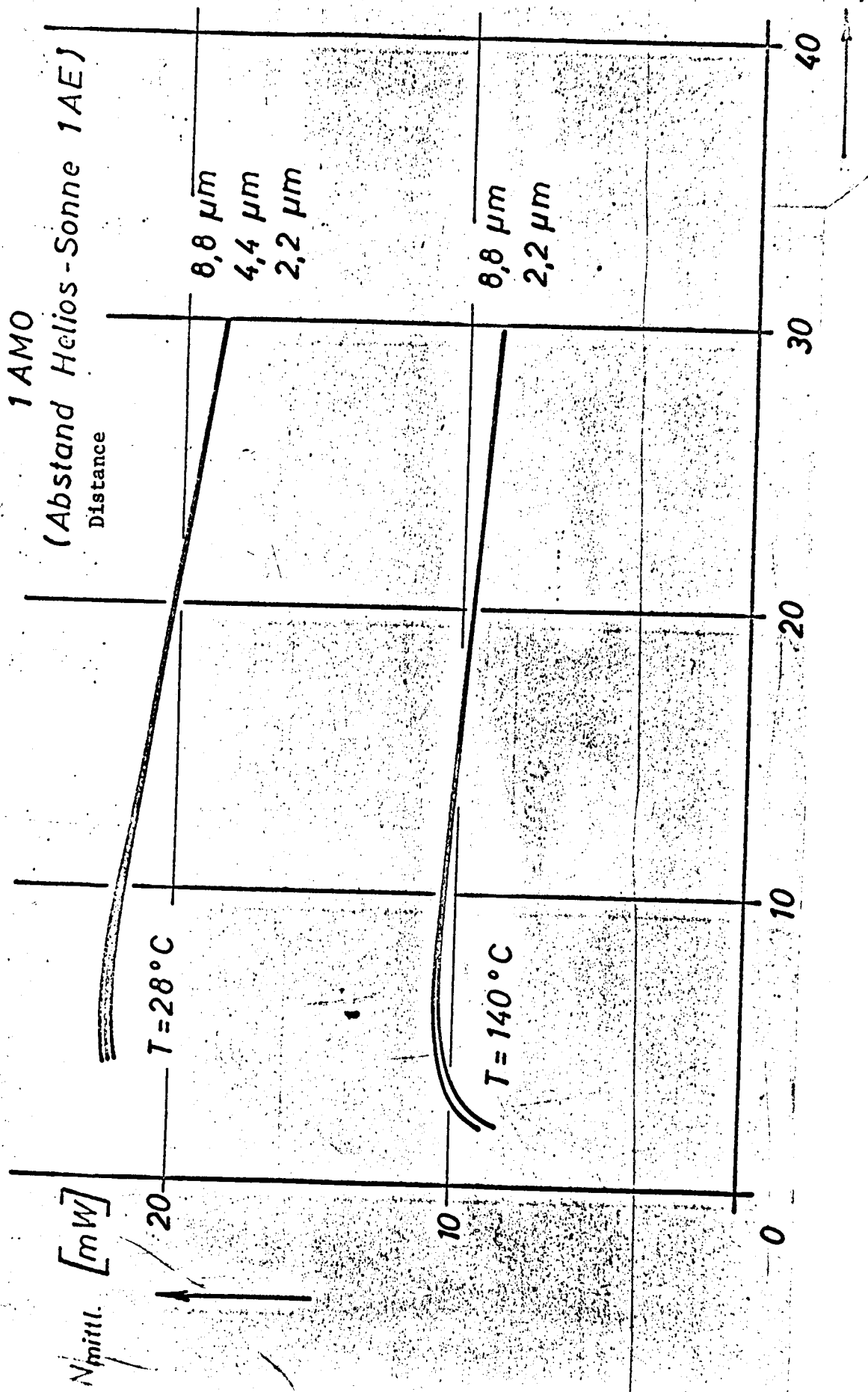


Figure 25 The output of a solar cell at the optimum working point averaged for the lighted semi-rotation of a spool in relation to the number of grid fingers.
Parameter: temperature and finger depth.

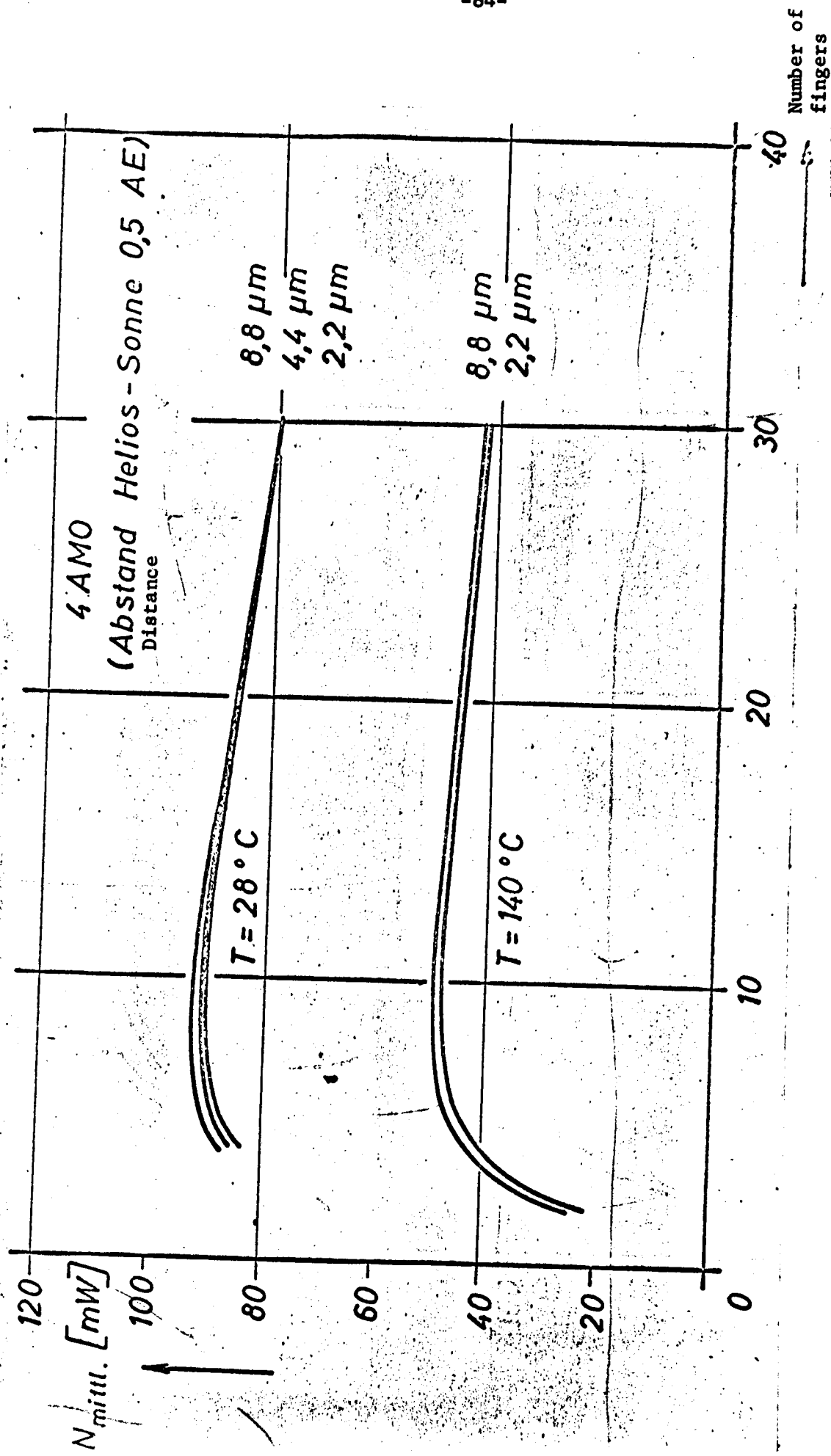


Figure 26 The output of a solar cell at the optimum working point averaged for the lighted semi-rotation of a spool in relation to the number of grid fingers.
Parameter: temperature and finger depth.

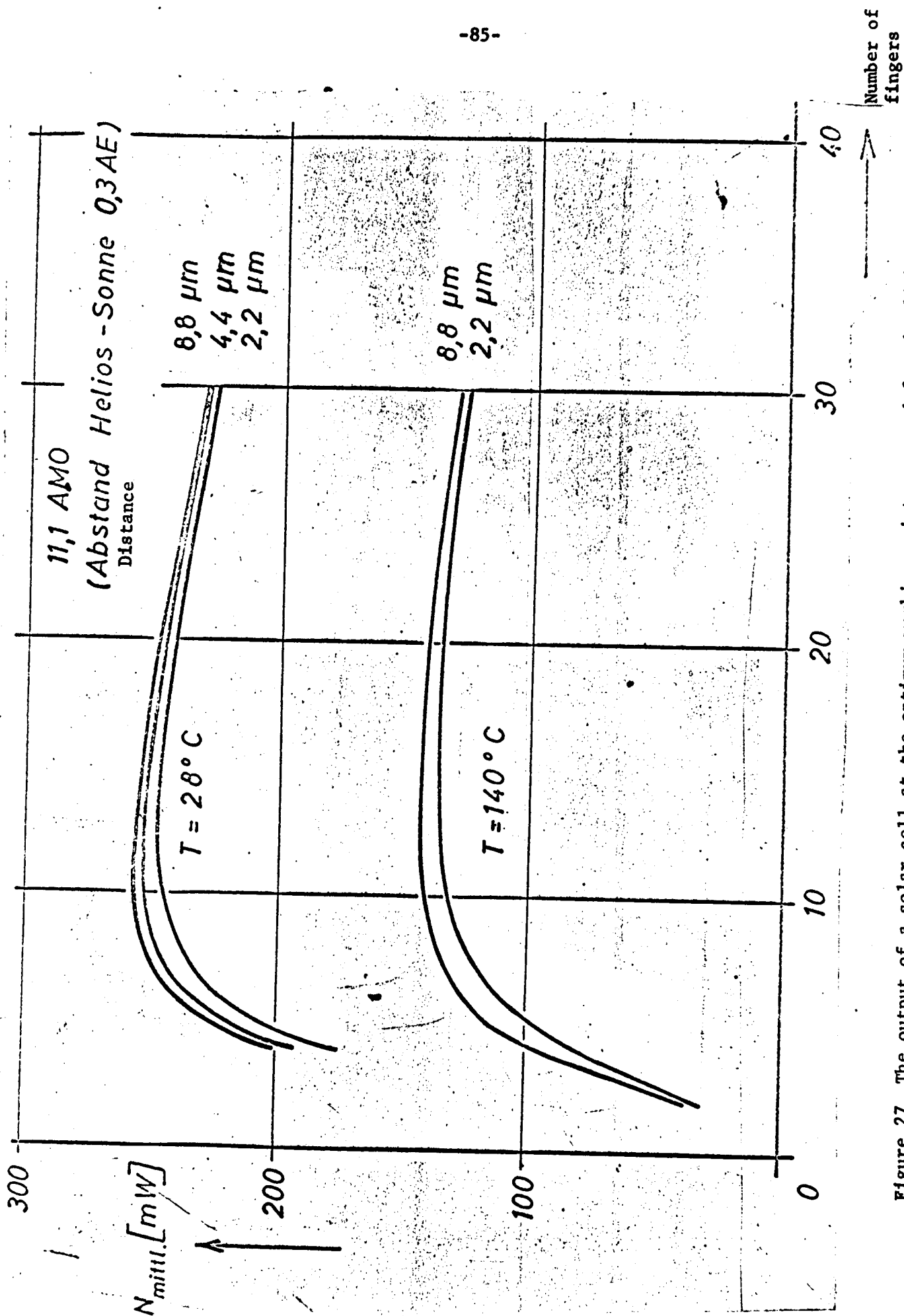


Figure 27 The output of a solar cell at the optimum working point averaged for the lighted semi-rotation of a spool in relation to the number of grid fingers.
Parameter: temperature and finger depth.

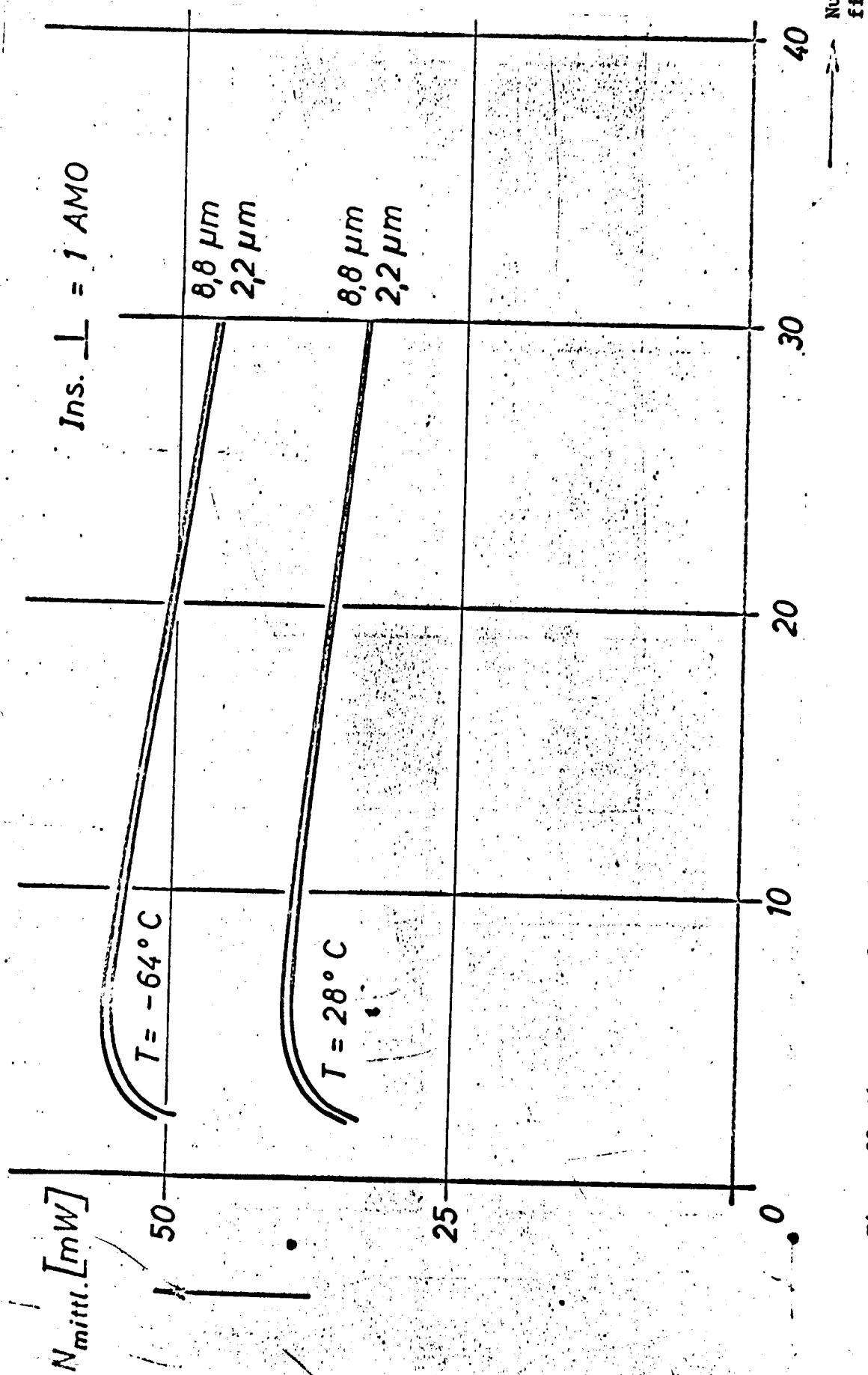


Figure 28 The output of a solar cell at the optimum working point averaged for the lighted semi-rotation of a spool in relation to the number of grid fingers.
Parameter: temperature and finger depth.
($Z_F = 7$ and $F_T = 4.4/\mu m$ correspond to type V).

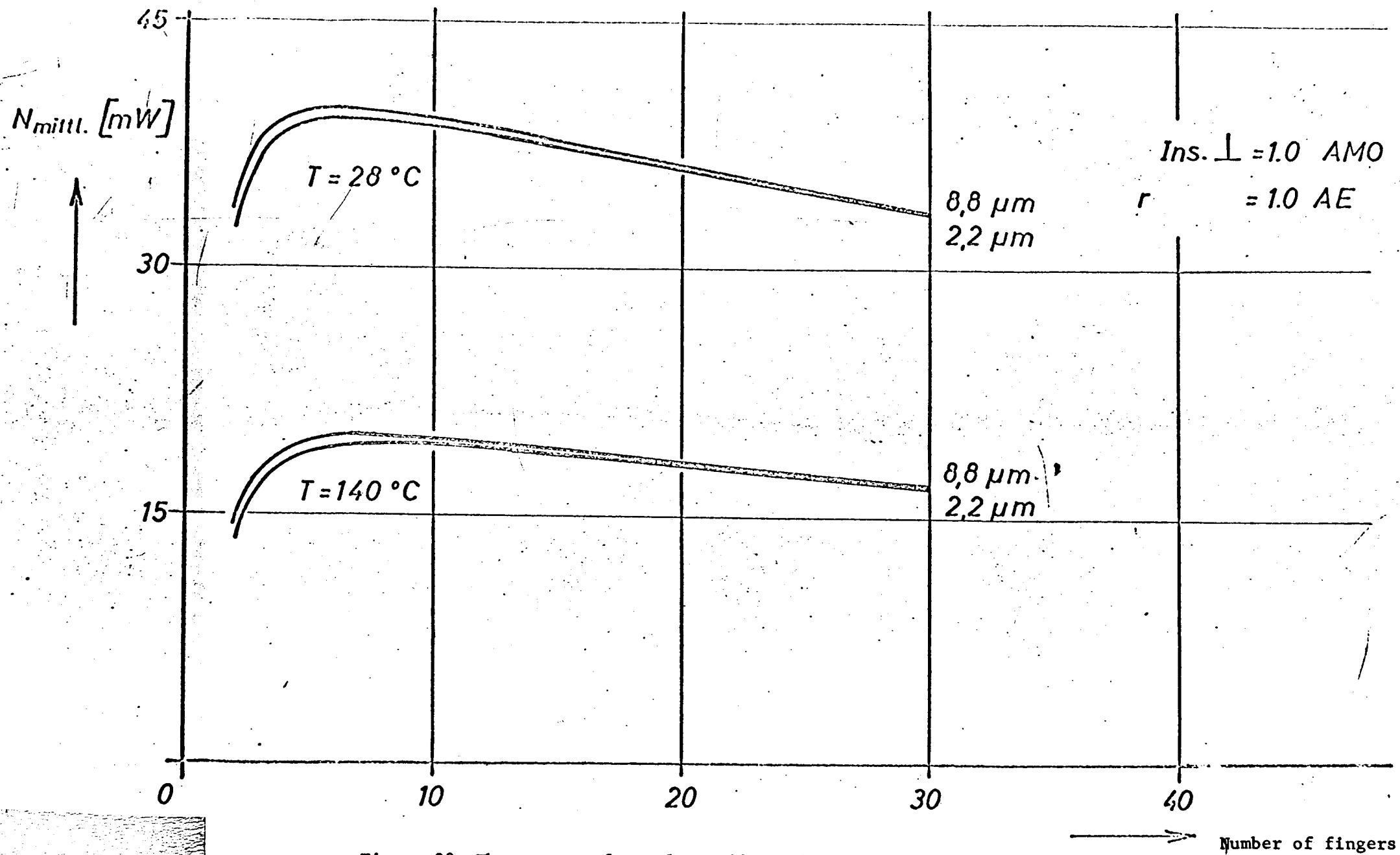


Figure 29 The output of a solar cell at the optimum working point averaged for the lighted semi-rotation of a spool in relation to the number of grid fingers. Parameter: temperature and finger depth. ($Z_F = 7$ and $F_T = 4.4 \mu m$ correspond to type V).

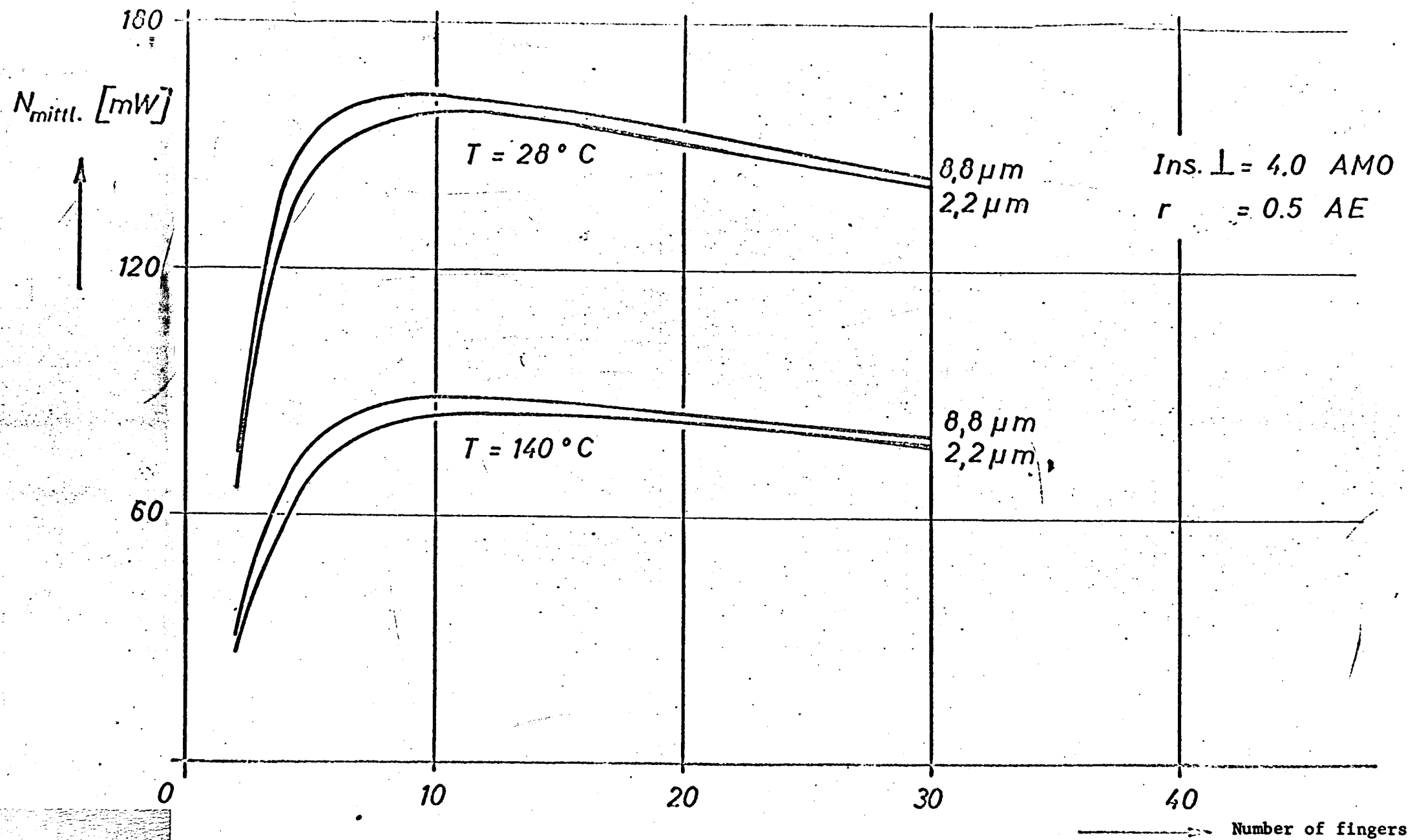


Figure 30 The output of a solar cell at the optimum working point averaged for the lighted semi-rotation of a spool in relation to the number of grid fingers. Parameter: temperature and finger depth. ($Z_F = 7$ and $F_T = 4.4 \mu\text{m}$ correspond to type V).

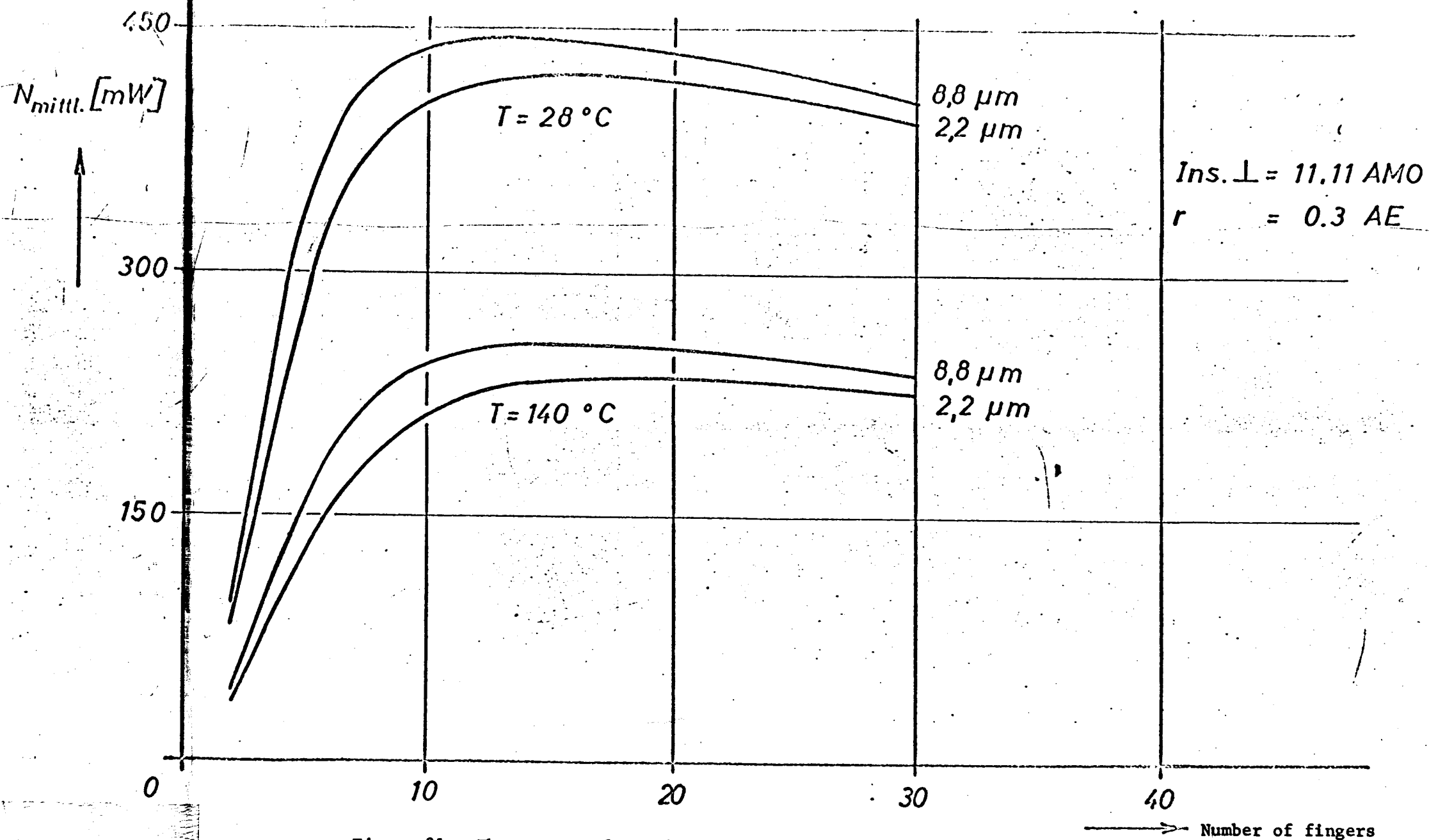


Figure 31: The output of a solar cell at the optimum working point averaged for the lighted semi-rotation of a spool in relation to the number of grid fingers. Parameter: temperature and finger depth. $Z_F = 7$ and $F_T = 4.4 \mu m$ correspond to type V).

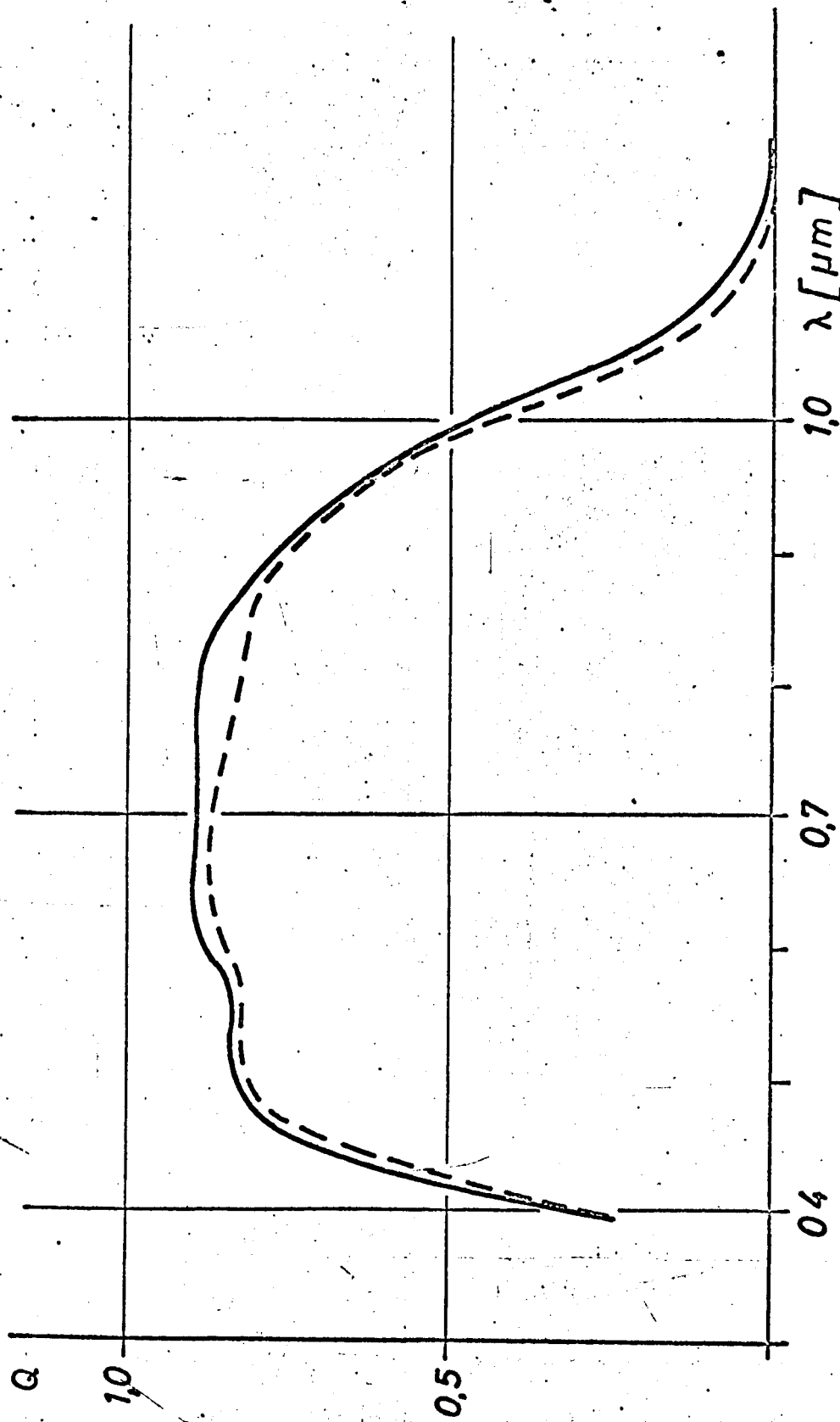


Figure 32 Measured quanta yield on silicon n/p solar cells in relation to the wave length of the incident light.

Solid curve: standard cell type IV

Broken curve: standard cell type V.

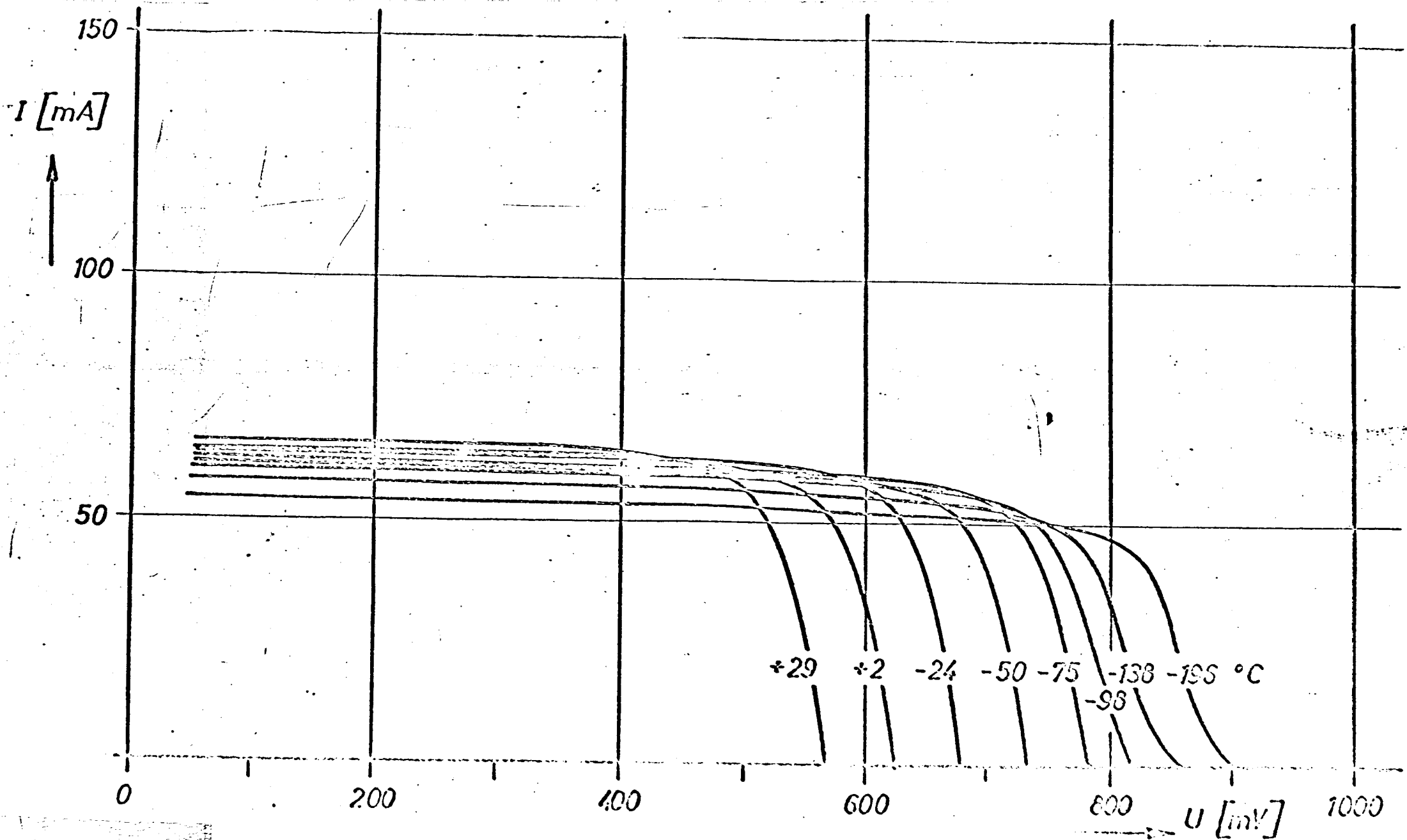


Figure 33 I/U curves of a type V solar cell under an insolation of 0.5 AMO and temperatures from $+29^{\circ}\text{C}$ to -196°C .

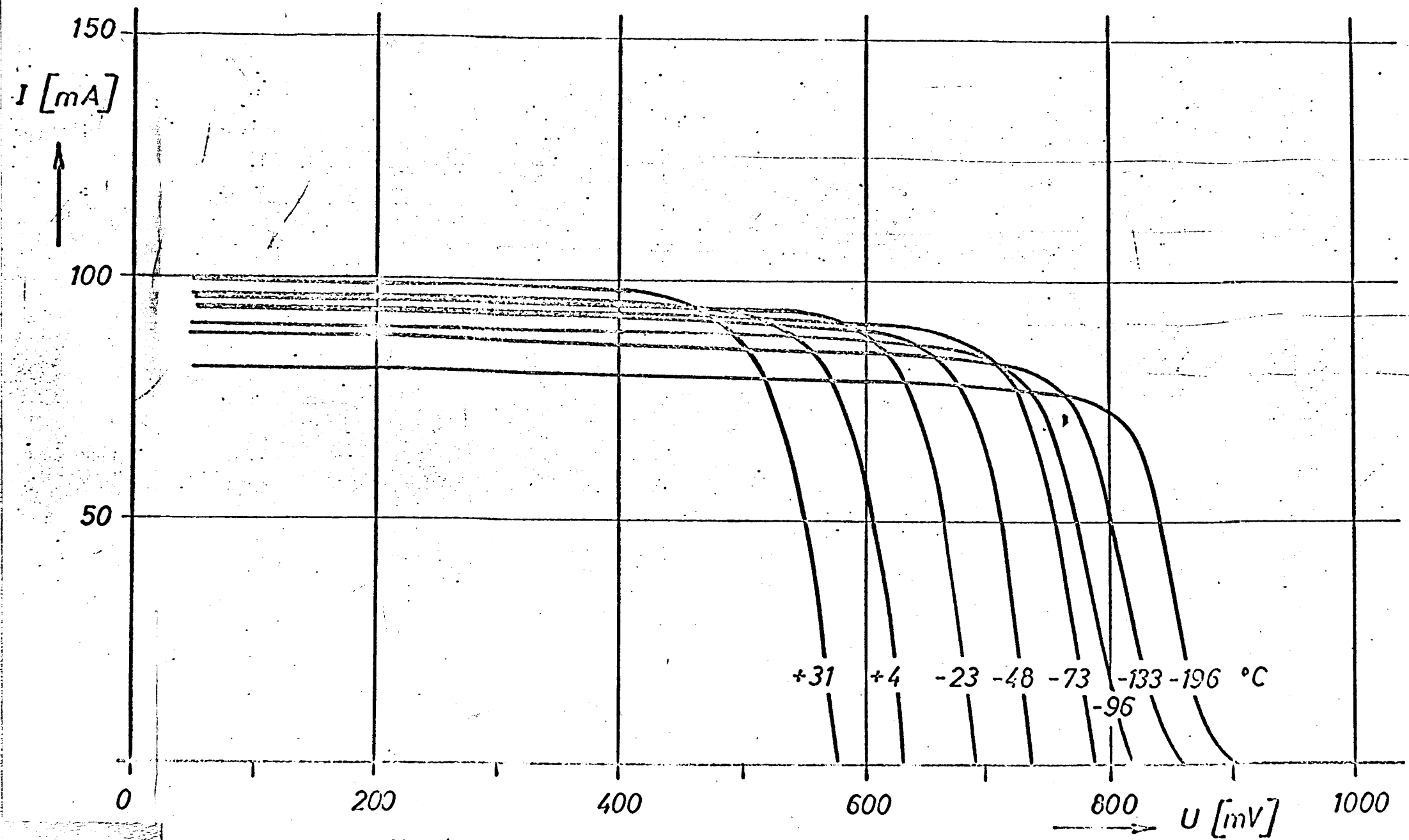


Figure 34 I/U curves of a type V solar cell under an insolation of 0.75 AMO and temperatures from +31°C to -196°C.

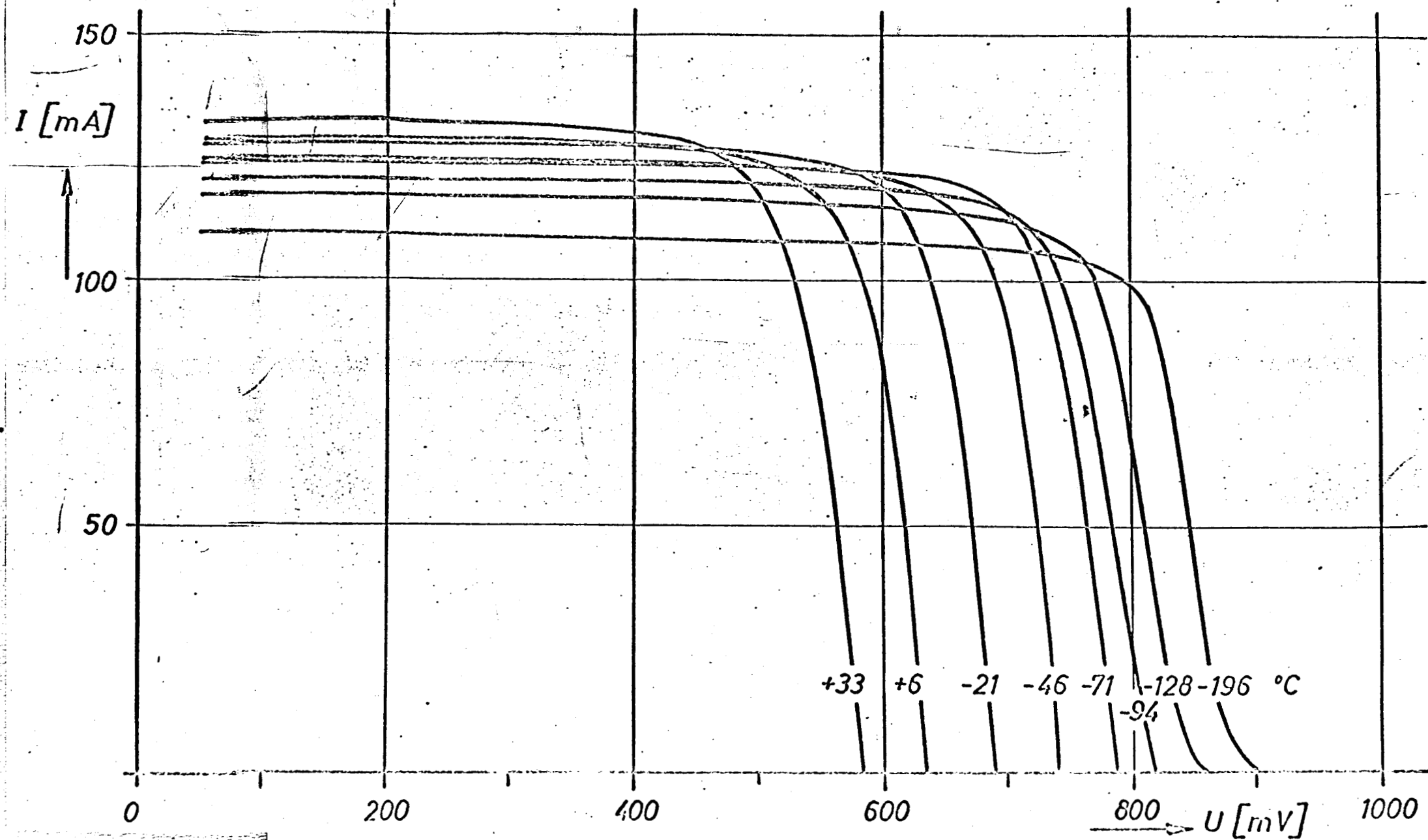


Figure 35 I/U curves of a type V solar cell under an insolation of 1 AMO and temperatures from +33°C to -196°C.

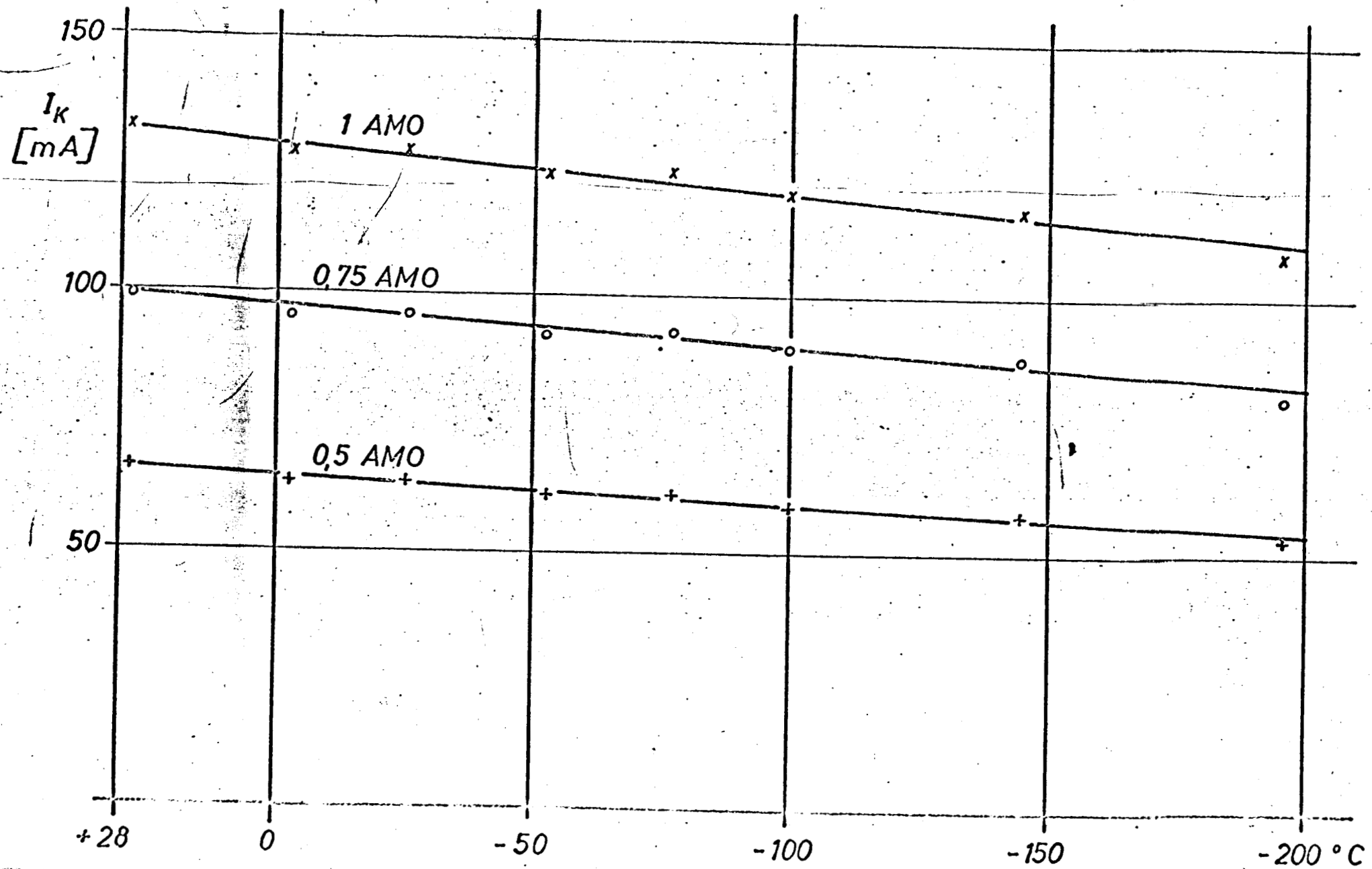


Figure 36 Short circuit current of a type V solar cell at temperatures from +28°C to -196°C under small insulations.

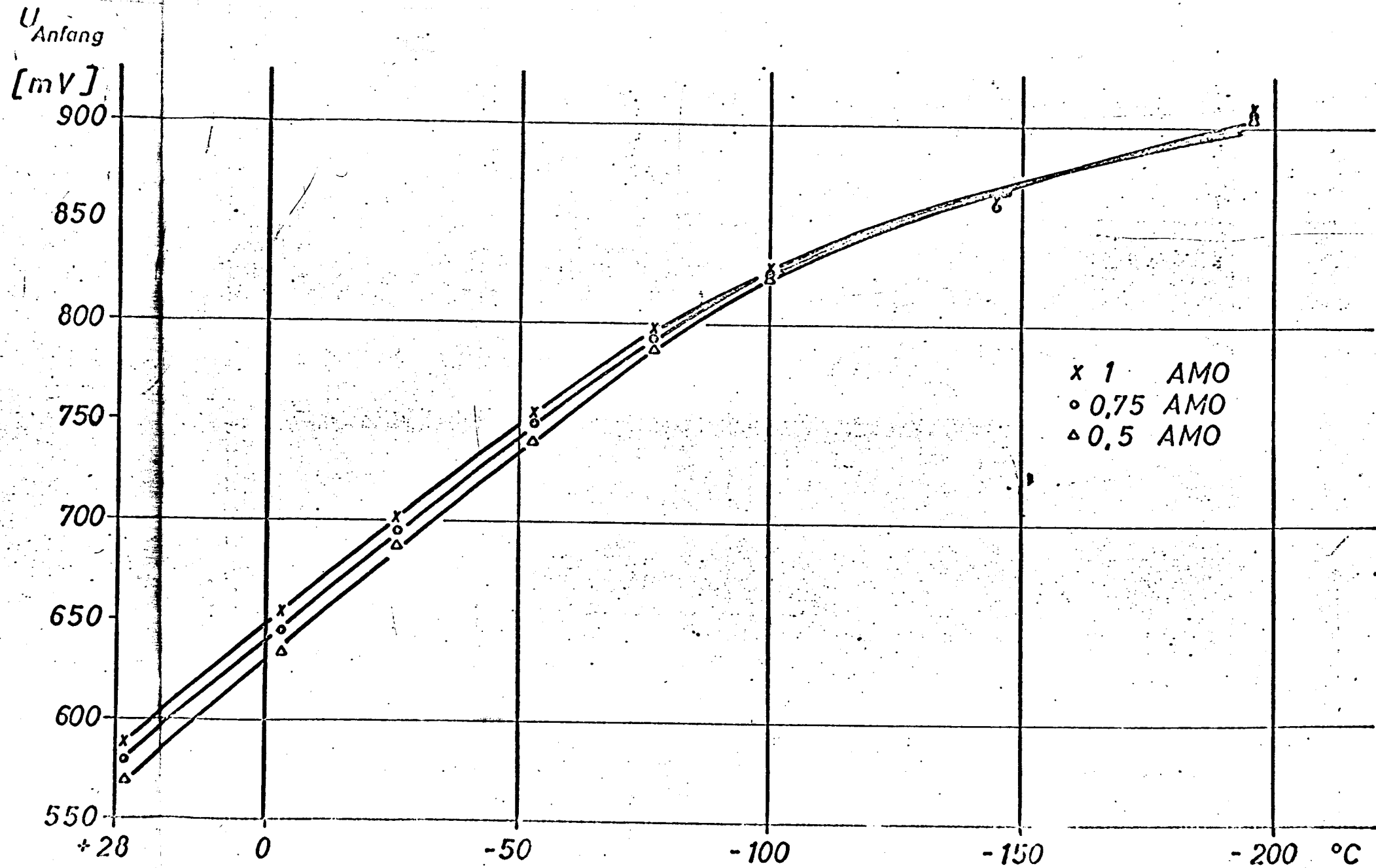


Figure 37 Idling potential of a type V solar cell at temperatures from +28°C to -196°C under small insulations.

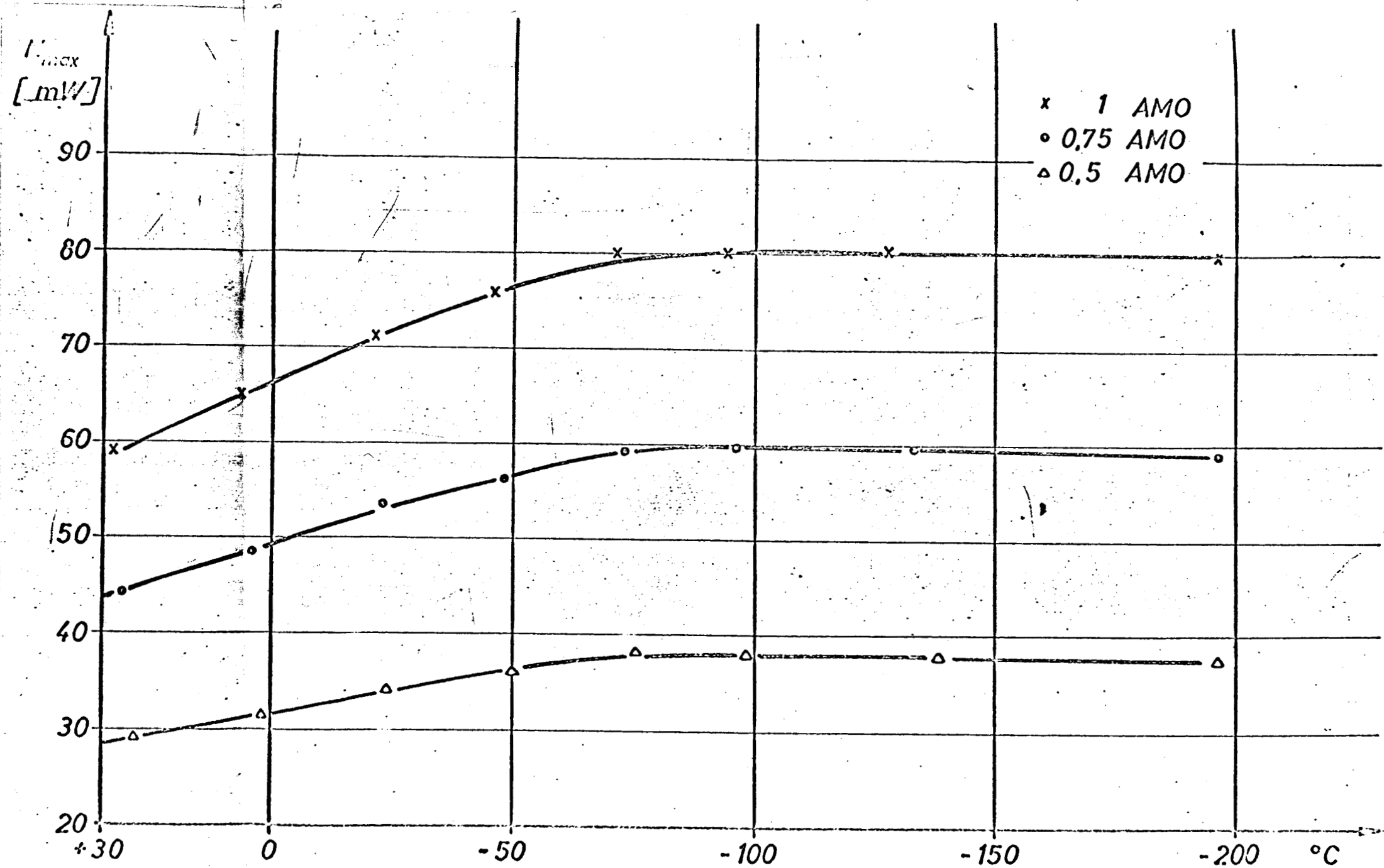


Figure 38 Maximum output of a type V solar cell at temperatures from +28°C to -196°C under small insulations.

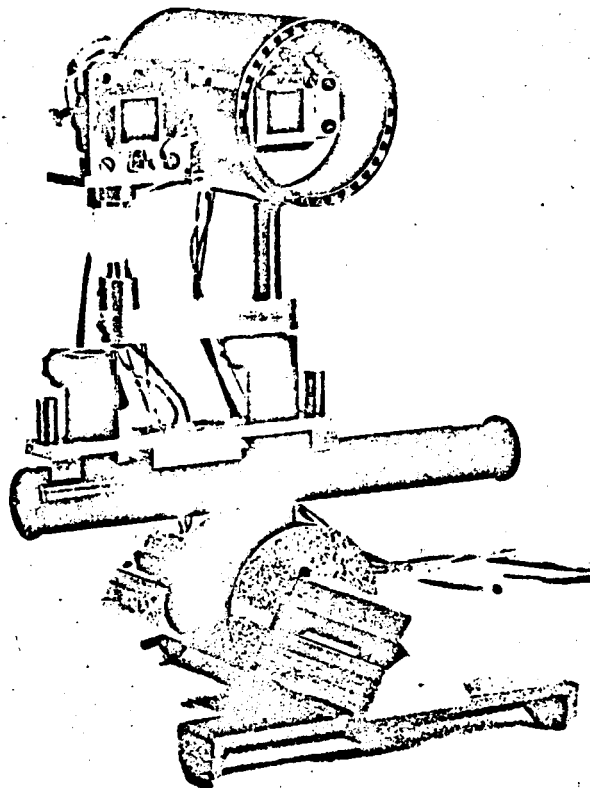


Figure 39 High temperature measuring mounting.
At left, the water-cooled standard cell;
at right the cell to be measured in the
convection and contact safety device.

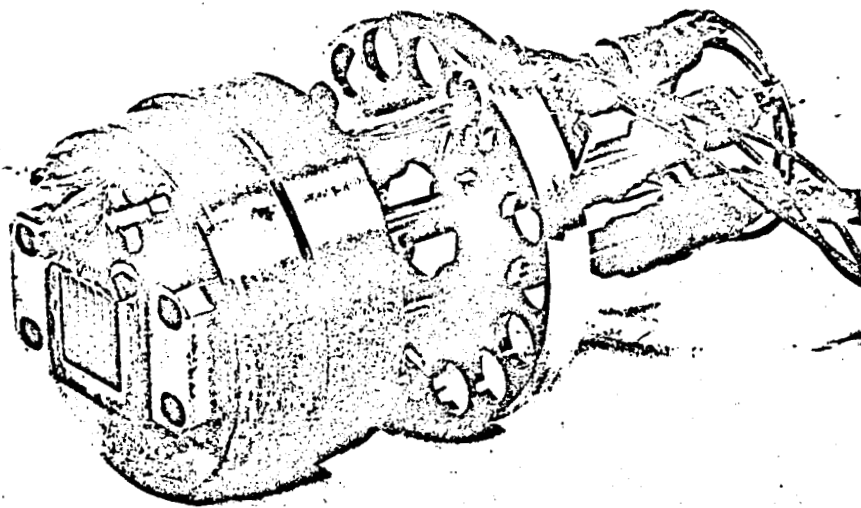


Figure 40 Internal part of the high temperature measuring mounting. The solar cell soldered on the solar cell carrier is fastened onto the heatable metal block of great heat capacity. For measurements of current and potential, separate lines are used. A thermoelement is screwed onto the solar cell carrier.

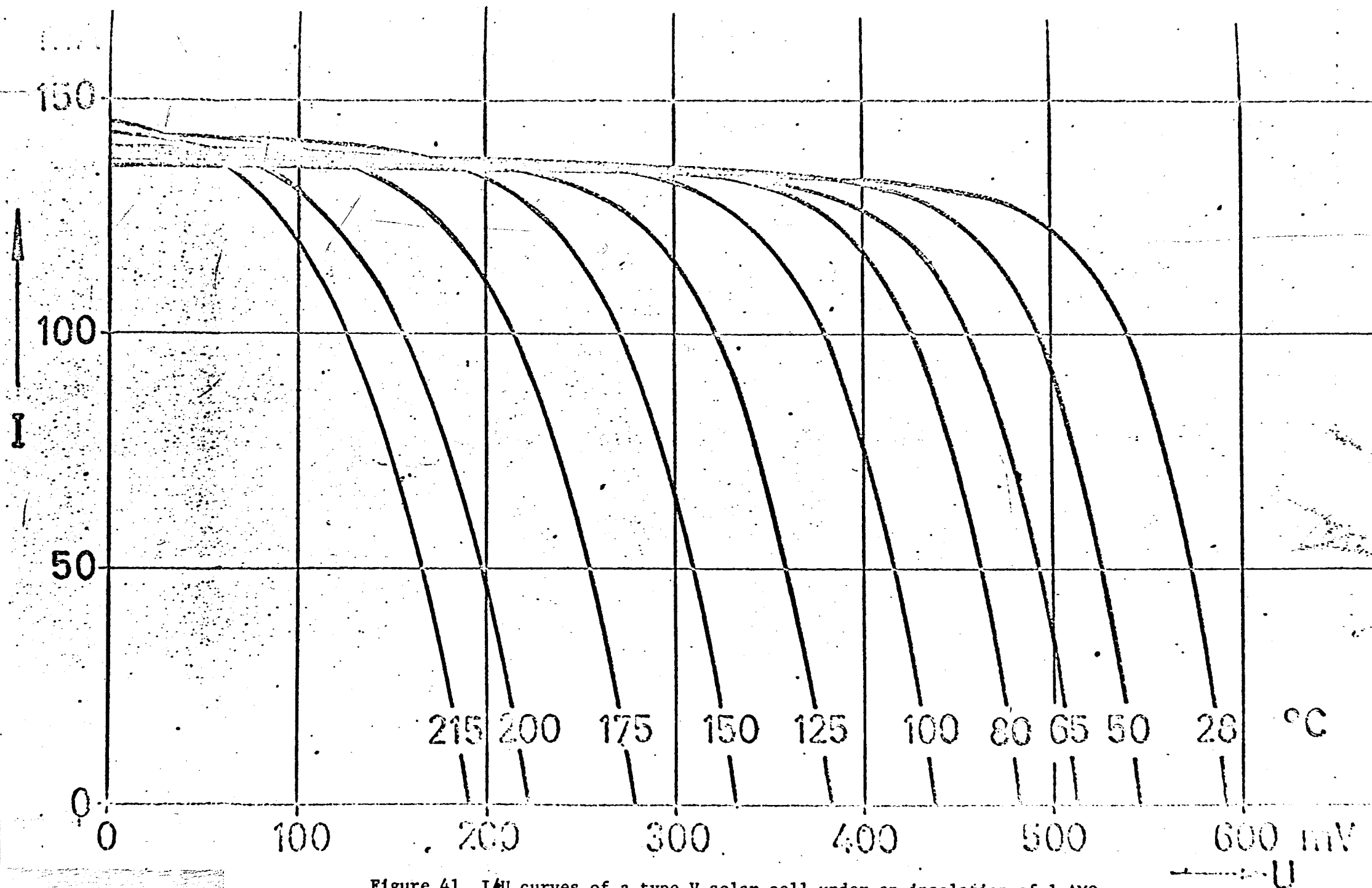


Figure 41 I/U curves of a type V solar cell under an insolation of 1 AMO at temperatures from +28°C to +215°C.

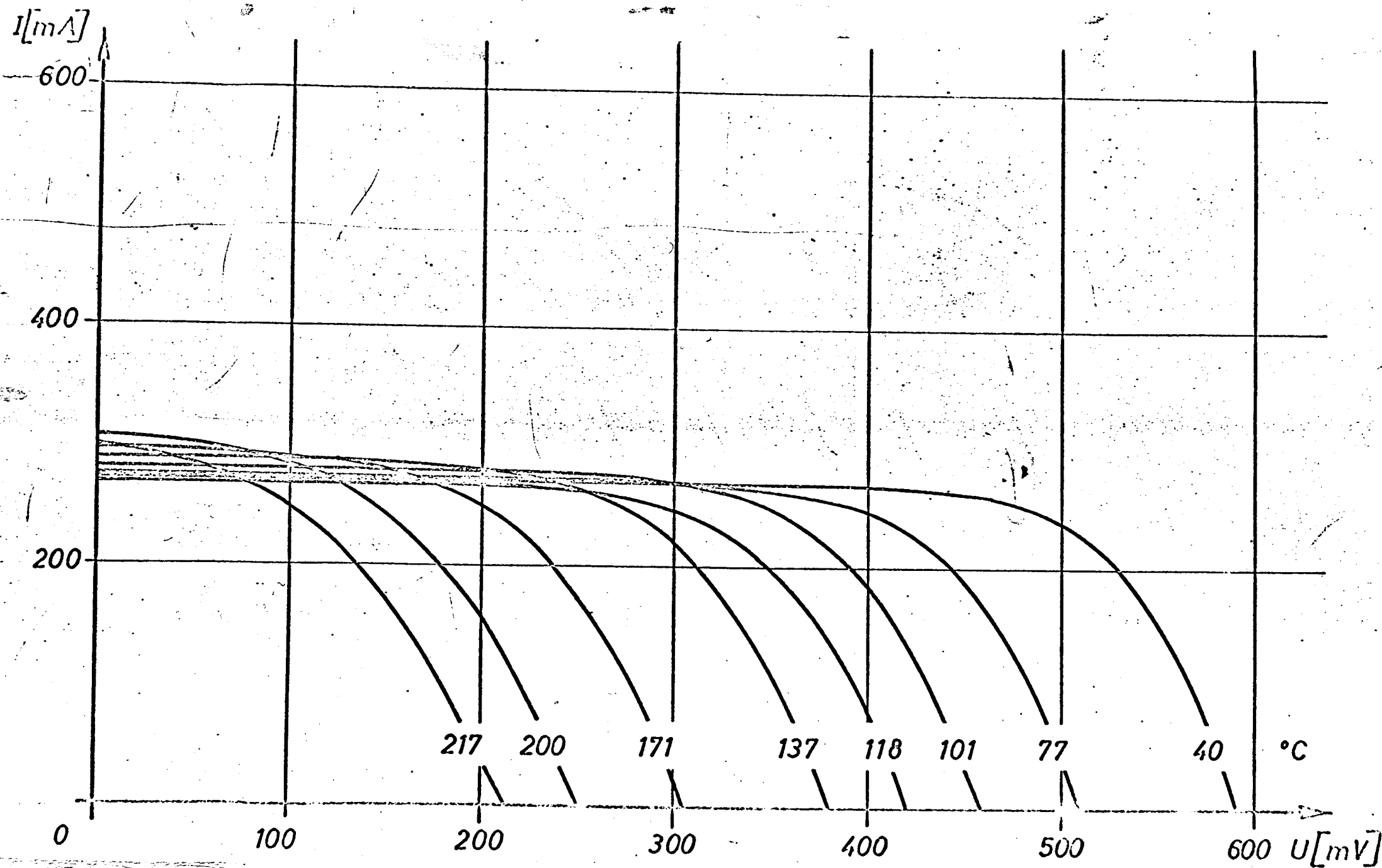


Figure 42 I/U curves of a type V solar cell under an insolation of 2 AMO at temperatures from $+40^{\circ}\text{C}$ to $+217^{\circ}\text{C}$.

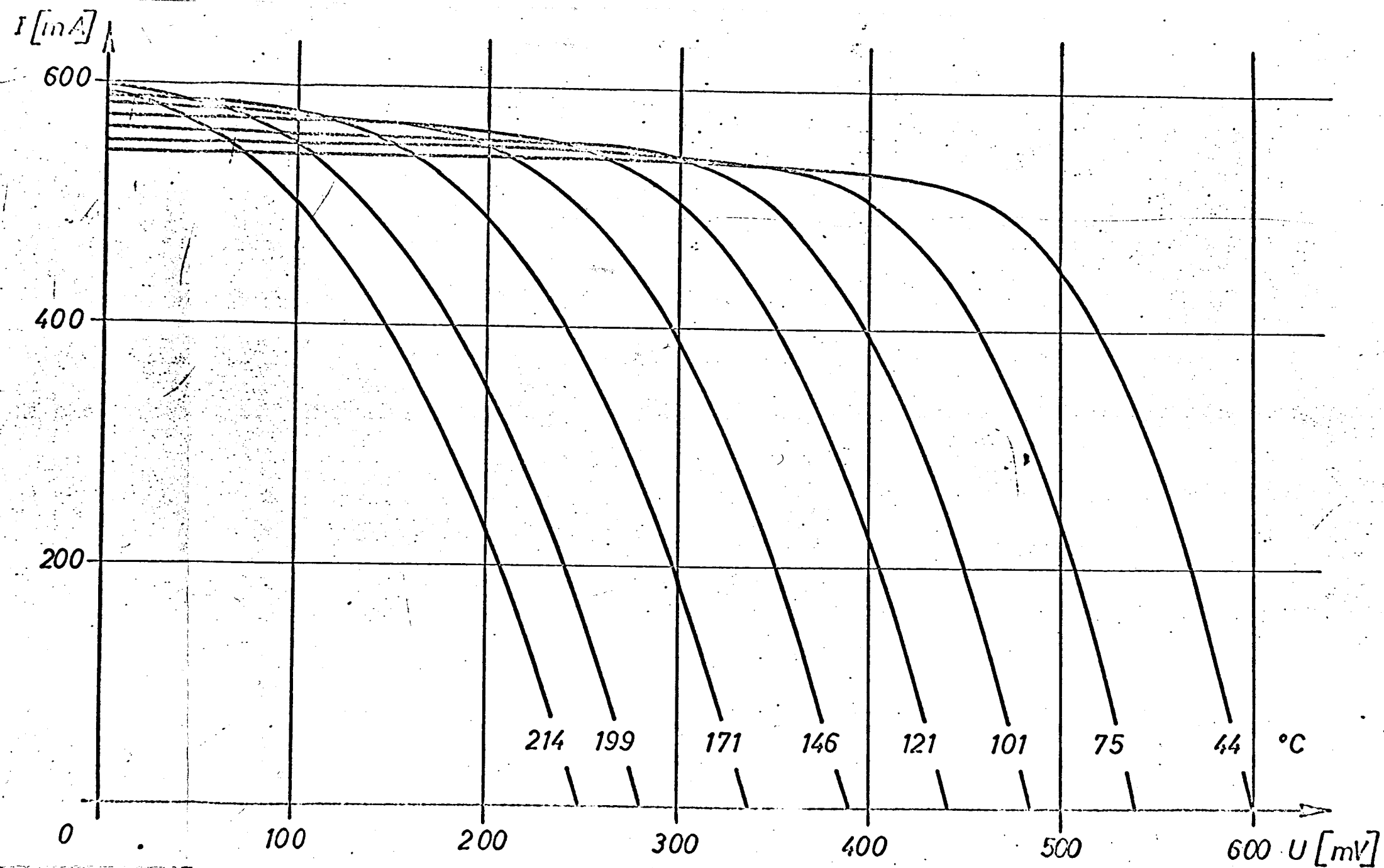


Figure 43. I/U curves of a type V solar cell under an insolation of 4 AMO at temperatures from +44°C to +214°C.

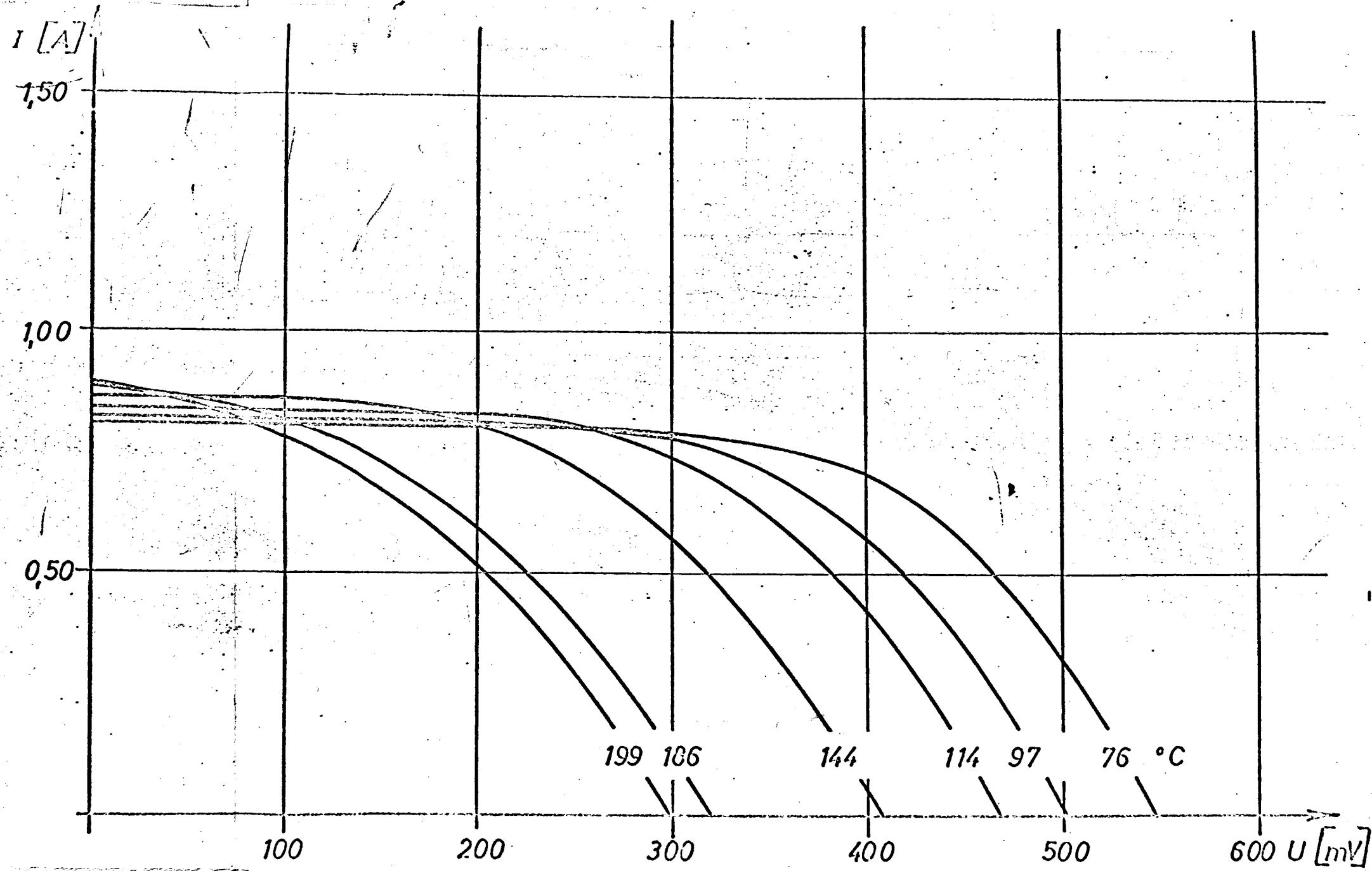


Figure 44 I/U curves of a type V solar cell under an insolation of 6 AMO at temperatures from +76°C to +199°C.

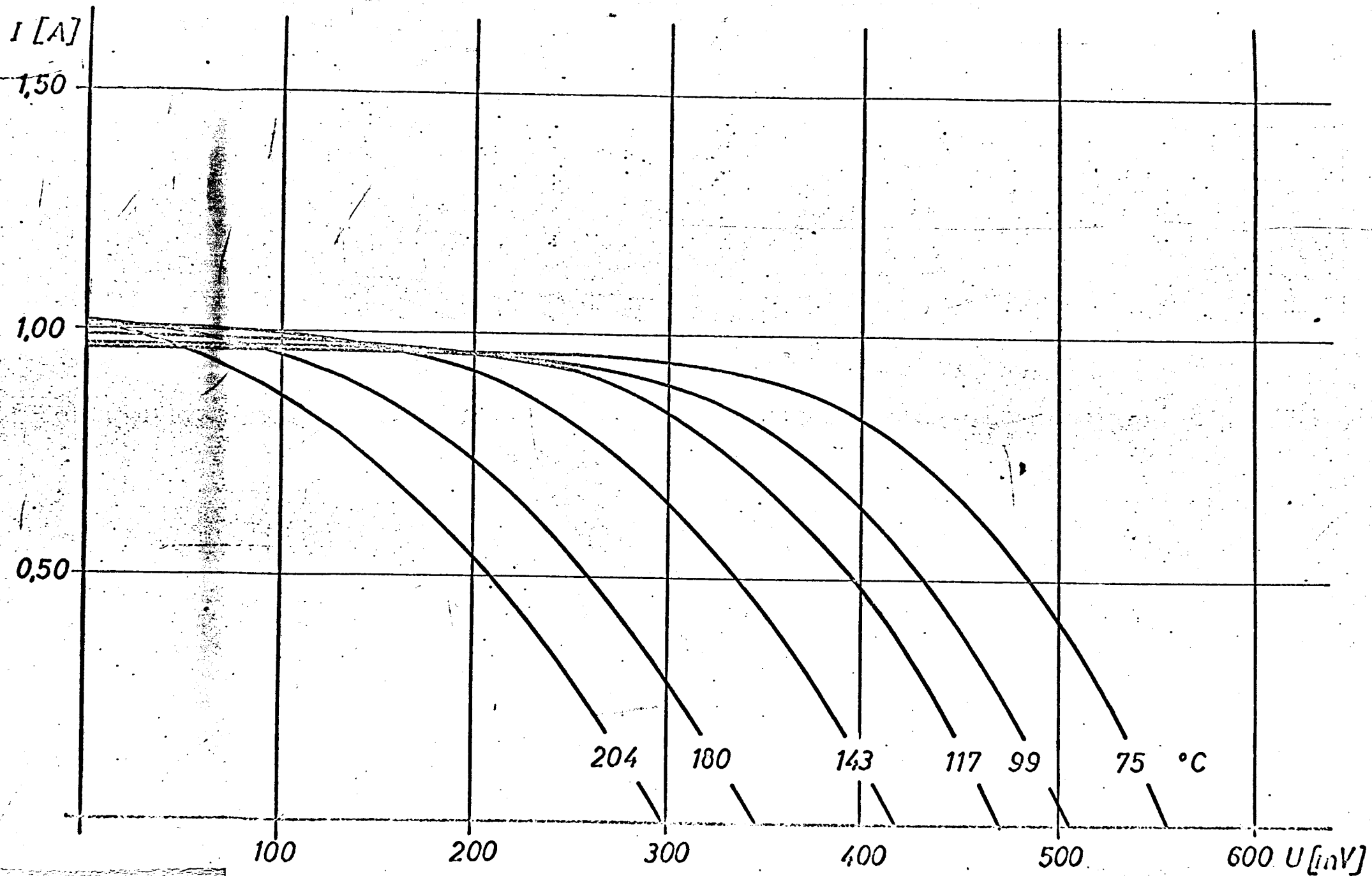


Figure 45 I/U curves of a type V solar cell under an insolation of 7 AMO at temperatures from +75°C to +204°C.

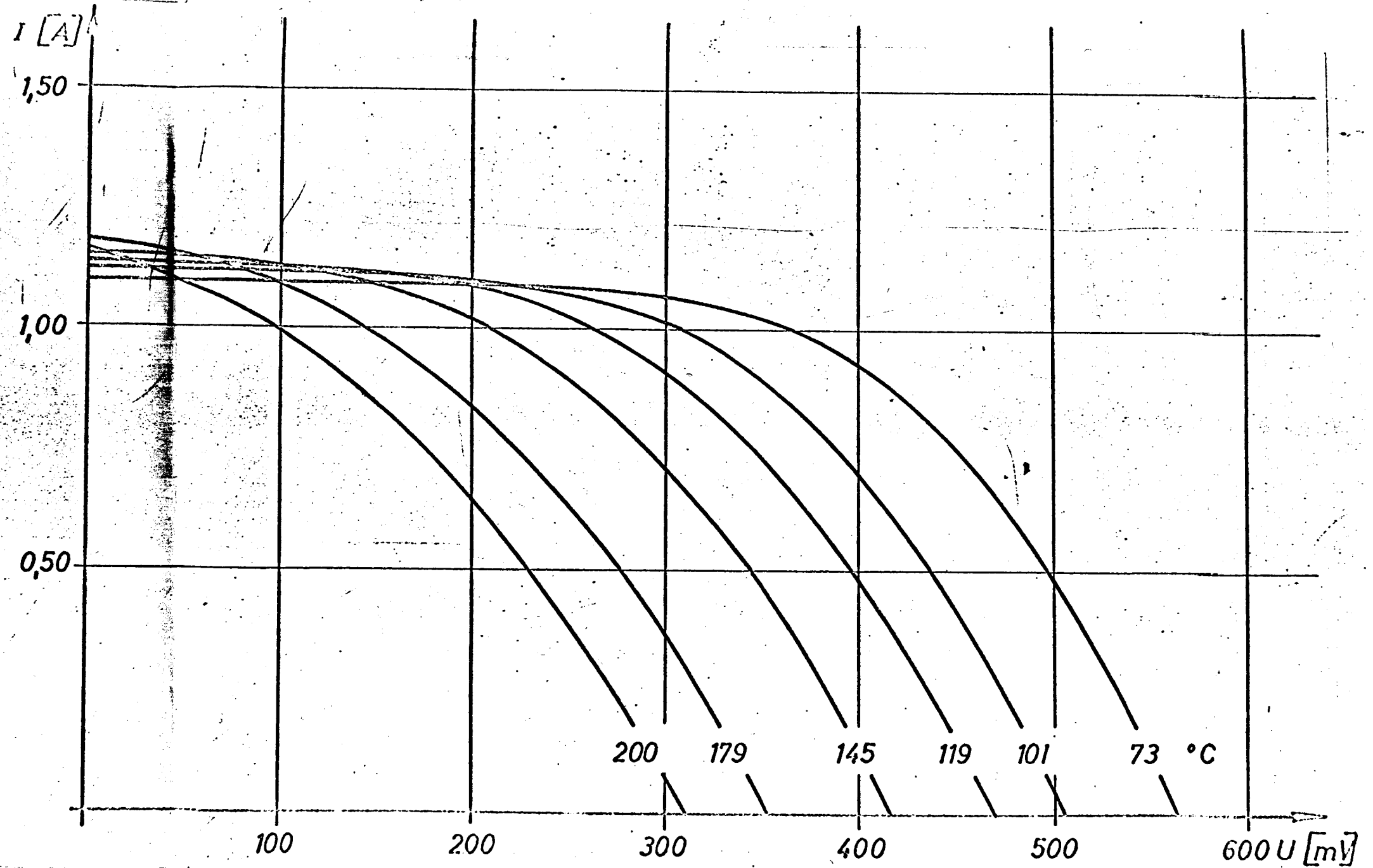


Figure 46 I/U curves of a type V solar cell under an insolation of 8 AMO at temperatures from +73°C to +200°C.

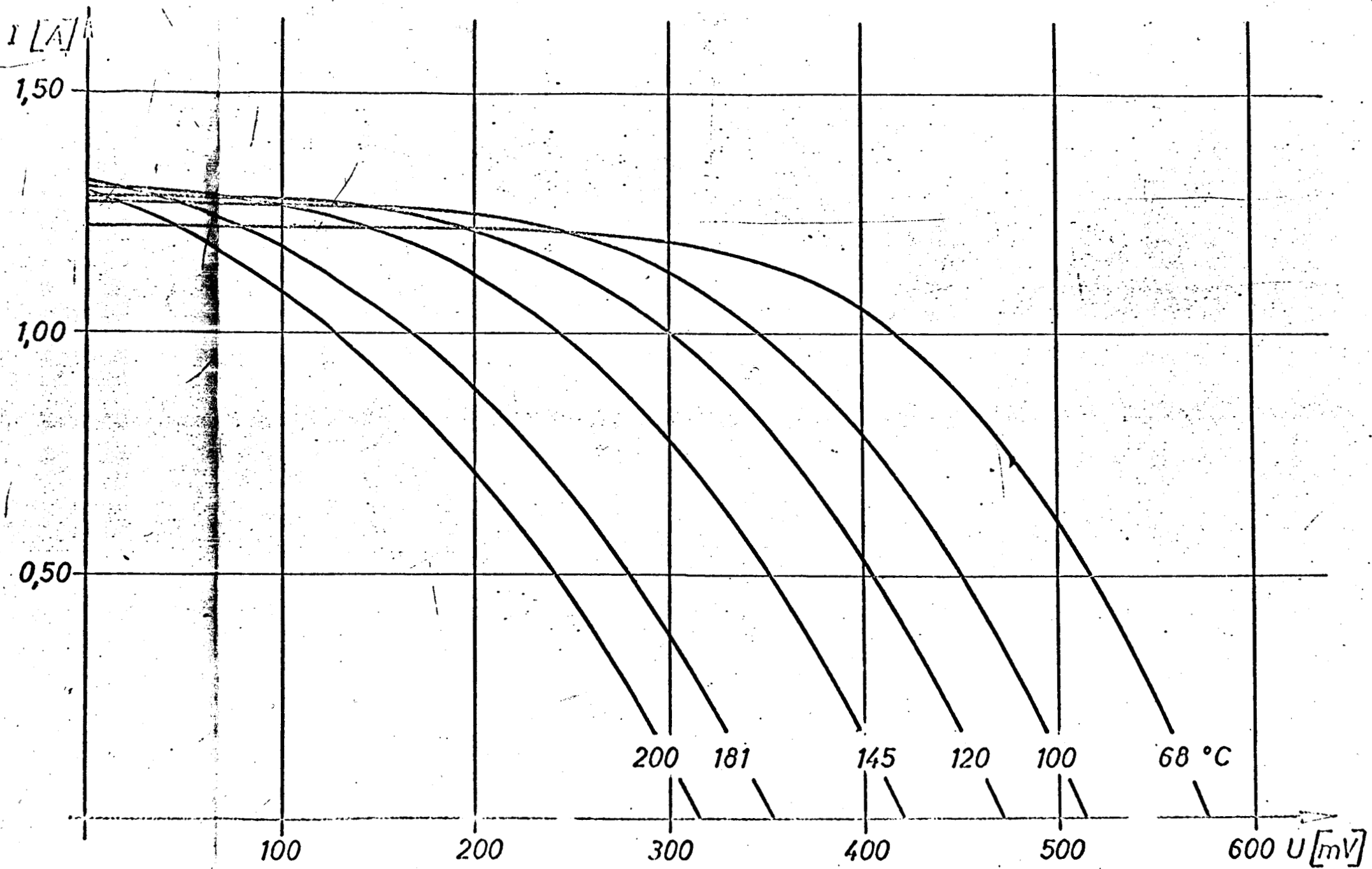


Figure 47 I/U curves of a type V solar cell under an insolation of 9 AMO at temperatures from +68°C to +200°C.

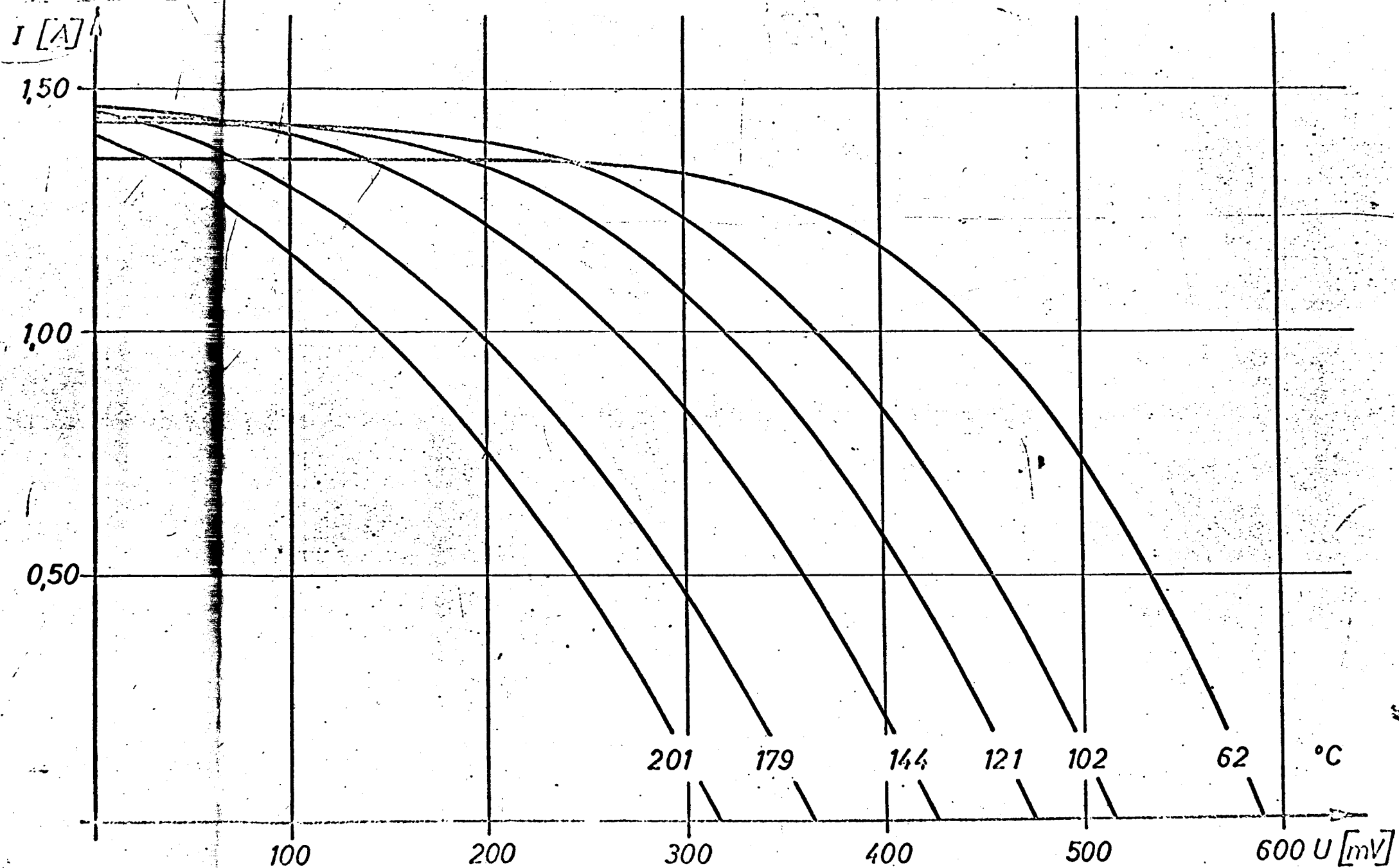


Figure 48 I/U curves of a type V solar cell under an insolation of 10 AMO at temperatures from +62°C to +201°C.

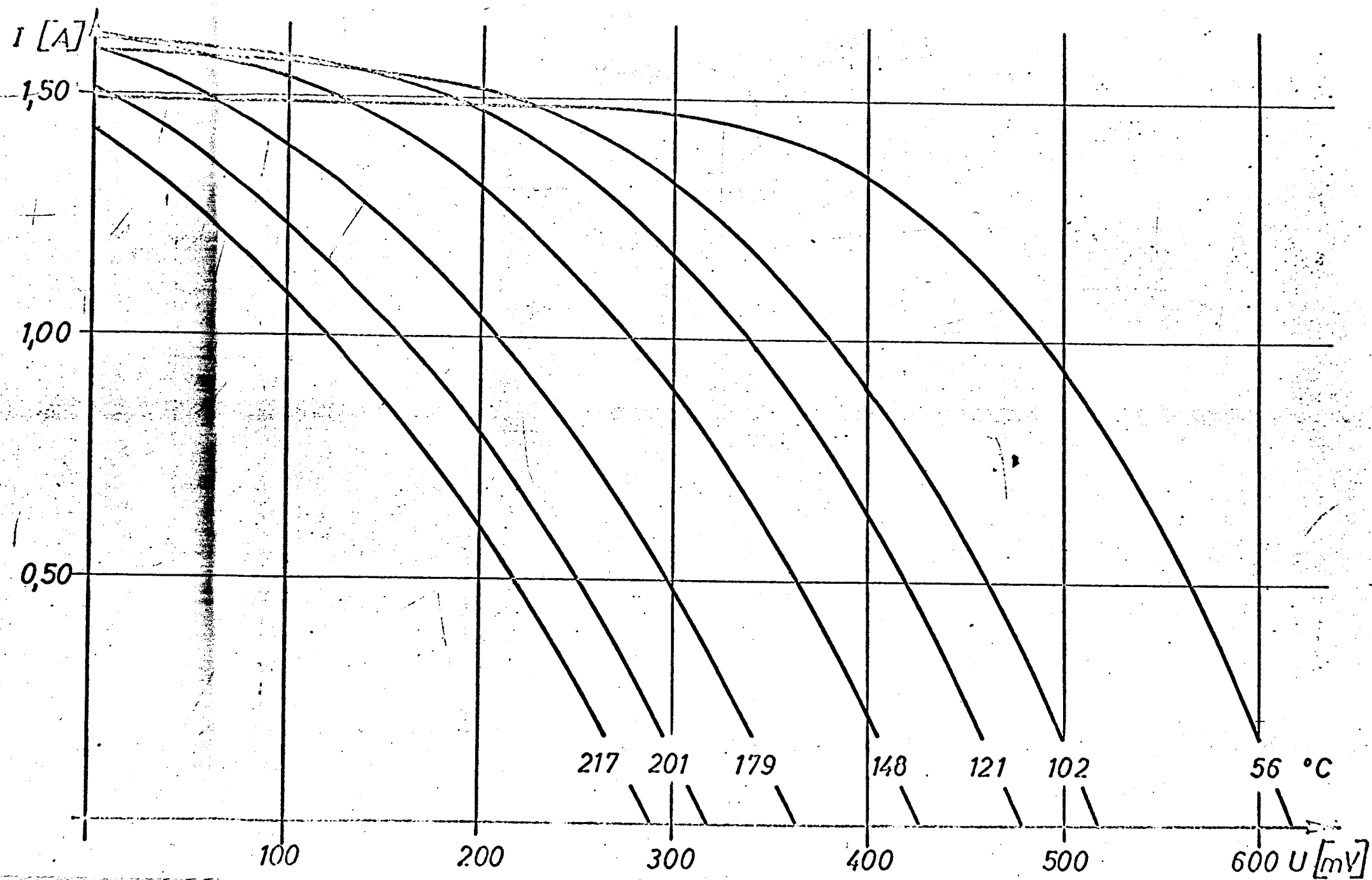


Figure 49 I/U curves of a type V solar cell under an insolation of 11 AM0 at temperatures from +56°C to +217°C.

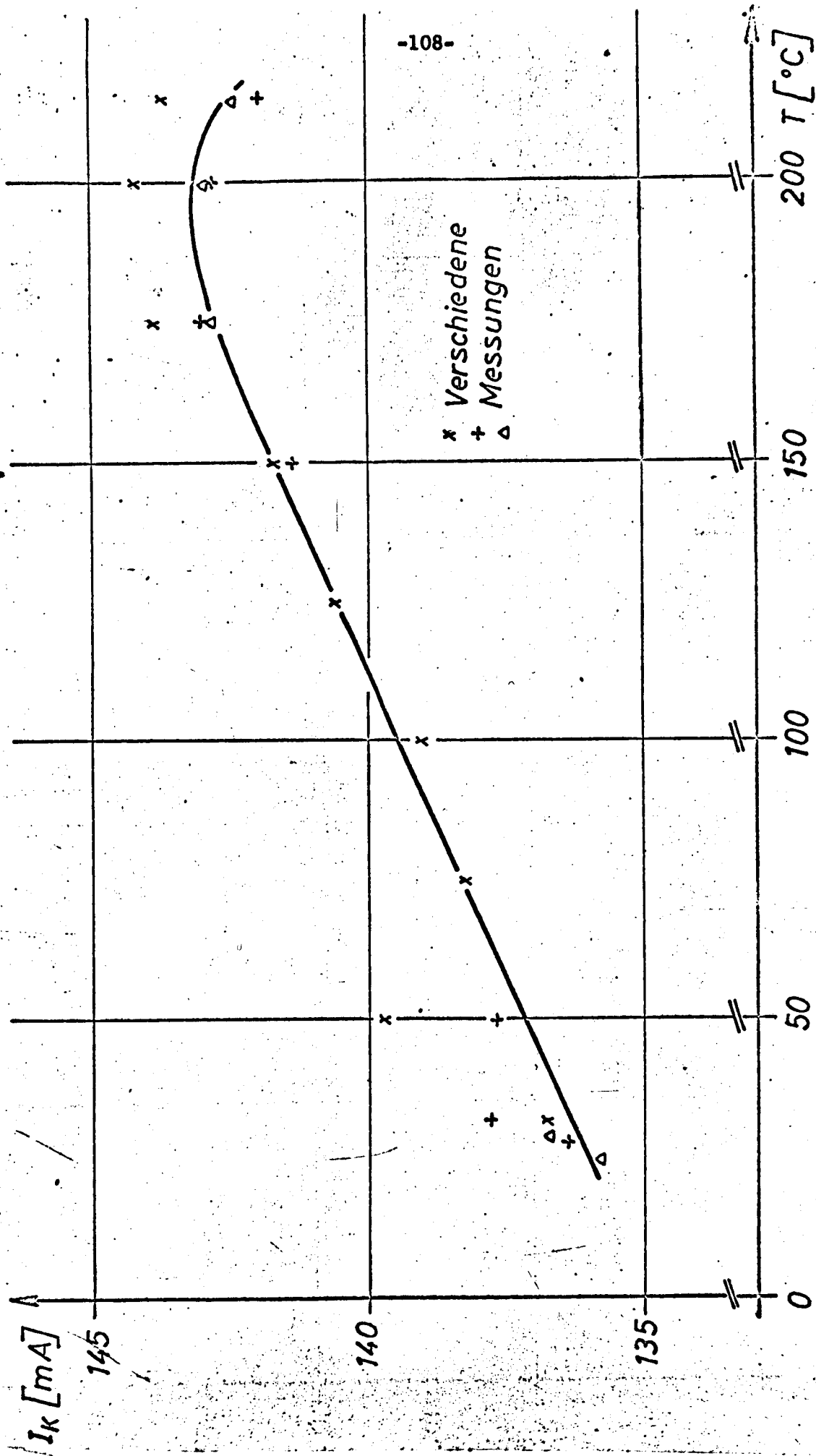


Figure 50 Short circuit current of a type V solar cell at temperatures from +28°C to +215°C under an insolation of 1 AMO.

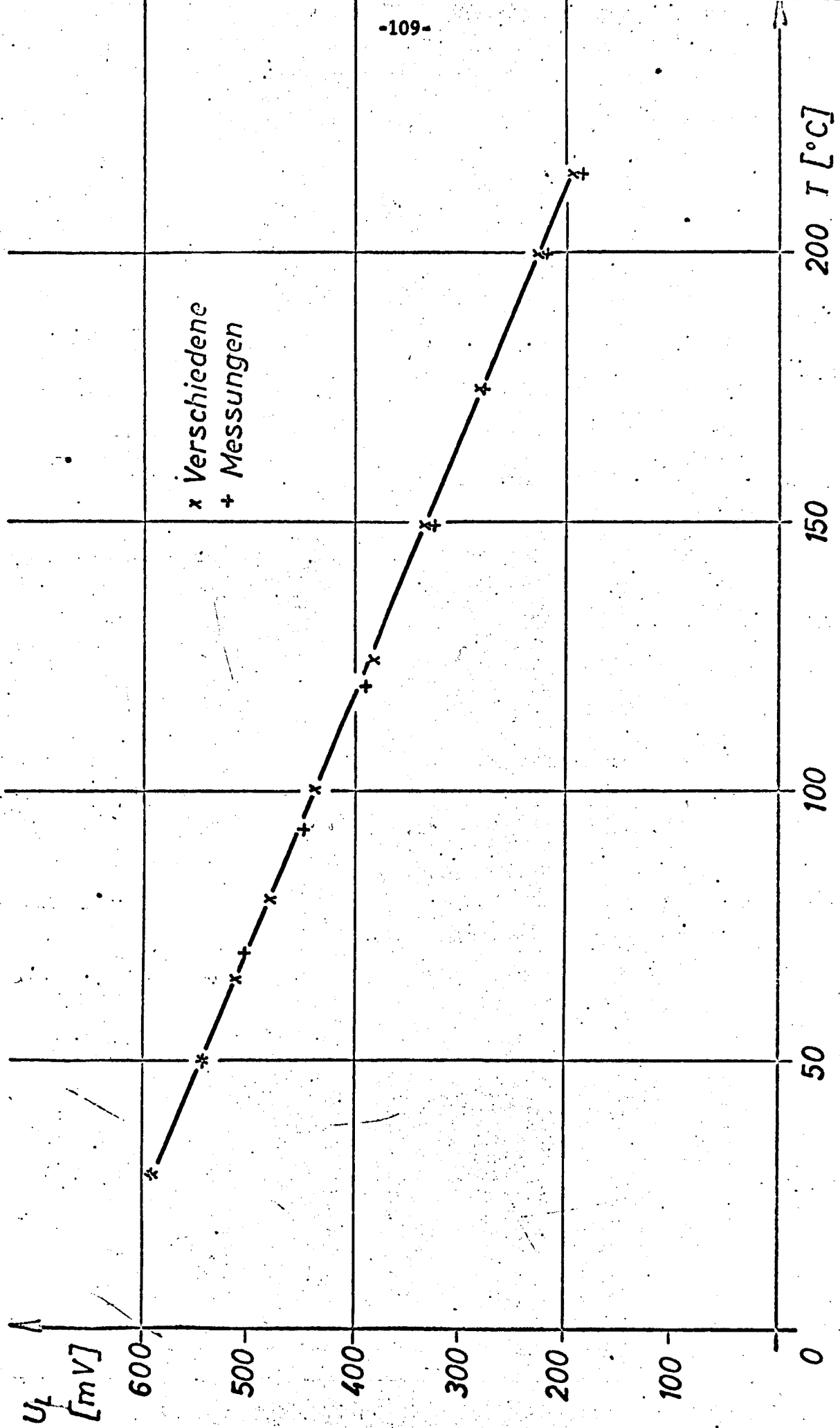


Figure 51 Idling potential of a type V solar cell at temperatures from +28°C to +215°C under an insolation of 1 AMO.

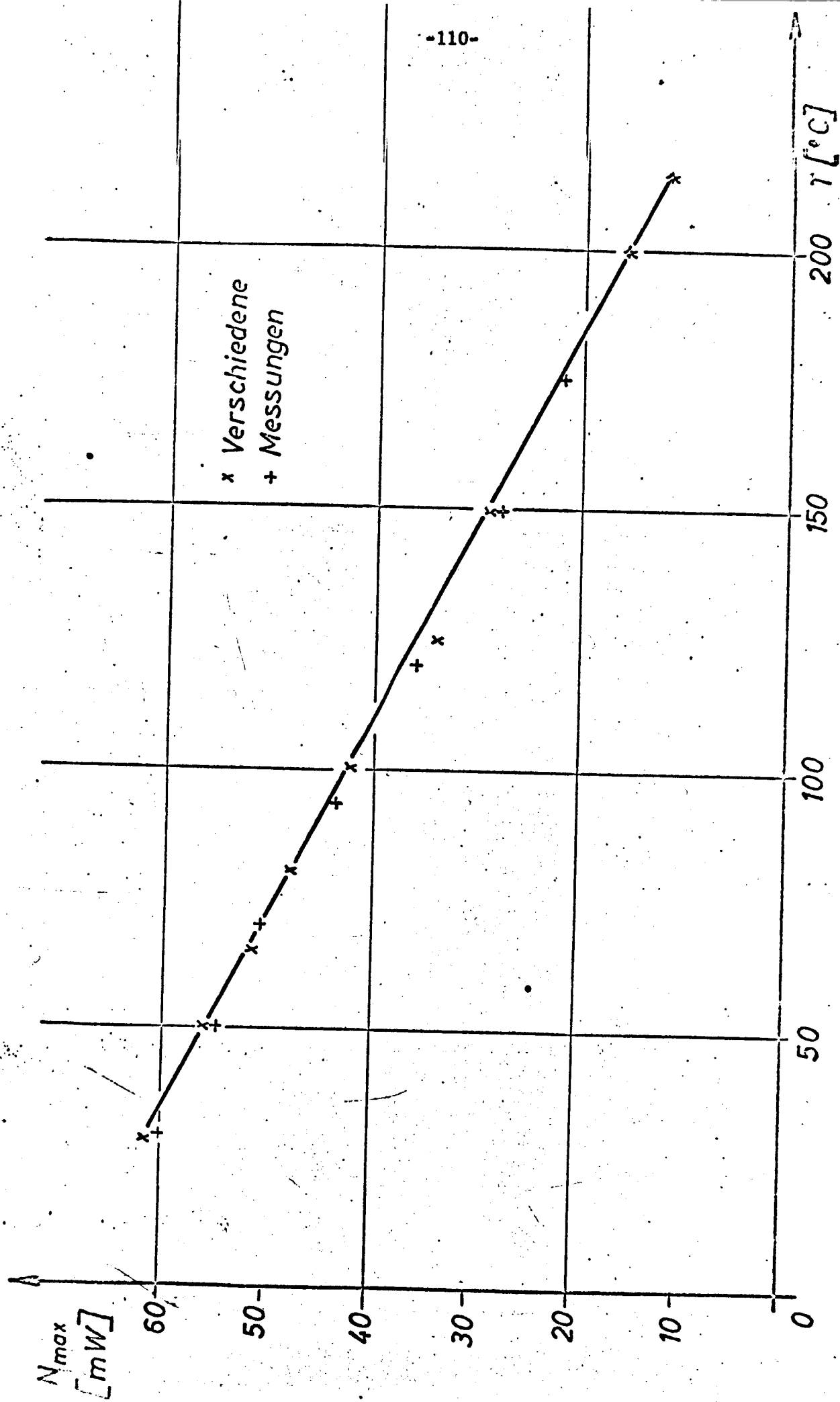


Figure 52 Maximum output of a type V solar cell at temperatures from +28°C to +215°C under an insolation of 1 AMO.

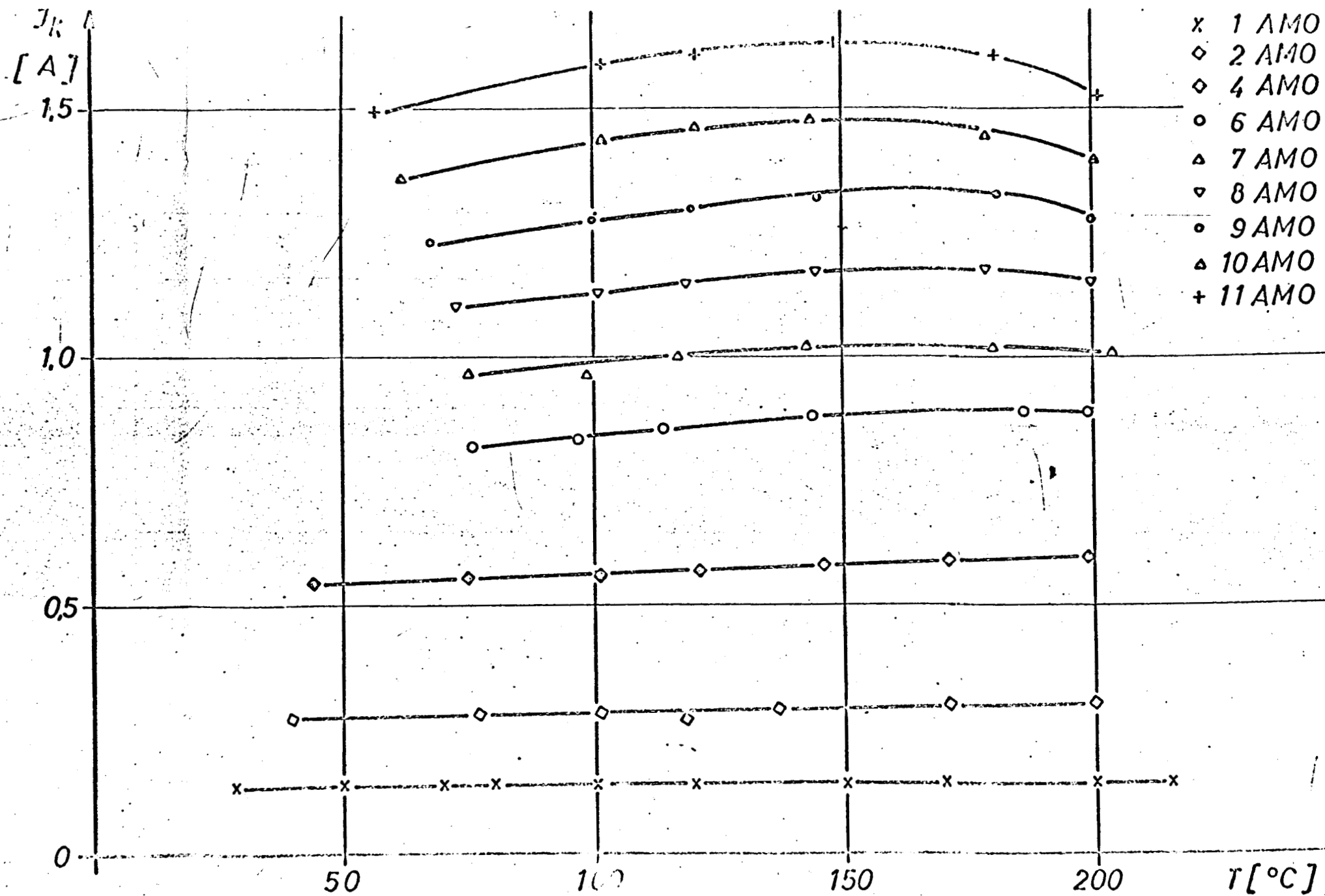


Figure 53 Short circuit current of a type V solar cell at temperatures from +40°C to +217°C under high insulations up to 11 AMO.

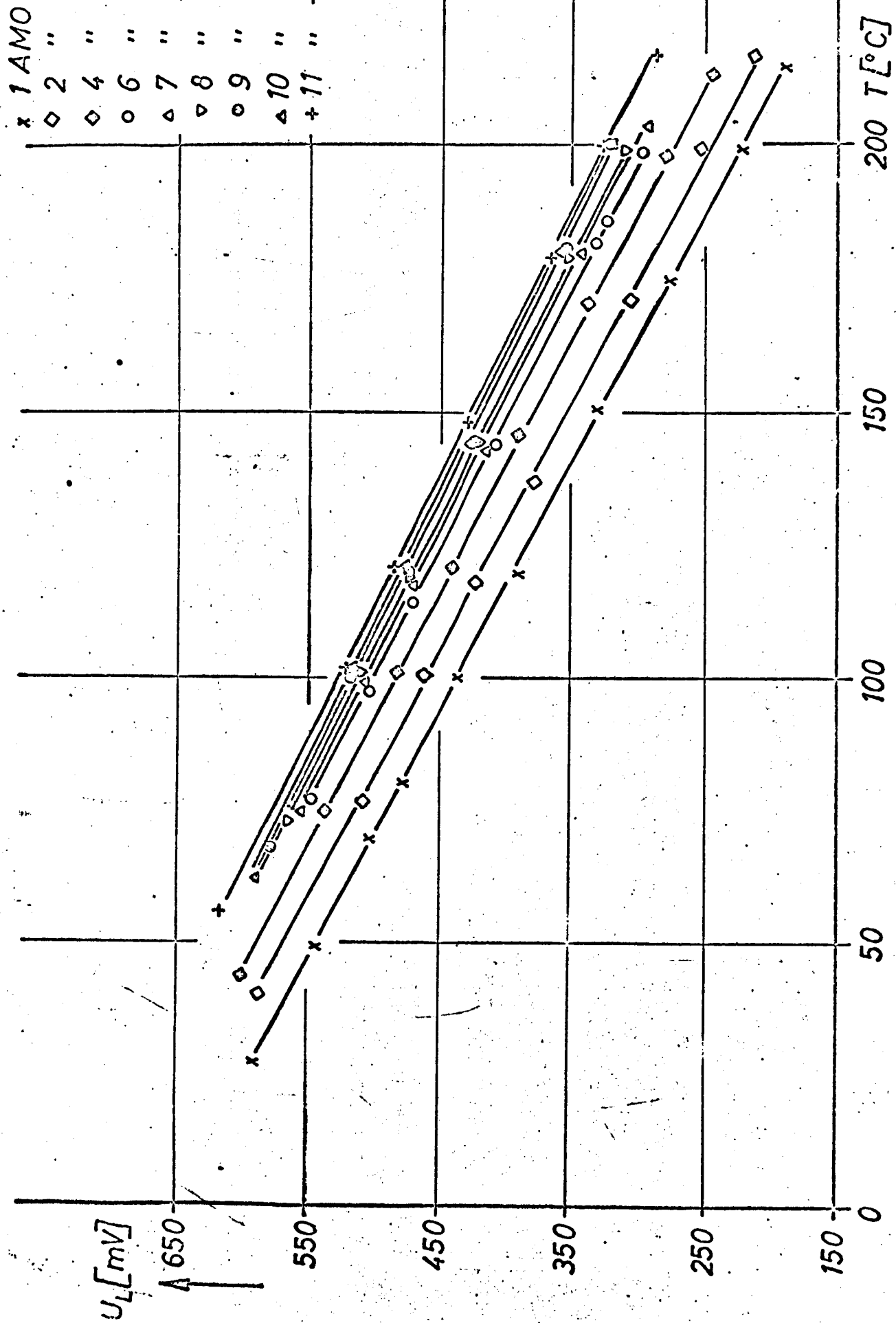


Figure 54 Idling potential of a type V solar cell at temperatures from +40°C to +217°C under high insulations up to 11 AMO.

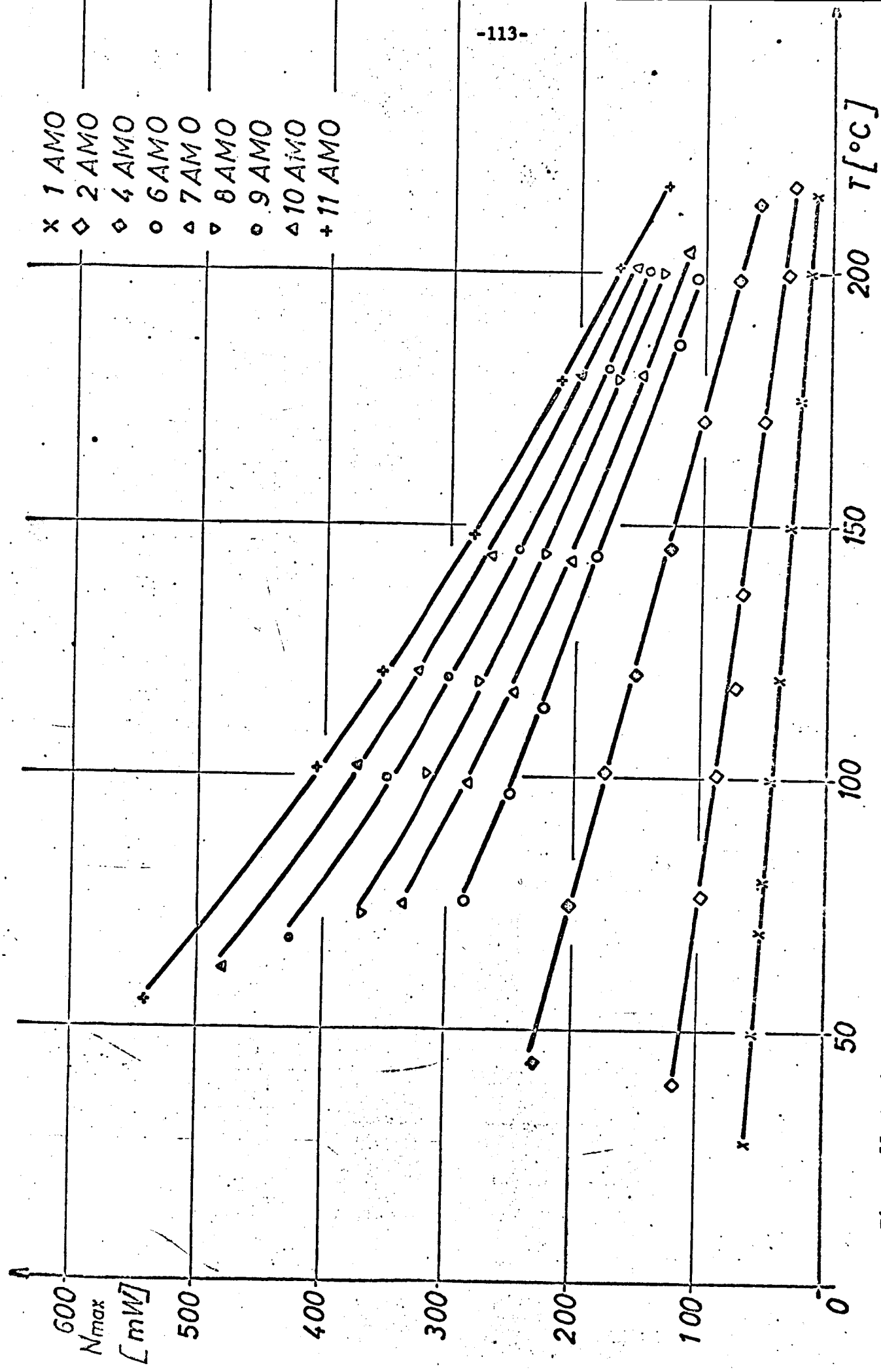


Figure 55 Maximum output of a type V solar cell at temperatures from +40°C to +217°C under high insolation up to 11 AMO.

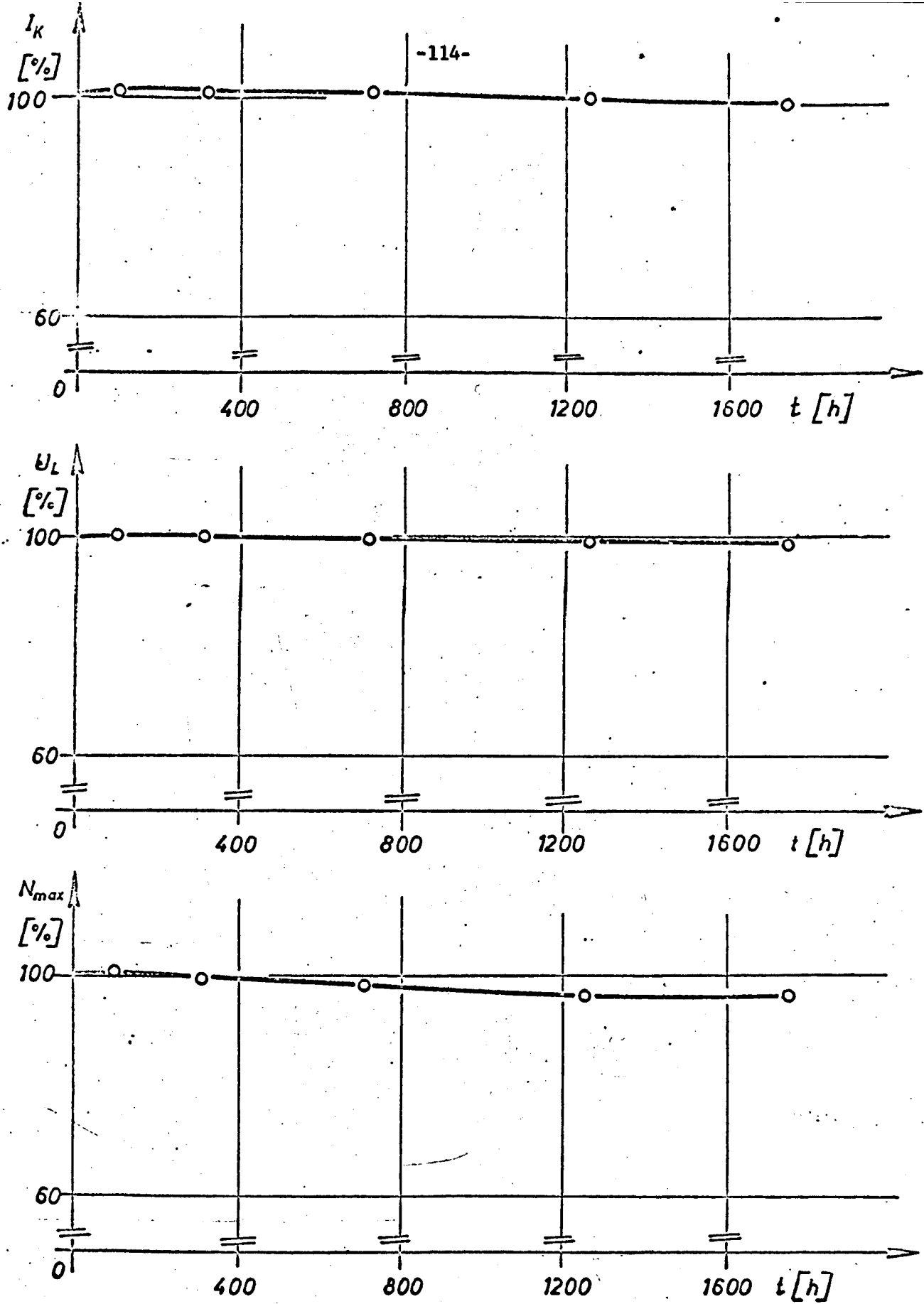


Figure 56 High temperature storage in a high vacuum at $+200^{\circ}\text{C}$.
 Percentage change of short circuit current, idling potential,
 and maximum output of type V solar cells.

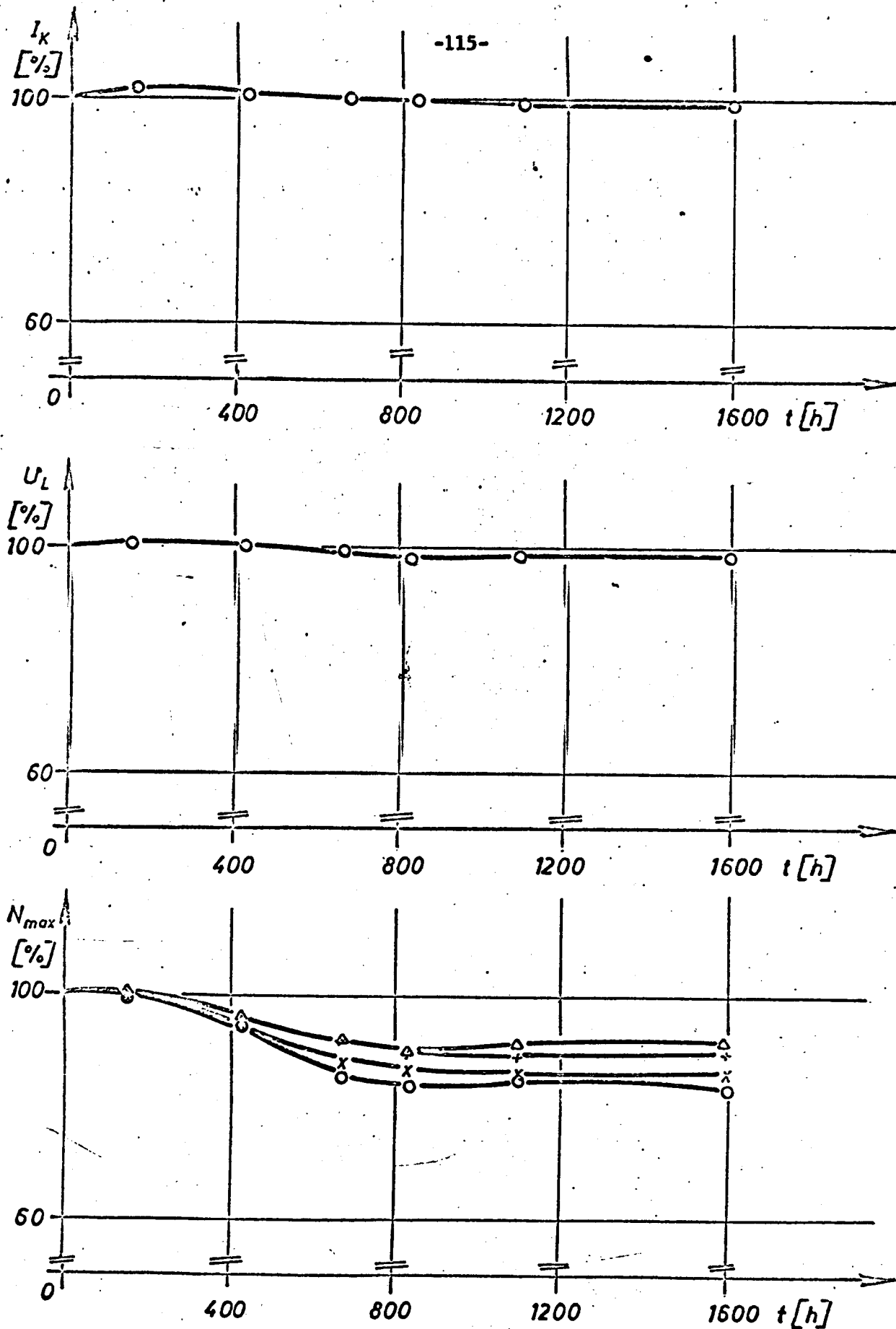


Figure 57 High temperature storage in protective gas atmosphere at +300°C. Percentage change of short circuit current, idling potential and maximum output of type V solar cells.

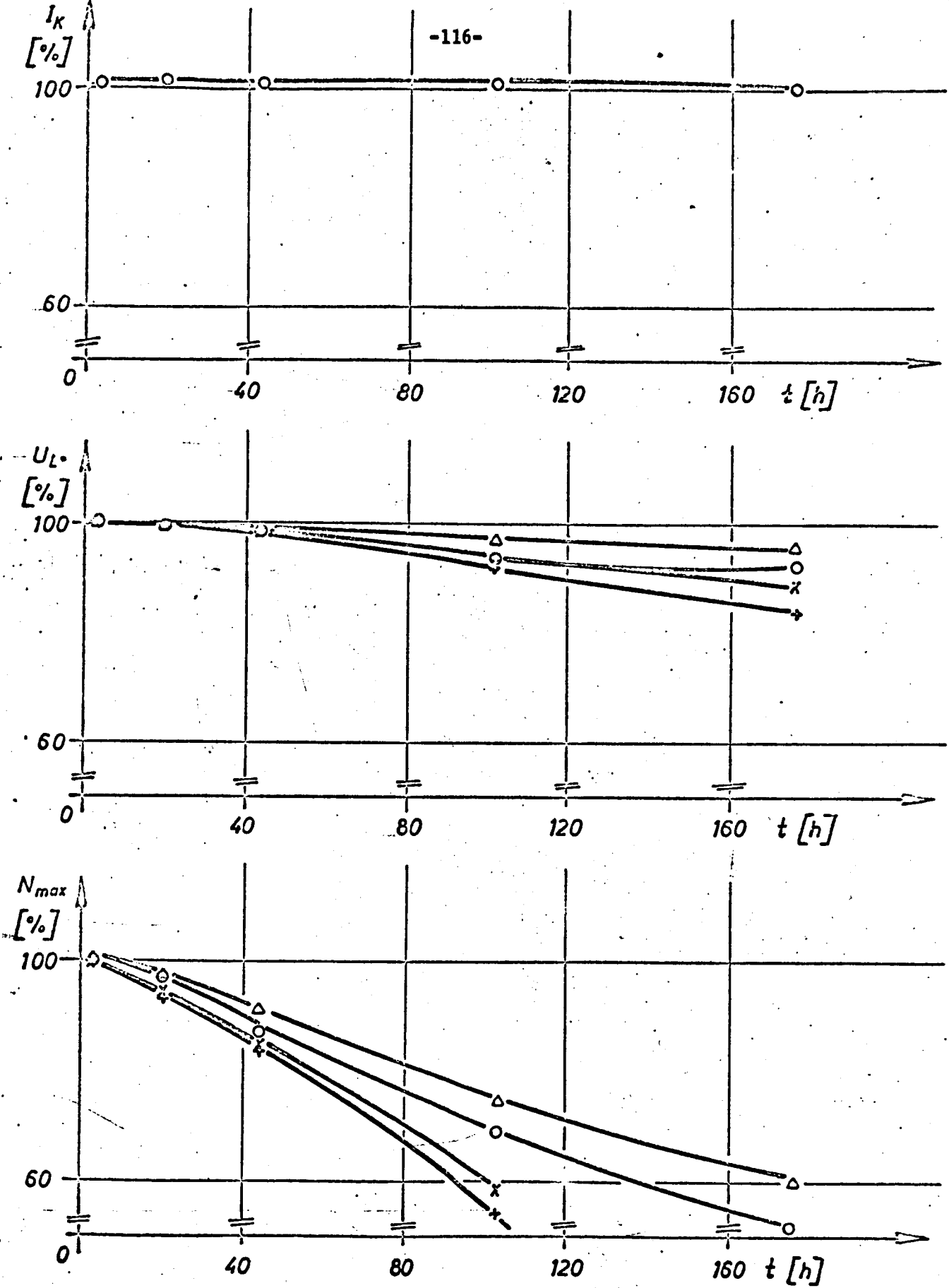


Figure 58 High temperature storage in protective gas atmosphere at $+400^{\circ}\text{C}$. Percentage change of short circuit current, idling potential and maximum output of type V solar cells.

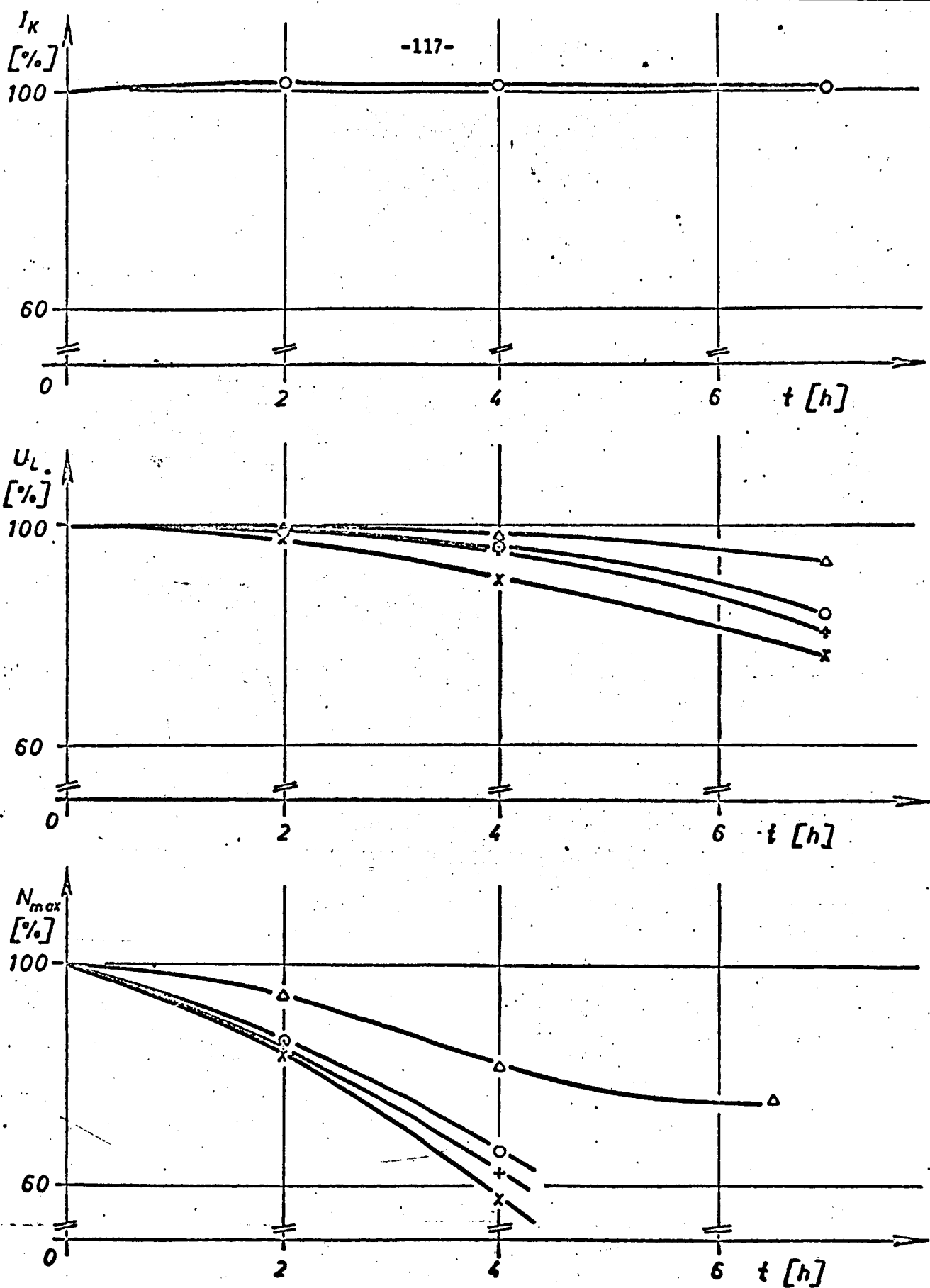


Figure 59 High temperature storage in protective gas atmosphere at +515°C. Percentage change of short circuit current, idling potential and maximum output of type V solar cells.

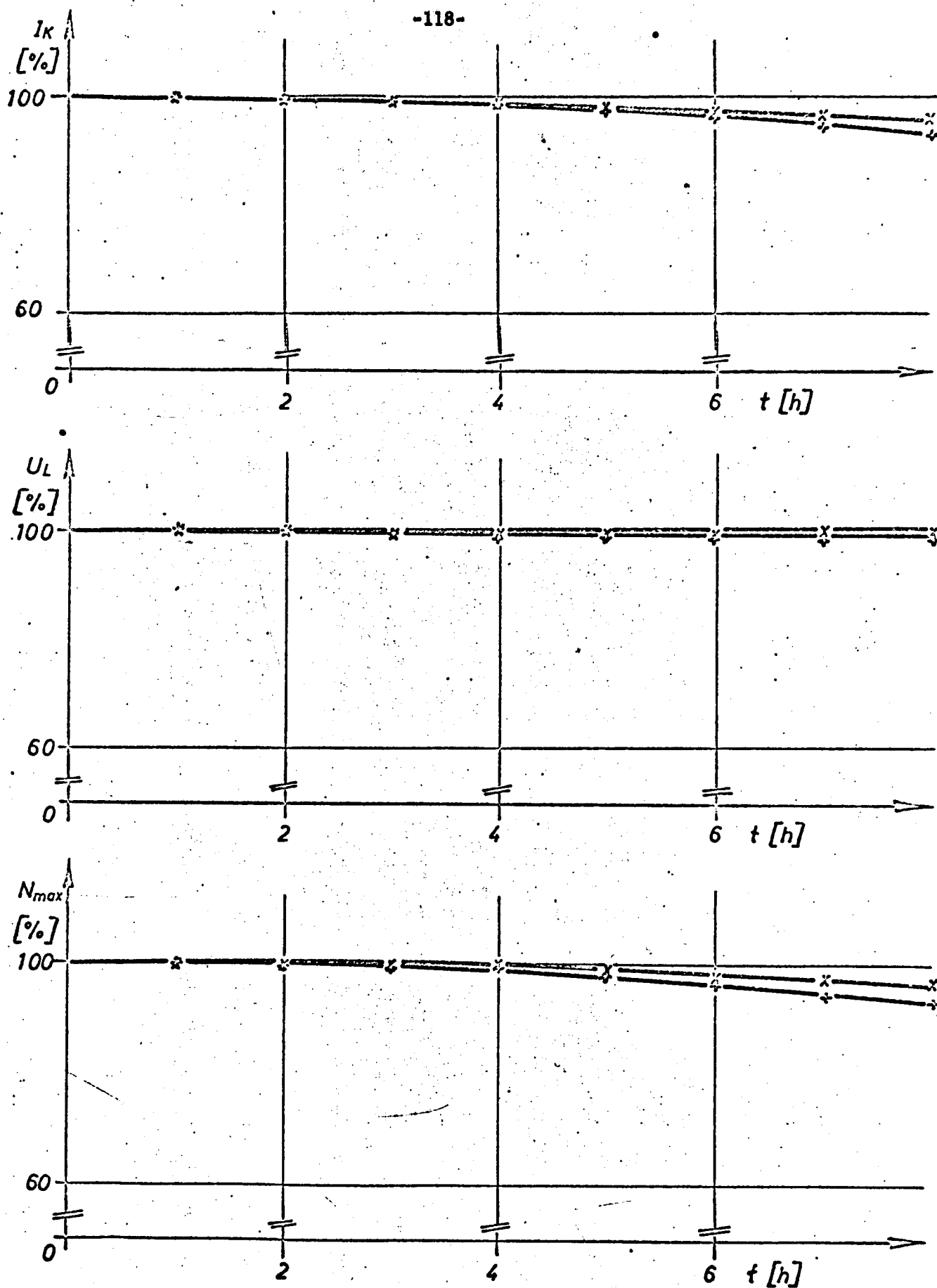


Figure 60 Boiling water test; percentage change of short circuit current, idling potential and maximum output of type IV and V solar cells when stored in boiling water.

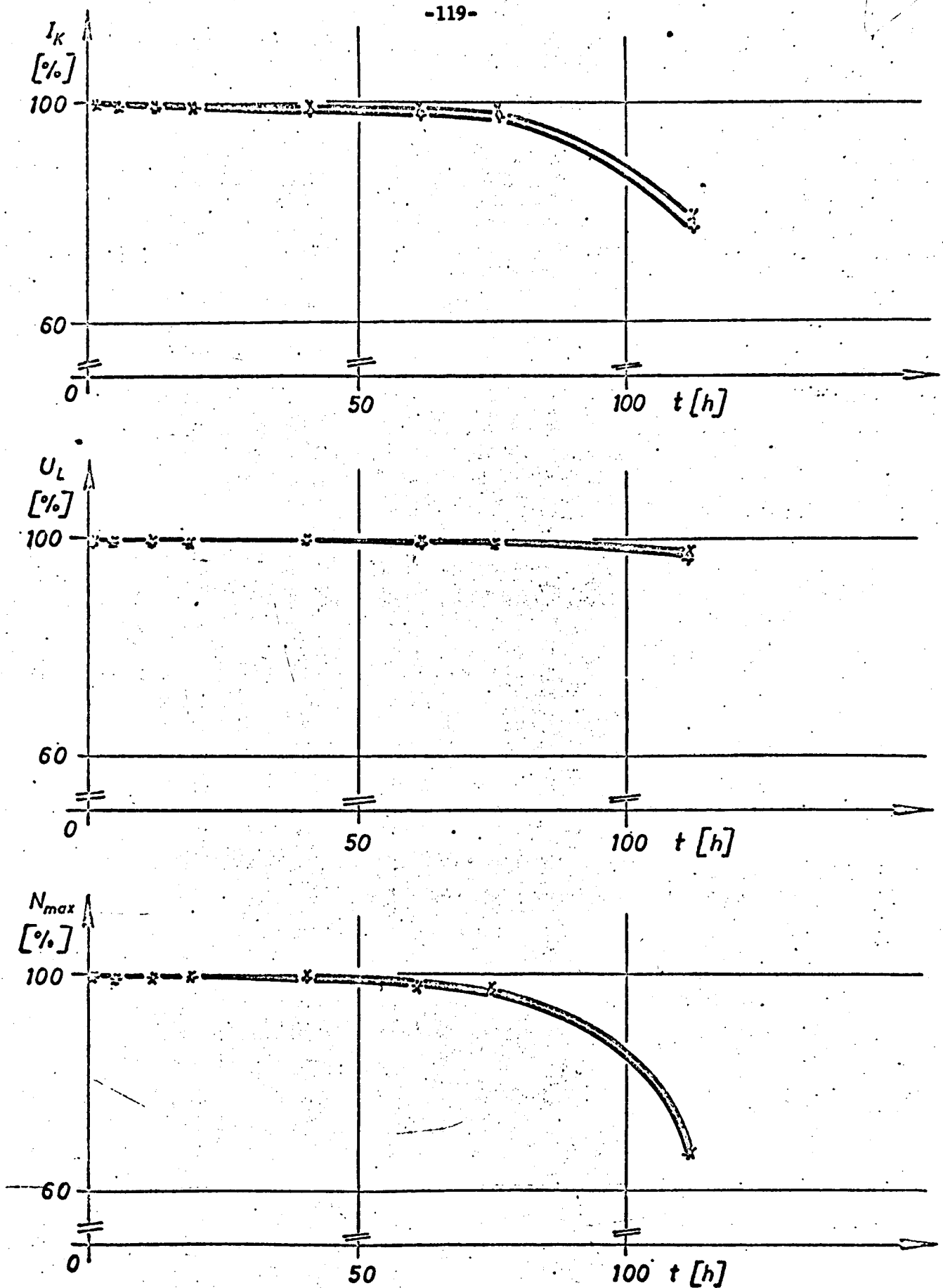
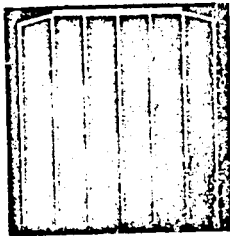
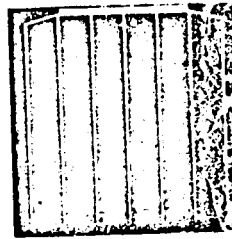


Figure 61. Water vapor test: percentage change of short circuit current, idling potential and maximum output of type IV and V solar cells when stored over boiling water.



294 T 31



300 T 42

Figure 62 Solar cells after water vapor test. On the left cell the optical tempering layer shows changes over a smaller area than it does on the right cell. Short circuit current and maximum output are influenced accordingly.

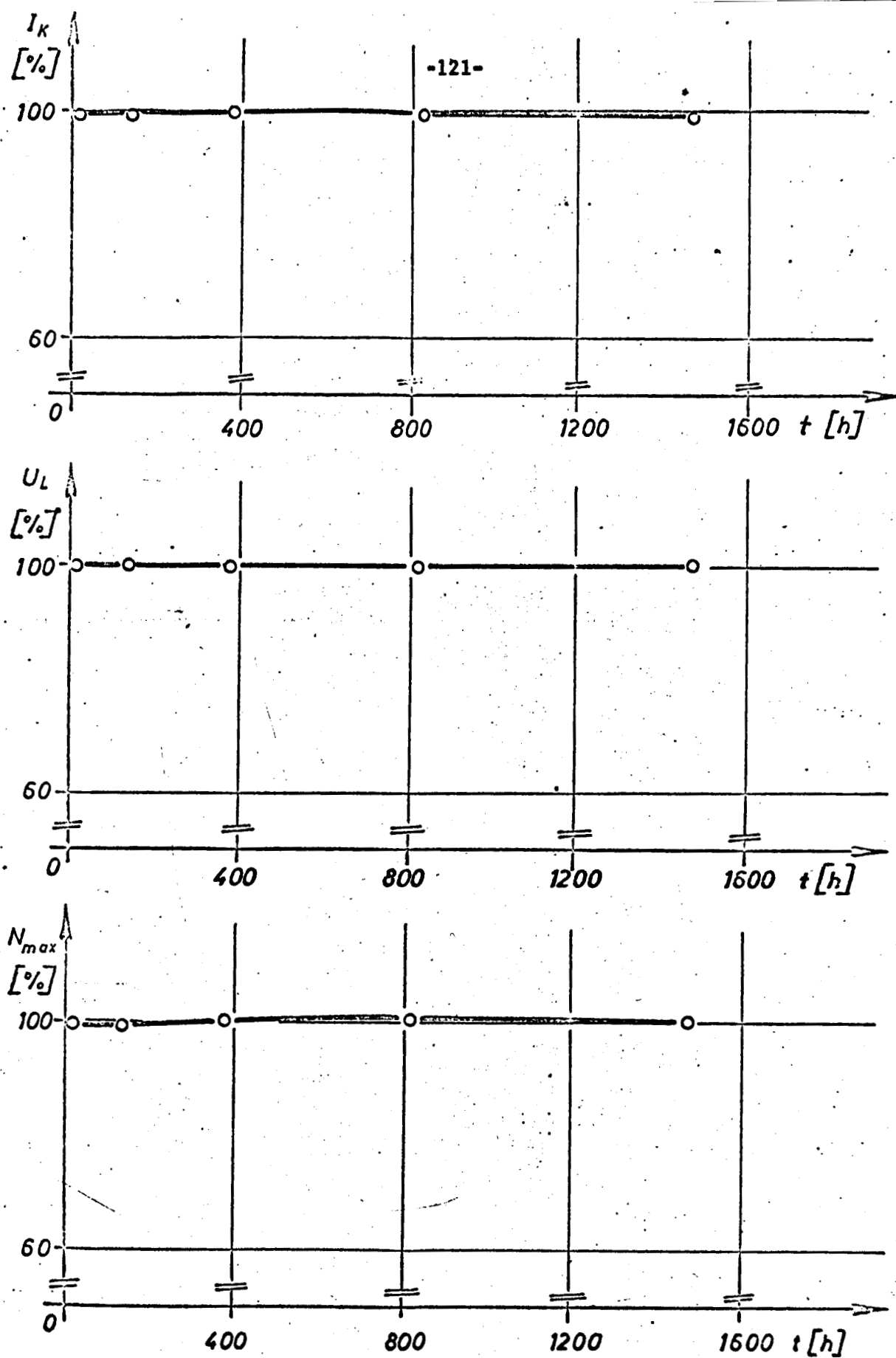
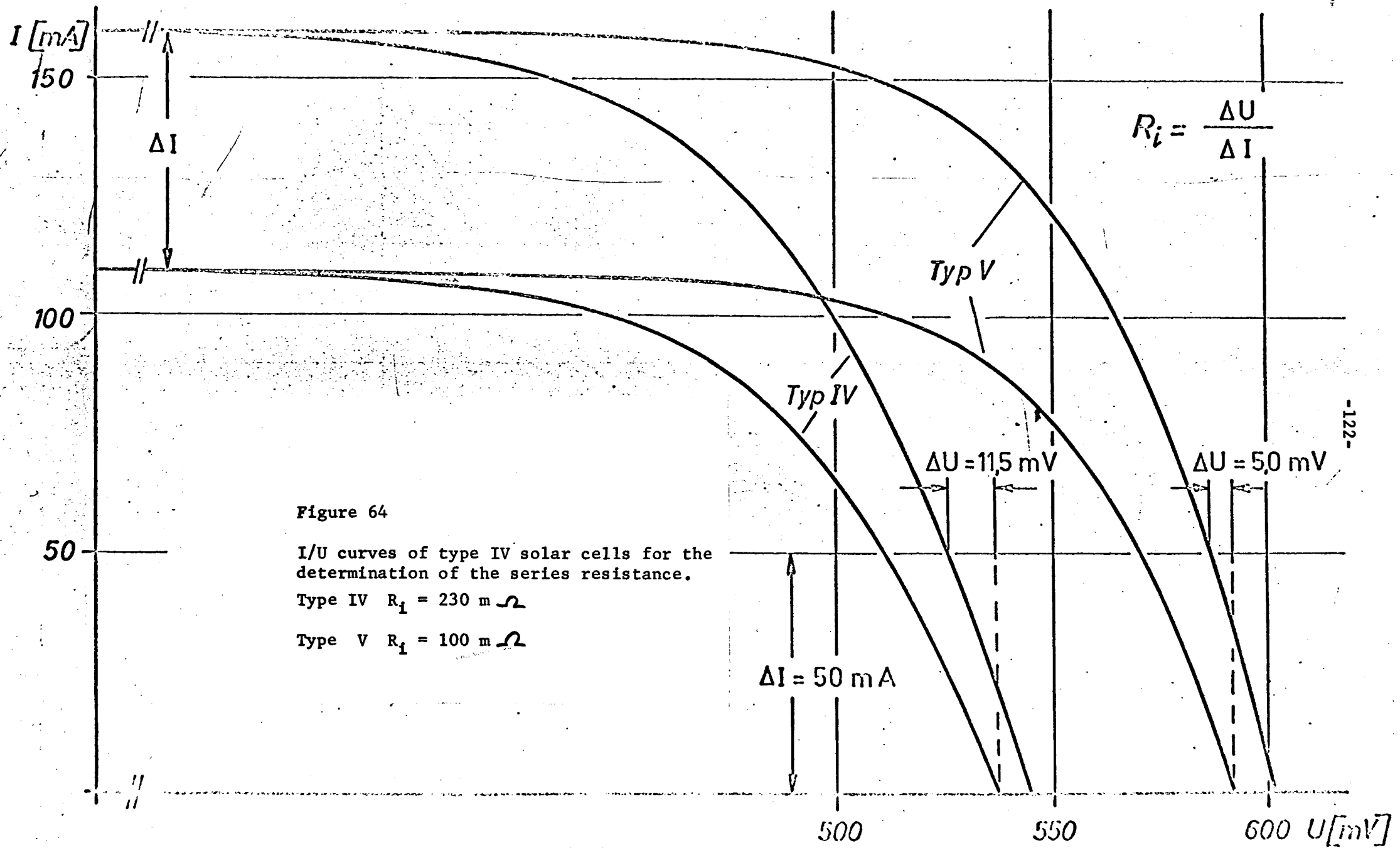


Figure 63 Humidity test: percentage change of short circuit current, idling potential and maximum output of solar cells (at) $+80^{\circ}\text{C}$.



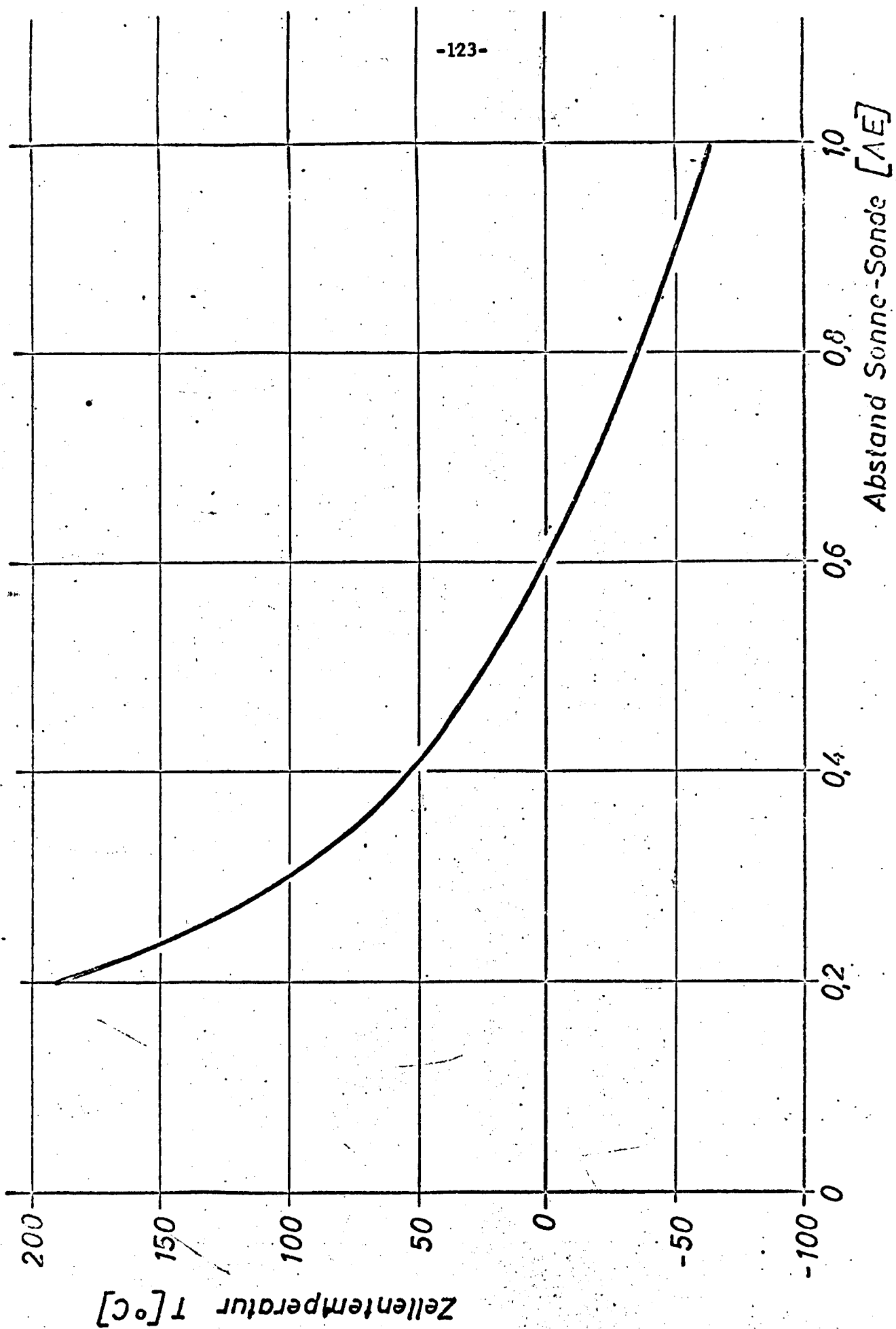


Figure 65 Solar cell temperature as a function of the distance sun - probe. Double cylinder shape, degree of coverage 40%, values according to Dornier.

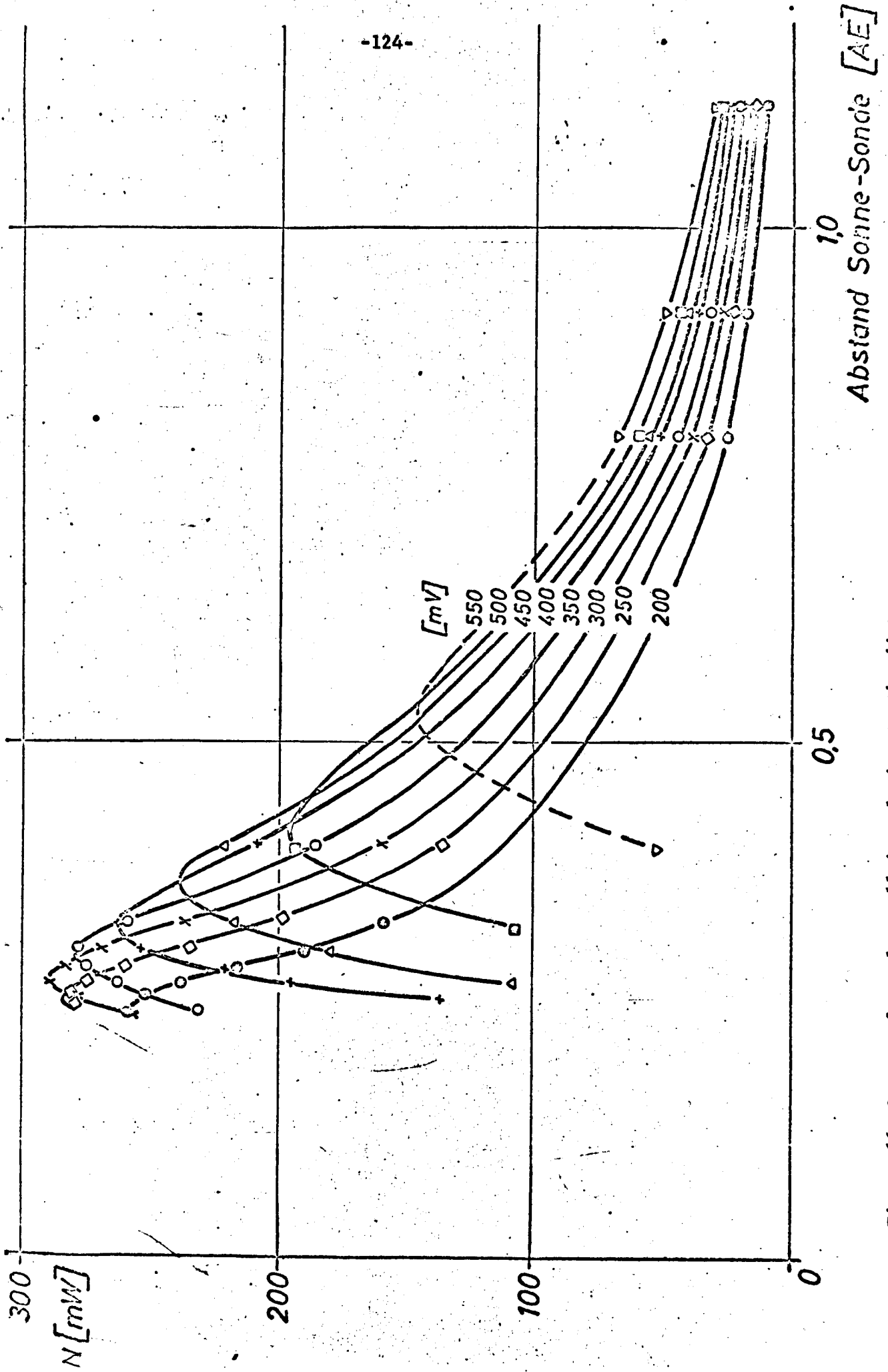


Figure 66 Output of a solar cell in relation to the distance sun - probe for steady cell potentials.

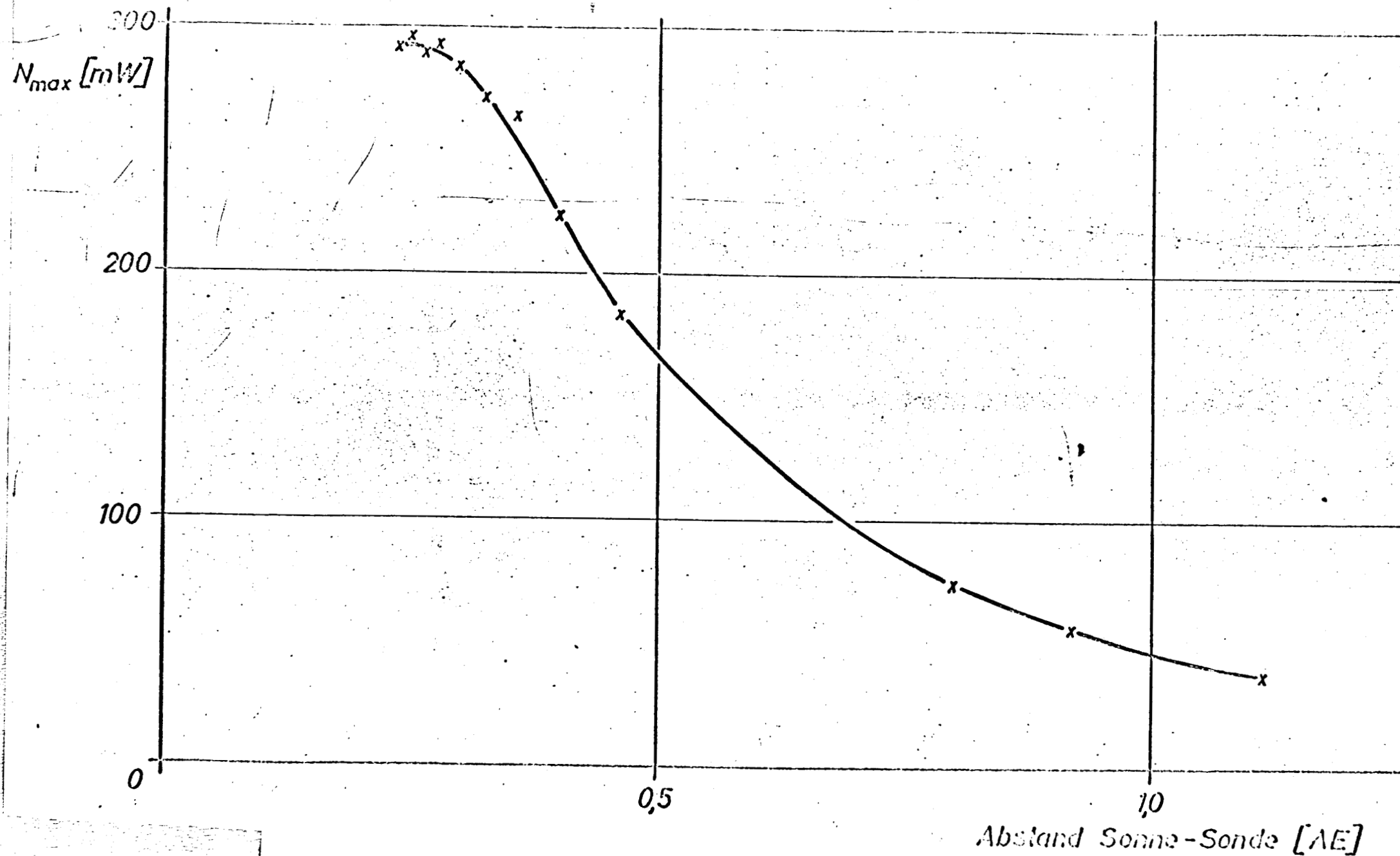


Figure 67 Maximum output of a solar cell in relation to the distance
sun • probe.